UNIVERSITY OF CALIFORNIA,

IRVINE

From Proteins to Protons: Fabrication of Nanoscopic Conductive Polymers Biosensors for Point-of-care Diagnostics

DISSERTATION

submitted in partial satisfaction of the requirements

for the degree of

DOCTOR OF PHILOSOPHY

in Chemistry

by

Nicholas P. Drago

Dissertation Committee:
Professor Reginald M. Penner, Chair
Assistant Professor Joe Patterson
Professor Shane Ardo

2022

DEDICATION

To my wife Nora: Without your love and constant support, I could not have accomplished all that I have during the last 4 years. You have been an incredible partner and sacrificed so much of your time and energy to support me and my studies.

To my parents Paul and Darlene: You have always provided a safe and nurturing environment for me to grow and achieve whatever I set my mind to. I will always appreciate your support of my education and career opportunities even though they may take me far away from home.

To my sister Stephi: You have taught me that doing the right thing and doing the difficult thing are often one and the same. The fervor in which you support what you believe in has taught me a lot about the world and had a lasting impact on me and what I stand for.

To Lori, Dave, Alex, and Julie: You have provided me a home away from home and I am incredibly grateful for all of you being such a great support system throughout these years.

To my Aunt Pat and Uncle Jay: Your support of my education has helped me immeasurably throughout undergraduate and graduate school. I will always appreciate your constant interest and encouragement in my personal and professional life.

TABLE OF CONTENTS

LIST OF FIGURES

LIST OF TABLES

ACKNOWLEDGEMENTS

I humbly acknowledge my advisor Professor Reginald Penner for his continued mentorship throughout my PhD. Reg allowed me agency to make my own scientific decisions, while also teaching me so much about analytical experimentation, scientific communication, and publishing academic work. I would like to thank Professor Shane Ardo and Professor Joe Patterson for their valuable advice regarding my PhD work. This work was made possible through valuable collaborations with Professor Gregory Weiss and his students, Jason Garrido, Emily Sanders, Alicia Santos, Sudipta Majumdar, and Sanjana Sen. I would also like to acknowledge my coauthors Dr. Jihoon Shin, Dr. Aisha M. Attar, Prof. Alana Ogata, Debora Yoon, Andrew Wheat, Shae Patterson, Prof. Il Do Kim, and Justin Van Houton. Furthermore, this work would have been impossible without the time and energy of the team at PhageTech Inc., Jeffrey Briggs and Marie True.

I would also like to thank my fellow graduate students and coauthors in the Penner Lab throughout my time in graduate school, Dr. Guarav Jha, Dr. Apurva Bhasin, Dr. Josh Ziegler, Vivian Chen, Eric Choi, Dr. Ilektra Andoni, Nick Humphrey, and Heriberto Zuleta. These scientists were always supportive, willing to help solve any problems that came up in the lab, and created a friendly and fun environment to work in. Special shout out to Apurva and Eric for their valuable help and collaboration with all the VBR work.

Additionally, I acknowledge the incredible undergraduate professors who are responsible for my initial interest in Chemistry, Professor Colleen Munro-Leighton, Professor Michelle Applebee, Professor Kimberly Lawler-Sagarin, Professor Ami Johanson, Professor Eugene Losey, and Professor Joel Southern. The incredible culture of learning and mentorship at Elmhurst University was paramount in my development as a young scientist. These professors cultivated a welcoming environment that nurtured my curiosity about the fundamentals of Chemistry. This allowed me to not only learn how to answer their questions, but also how to ask my own questions without fear of judgement. I regard the ability to recognize what I don't know and ask insightful questions about it as the most important skill I have ever learned. I am grateful for the Elmhurst University Chemistry Department for providing an environment where I could develop that skill.

I thank Elsevier for permission to include a portion of chapter one of this dissertation, which is to be published in *Materials Today*. I also thank The American Chemical Society for permission to include a portion of chapter one of this dissertation, which was published in *Accounts of Chemical Research* and chapters two, three, and four of this dissertation, which were published in *Analytical Chemistry*. This work was financially supported by the National Science Foundation, through contract CBET-1803314, CBET-2149631 and CHE 2201042, the national Cancer Institute of the NIH, through contract 1R33CA206955-01, PhageTech Inc., through contract PHAGE-203015 and the Chao Family Comprehensive Cancer Center, UC Irvine. Microscopy data were acquired using the instrumentation of the LEXI (lexi.eng.uci.edu/) and IMRI (ps.uci.edu/imri/) facilities at UCI. We thank the healthy urine donors who consented to have their urine used in this study through UCI clinical protocol IRB HS# 2014-1758.

VITA

Nicholas P. Drago

October 12, 2022

EDUCATION

Doctor of Philosophy, Chemistry
2022
University of California, Irvine — Irvine, CA

Bachelor of Science, Chemistry — 2018
Elmhurst University — Elmhurst, IL

RESEARCH

Graduate Research Assistant — 2018-2022
University of California, Irvine — Irvine, CA

Researcher Intern — 2018
Argonne National Laboratory — Lemont, IL

Undergraduate Researcher — 2015-2018
Elmhurst University — Elmhurst, IL

Undergraduate Researcher — 2017
University of California, Davis — Davis, CA

PUBLICATIONS

1. "Electrodeposition-Enabled Chemical Sensors and Biosensors: 2017 – Present." Eric J. Choi, Nicholas P. Drago, Nicholas Humphrey, Justin Van Houton, Il Do Kim, Alana F. Ogata, Reginald M. Penner, Accepted September 2022
2. "A Nanojunction pH Sensor within a Nanowire." Nicholas P. Drago, Eric J. Choi, Jihoon Shin, Il Do Kim, Regniald M. Penner, Anal. Chem., 2022, 94, 35, 12167–12175
3. "Enhancing the Sensitivity of the Virus BioResistor by Over-Oxidization: Detecting IgG Antibodies." Apurva Bhasin†, Eric J. Choi†, Nicholas P. Drago†, Jason Garrido, Emily C. Sanders, Jihoon Shin, Ilektra Andoni, Dong-Hwan Kim, Lu Fang, Gregory A. Weiss*, Reginald M. Penner*, *Analytical Chemistry*, 2021, 93, 32, 11259–11267
4. "Viruses Masquerading as Antibodies in Biosensors: The Development of the Virus BioResistor." Apurva Bhasin, Nicholas P. Drago, Sudipta Majumdar, Emily C. Sanders,

Gregory A. Weiss, Reginald M. Penner, *Accounts of Chemical Research*, 2020, 53, 2384 - 2394

5. “A Virus BioResistor (VBR) for Bladder Cancer Detection: Dip-and-Read Detection of DJ-1 in Urine at 10 pM in One Minute.” Apurva Bhasin, Emily C. Sanders, Joshua M. Ziegler, Jeffrey S. Briggs, Nicholas P. Drago, Aisha M. Attar, Alicia M. Santos, Marie Y. True, Alana F. Ogata, Debora V. Yoon, Sudipta Majumdar, Andrew Wheat, Shae V. Patterson, Gregory A. Weiss, Reginald M. Penner, *Analytical Chemistry*, 2020, 92, 6654 – 6666

ABSTRACT OF THE DISSERTATION

From Proteins to Protons: Fabrication of Nanoscopic Conductive Polymers Biosensors for Point-of-care Diagnostics

by

Nicholas P. Drago

Doctor of Philosophy in Chemistry

University of California, Irvine, 2022

Professor Reginald M. Penner, Chair

Conductive polymers are often used in biosensing architectures of many kinds. Their biocompatibility, electrical conductivity, and ease of polymerization allows many routes to fabricate innovative, nanoscale biosensors for point-of-care diagnostic purposes. The focus of this dissertation will be on two different types of nanoscale, conductive polymer biosensors that were fabricated since 2018 in the Penner Lab by myself and my associates. The first device is the Virus BioResistor (VBR). This device employs poly(3,4-ethylenedioxythiophene) (PEDOT) which is electropolymerized in the presence of virus particles which have been genetically engineered to bind a specific protein. A baselayer of PEDOT:PSS is used as a target for this electrodeposition. This event produces an electrically conductive bioaffinity layer, through which impedance measurements can be taken. In Chapter 2, advances are made to this device by increasing the PEDOT:PSS baselayer are discussed. The increase in the baselayer resistance causes a ~4x signal enhancement, without sacrificing signal-to-noise or specificity. The resulting device can detect deglycase 1 (DJ-1), a bladder cancer biomarker, at 10 pM in ~30 s. Chapter 3 discusses further enhancements made to the

VBR through over-oxidation. The process of over-oxidation allows for the detection of larger proteins and antibodies, up to 150 kDa. Without this process, the VBR is insensitive to proteins larger than 66.5 kDa. This process has been shown to enable detection of multiple antibodies. Following this work, an effort was made to engineer a conductive polymer sensor that is nanoscopic in 3 dimensions, compared to the VBR which is only nanoscopic in 1 dimension. This device is discussed in Chapter 4 and is called a Nanojunction pH sensor (*NJ-pH*). The *NJ-pH* sensor relies on lithographically patterned nanowire electrodeposition to fabricated single gold nanowires onto which electrical contacts are evaporated. A nanogap is formed in this nanowire through electromigration, and the gap is then bridged through electropolymerization of poly(aniline) (PANI) which has a resistance that is pH sensitive. This device is shown to have impedances that range 5 orders of magnitude between pH 1 – 9, and can give a reliable pH measurement within 30 s. This device is completely nanoscopic and offers a new avenue for monitoring local pH on the nanoscale.

Chapter 1: Introduction

Major portions of this section have been adapted from the following publications submitted to Materials Today and Accounts of Chemical Research: ”Electrodeposition-Enabled, Electrically-Transduced Sensors and Biosensors: 2017 – Present.” and “Viruses Masquerading as Antibodies in Biosensors: The Development of the Virus BioResistor.”

1.1. Introduction to Electrically Transduced Sensors Enabled by Electrodeposition and Electropolymerization

Electrodeposition (ED) is now more than two centuries old but its application to the fabrication and function of sensors and biosensors is relatively recent. Only since 1980 has ED, and its relative, electropolymerization (EP), been exploited to enhance the properties of sensors and biosensors. In these applications, the three attributes of ED are: i) Precision, ii) Selectivity, and iii) Compatibility. ED allows precise control of the quantity of electrodeposited material, of composition, of particle size, of surface roughness, and in some cases, control of the porosity of the electrodeposit. ED and EP also afford the ability to prepare composites containing two or more materials such as an antibody, a chelator, a single-stranded DNA (ss-DNA), or other receptors.

The *precision* intrinsic to ED is, itself, an attribute: The fine control afforded in ED using current and potential is difficult to match using alternative deposition methods, such as physical vapor deposition, sputtering, spin-coating, spraying, imprinting, and so on. A second attribute is that ED imparts spatial *selectivity* to the ED process because the deposition process can be targeted at, and confined to, a single conductor amongst other sensor components. For example, a polymer film can be EDed onto a metal transducer without risking contamination of other sensor parts with this material. Moreover, ED and EP can be carried out on conductors that are immersed in aqueous plating solutions. This means that biological materials such as proteins, antibodies, and aptamers can be co-deposited using ED and EP. This *compatibility* of ED and EP with aqueous solutions, has been a major driver of the application of ED and EP to the fabrication and function of biosensors.

1.2. A Brief History of Electrodeposition and Electropolymerization

1.2.1. Historical Milestones

A pictorial timeline (Figure 1.1) lists some milestones marking progress related to the application of ED to sensor and biosensor development prior to 2017.

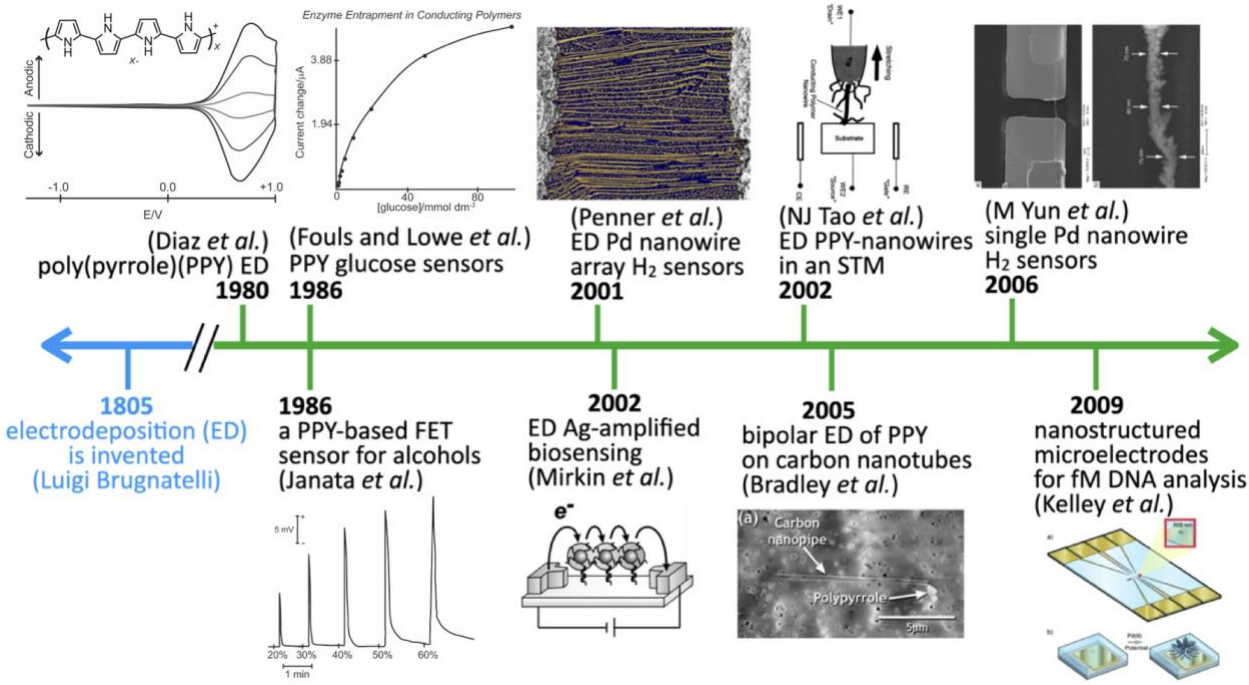

Figure 1.1 - Milestones in ED and EP-enabled electrically-transduced chemical sensing and biosensing. The references highlighted here can be found in Section 1.

1.2.2. Electronically conductive polymers.

This chronology begins with chemiresistive sensors in which electronically conductive organic polymers functioned as either receptors or transducers or both. In 1980, Art Diaz and coworkers at IBM discovered that heterocycles including pyrrole, thiophene, and aniline could be electropolymerized to form conductive films simply by oxidizing solutions containing these monomers [1–5]. This process, known as electropolymerization (EP), helped the initial development of ED-enabled sensors. Diaz and coworkers demonstrated that electrodeposited films of poly(pyrrole) (PPY), poly(thiophene), and poly(aniline) (PANI) showed electrochromic behaviors and strongly modulated electronic conductivity that were both correlated with the redox electrochemistry of these films.

By 1986, these electropolymerized polymers, such as (poly(3-methyl-thiophene) [6], and their derivatives, including poly(3,4 ethylene dioxythiophene) (PEDOT) [7], were exploited for the fabrication of sensors and biosensors targeting a range of molecules. Art Janata, a pioneer in the development of a field-effect transistor (FET) based chemical sensors [8–10], reported a solid-state alcohol vapor sensor based upon a suspended-gate FET (SGFET) in which a platinum (Pt) gate modified by electrodeposited PPY, as well as several derivatives, sensitized the SGFET to a series of primary alcohols with response times within seconds [11]. Likewise, PPY was being widely applied to gas sensors [12] and biosensors[13] in the same time period.

Foulds and Lowe [14] were among the first to incorporate enzymes into PPY by co-electrodeposition/electropolymerization. This strategy was applied in 1986 to prepare an amperometric glucose sensor based upon the incorporation of glucose oxidase into PPY [14].

1.2.3. Metal and Polymer Nanowires

The next class of transducers/receptors to emerge were one-dimensional nanowires based on metals and polymers, by virtue of their high specific surface area that promotes a more sensitive detection of analytes compared to the film-type sensors. This was kickstarted in 2001 by the development of a nanowire ED method termed electrochemical step edge decoration (ESED) [15,16], which involved the nucleation and growth of the electrodeposited metal on the step edges of highly oriented graphite electrodes. These nanowire networks were then transferred from the graphite surface onto a glass slide by embedding them in a polymer film. Silver (Ag) epoxy was then used to establish electrical contacts to these nanowire networks. Palladium (Pd) nanowire networks prepared by ESED comprised the first palladium nanowire hydrogen gas sensors [17,18].

In parallel with this discovery, the first-ever successful synthesis of polymer nanowires prepared by a modified EP process was described by Nongjian Tao and colleagues in 2002 [19]. Their approach involved the application of a tip in a scanning tunneling microscope. The surface of the conductive substrate and the tip were both poised at a potential exceeding that of the onset for PANI polymerization from aniline. As this polymerization proceeded at both the tip and surface, the gap between these elements was bridged, forming a nanowire [19].

In 2004, Yun, Myung, and others demonstrated the preparation of single PPY and Pd nanowires by EP and ED, respectively [20,21]. In 2006, single Pd nanowire chemiresistors prepared using this method were used for the detection of H_2 gas for the first time [22]. Bradley and coworkers [23] demonstrated that carbon nanotubes could be decorated with PPY without making a direct electrical connection to the nanotube using a bipolar electrodeposition method. PPY decoration of carbon nanotubes provided a means for controlling how much water is within these structures [23].

1.2.4. Signal Transduction and Amplification

An innovation in 2002 was the discovery by Mirkin *et al.* [24] that immunogold staining methods that have been developed for microscopy [25], in which Ag is grown on gold (Au) labels by electroless deposition to increase contrast, could be used to provide amplification of sandwich assays involving a Au nanoparticle label. In these experiments, a ss-DNA capture strand was recognized by a complimentary ss-DNA probe strand conjugated to a Au nanoparticle, at concentrations as low as 0.5 pM. In this experiment, ss-DNA capture strands are located between two lithographically patterned Au electrodes that measure a percolating current across this affinity layer as Ag deposition onto the immobilized Au nanoparticles increased the measured current between these electrodes [24].

Subsequently, in 2009, Su *et al.* [26] exploited the same scheme for the detection, using a quartz crystal microbalance (QCM) as the transducer. In this work, the detection sensitivity of human IgG (h-IgG) was enhanced by 100 times in a sandwich assay involving an Au nanoparticle-labeled anti-h-IgG after applying solution-phase electroless Ag plating process for 20 min [26].

1.2.5. Lithographically Patterned Nanowire Electrodeposition

A significant technological advance was made in 2006 through the development of the lithographically patterned nanowire electrodeposition (LPNE) process, which can be used to prepare high-quality metal nanowire arrays [27,28]. In contrast to the ESED process that was reported in 2001 [15,16], LPNE allowed the position of a nanowire to be precisely determined using a photolithographic process. Importantly, the nanowire dimensions were controlled by processing steps that were not affected by the diffraction of light, enabling the fabrication of sub-wavelength, nanometer-scale wires [27,28].

Compared with the process of Yun and Myung (2006) that only allowed the synthesis of single strands of polymer and metal nanowires one at a time [29,30], LPNE provided for the deposition of any number of nanowires in parallel, in virtually any pattern achievable by photolithography [27,28]. LPNE was first used to prepare H_2 sensors based on single Pd nanowires in 2009 with improved performance compared to previously reported Pd-based sensors [31].

1.2.6. Nanostructured metal microelectrodes.

The development in 2009 [32–34] of ED-prepared nanostructured microelectrode transducers by Shana Kelley became the springboard for a completely new strategy for biosensing [35,36]. In these experiments, highly dispersed metal transducers with micron-scale dimensions were functionalized with ss-DNA and other receptors, and their electrochemical responses to target redox species in solution were monitored. By this, the binding of target species with the immobilized receptors could effectively be transduced into electrical signals. Uniquely, the sensitivity of the nanostructured transducer could be tuned based on its level of dispersion, which was controlled by the electrodeposition parameters used for its preparation [37].

1.3. Introduction to the Virus BioResistor

1.3.1. Viruses and Biosensors

The 2018 Nobel Prize in Chemistry recognized *in vitro* evolution, including the development by George Smith and Gregory Winter of phage display, a technology for engineering the functional capabilities of antibodies into viruses. Such bacteriophage solve inherent problems with antibodies including their high cost, thermal lability, and their propensity to aggregate. While phage display accelerated the discovery of peptide and protein motifs for recognition and binding to proteins in a variety of applications, the development of biosensors using intact phage particles was largely unexplored in the early 2000's. Virus particles, 16.5 MDa in size and assembled from thousands of proteins, could not simply be substituted for antibodies in any existing biosensor architectures.

Incorporating viruses into biosensors required us to answer several questions: What process will allow the incorporation of viruses into a functional bioaffinity layer? How can the binding of a protein disease marker to a virus particle be electrically transduced to produce a signal? Will the variable salt concentration of a bodily fluid

interfere with electrical transduction? A completely new biosensor architecture, and a new scheme for electrically transducing the binding of molecules to viruses, was required.

The Penner Lab became interested in this problem in 2005.[38] Up to this time, most biosensors designed to detect the distinctive protein "biomarkers" produced by cancers used antibodies to recognize and bind these proteins. M13, a filamentous bacteriophage that infects Ecoli, was engineered to "display" Fv antibody fragments on their surfaces providing an intriguing opportunity for the development of cheaper, more robust biosensors. The basic approach for the "display" of proteins on the M13 phage surface was invented by George Smith in 1985,[39,40] before Jim Wells and co-workers introduced key and necessary improvements to enable Greg Winter to display an antibody, or Fv, on the phage surface.[41,42] Our labs built on such seminal contributions to the history of biotechnology to extend phage display into biosensing applications.

M13 viruses are an attractive alternative to antibodies in biosensors for three main reasons: 1) the cost of engineered viruses is much lower, 2) the affinity of virus particles is similar (often dissociation constants, K_D, are below 10^{-9} M), and, 3) virus particles are quite robust, and, for example, do not require refrigeration to maintain potency. In principle, biosensors based upon virus particles could be cheaper to manufacture and cheaper to distribute and store, especially in the resource-challenged third world. Herein, we trace the development over fourteen years of a new biosensor, the *Virus BioResistor* or *VBR*[43,44], designed specifically for rapid (60 s), point-of-need detection of cancer markers in urine using virus receptors.

1.3.2. Electrodeposition of Virus-PEDOT Bioaffinity Layers

Inspiration for a new type of virus-based bioaffinity layer arrived from an unexpected direction. In the 2010 time frame, the Penner group had been investigating the thermoelectric properties of nanowires composed of the electronically conductive organic polymer PEDOT (poly(3,4-ethylene dioxythiophene).[45] These PEDOT nanowires were prepared by electrodeposition, using the Lithographically Patterned Nanowire Electrodeposition (LPNE) method.[46,47]

Could PEDOT act as a host for M13 virus particles? This idea was interesting for two reasons: First, the electronic conductivity of PEDOT provided a means by which biosensor signal from M13 particles could be directly transmitted to an external circuit.

Second, PEDOT is positively charged as synthesized, with one positive charge for each 4 or 5 EDOT residues. During electropolymerization (Figure 1.2a), 3,4-ethylene dioxythiophene (EDOT) is oxidized to a cation radical, and radical coupling occurs near the electrode surface until the resulting oligomers lose solubility and, with anions from the solution to balance the positive charge, they precipitate onto the electrode. M13 virus particles have a net negative charge near 6000, as a consequence of three ionizable moieties, Glu2, Asp4 and Asp5, on the 2700 copy P8 majority coat protein near its exposed N-terminus.[48] Our hypothesis was that the polymerization of positively-charged PEDOT in the presence of negatively charged M13 would electrostatically promote the incorporation of M13 particles within the polymer matrix.

To test this hypothesis, virus-PEDOT biocomposite films were prepared by electropolymerizing EDOT in aqueous electrolytes containing just 12 mM $LiClO_4$ and nM concentration of M13 virus particles.[49] In these experiments, it was observed that the virus concentration was increased from 3 to 15 nM (the solubility limit), the EDOT electropolymerization current peak was depressed as compared to the virus-free control.[49] This observation suggested that the virus particles were either interfering with, or participating in, EDOT polymerization. QCM gravimetry (Figure 1.2b) showed that the mass of the resulting films was augmented when virus particles were present in the EDOT polymerization solution. The excess mass, relative to pure PEDOT films (Figure 1.2c), was attributed to the incorporation of virus particles into the growing PEDOT film.[49] This observation directly demonstrated that virus particles were being incorporated into these electrodeposited PEDOT films, as predicted by the reaction of Figure 1.2a.

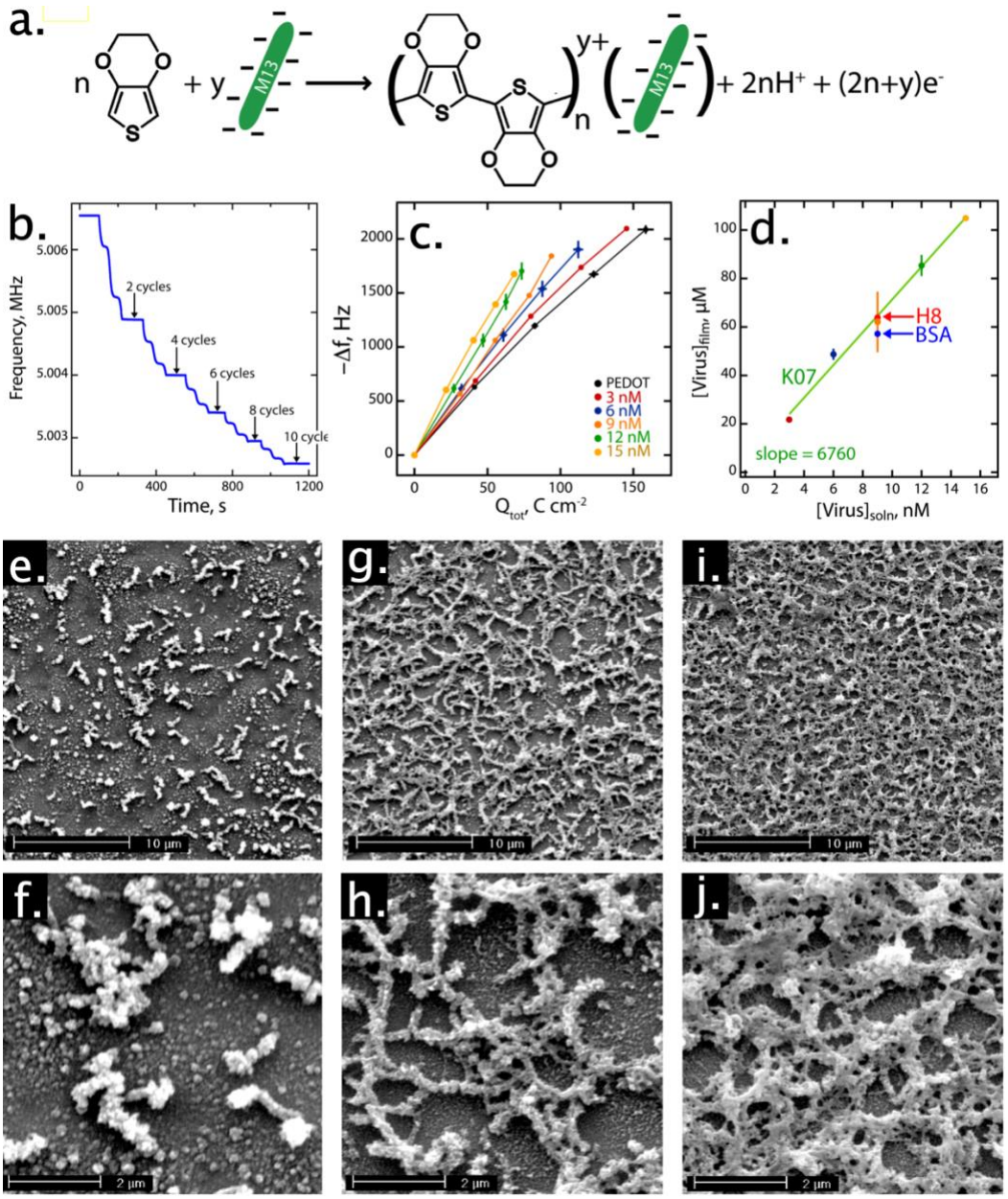

Figure 1.2 - Electrodeposition of a virus-PEDOT bioaffinity layer. a). The virus-PEDOT electrodeposition reaction, b). QCM analysis of virus-PEDOT electrodeposition shows increased mass loading as a decrease in frequency. c) Frequency change *versus* deposition charge, Q_{tot}, for QCM measurements. The positive deviation of *Df* for virus-containing solutions is due to virus incorporation into these films. d) Calibration curve showing the linear correlation of the virus concentration within the PEDOT film (vertical axis) *versus* the concentration of virus in solution. (e-j). Topography of virus-PEDOT films imaged by scanning electron microscopy at two magnifications. All films were prepared using 10 deposition cycles (20 mV/s) from a solution of aqueous 12.5 mM $LiClO_4$, 2.5 mM EDOT, and virus particles at three concentrations: (e,f) $[virus]_{soln}$ = 3 nM, (g,h) $[virus]_{soln}$ = 9 nM, and (I,j) $[virus]_{soln}$ = 15 nM. After Ref.[49]

How efficient is the virus incorporation into these films during electropolymerization? The QCM data of Figure 1.2c provided the answer: The difference in mass (the vertical axis) at a particular deposition charge, Q_{tot}, could be attributed to virus incorporated into the virus-PEDOT composite film. This analysis showed that concentration of the M13 in the virus-PEDOT film prepared by electrodeposition was directly proportional to the M13 concentration in the polymerization solution (Figure 1.2d), and the slope of this line was an astonishing ≈500. These experiments demonstrated that the reaction shown in Figure 1.2a provided for highly efficient incorporation of virus into a growing PEDOT film. SEM images of electrodeposited virus-PEDOT composite films showed a striking transformation as virus was incorporated into the plating solution (Figure 1.2e-j). In these images, bundles of virus particles are seen protruding at the surface of the virus-PEDOT films, and as expected, the density of these virus particles is correlated with the concentration of virus in the deposition solution.[49]

1.3.3. The two-sided virus-PEDOT biosensor

All of the virus-based biosensors investigated in the Penner Lab up to 2015 were laboratory experiments[38,50–56] in the sense that electrochemical measurements conducted using three-electrode cells incorporating separate reference, counter, and working (sensor) electrodes. A portable, miniaturizable, and commercializable electrochemical sensor architecture – in which the necessary electrodes were incorporated into a single monolithic sensor body - had not been demonstrated.

This advance occurred in 2017 with the demonstration by Alana Ogata, Ming Tan, and others that two virus-PEDOT modified gold electrodes, without reference or counter electrodes (Figure 1.3a), could function as a biosensor for human serum albumin (HSA).[57] Prior work on PSMA[55,58] had demonstrated that the signal generated by a virus-PEDOT-modified gold electrode was concentrated in the resistive component of the impedance, Z_{re}, instead of the capacitive component, Z_{im}. The hypothesis explored in the 2017 “two-sided” sensor architecture (Figure 1.3b) was that arranging *two* virus-PEDOT bioaffinity layers electrically in series would double the impedance signal produced by the biosensor.[57]

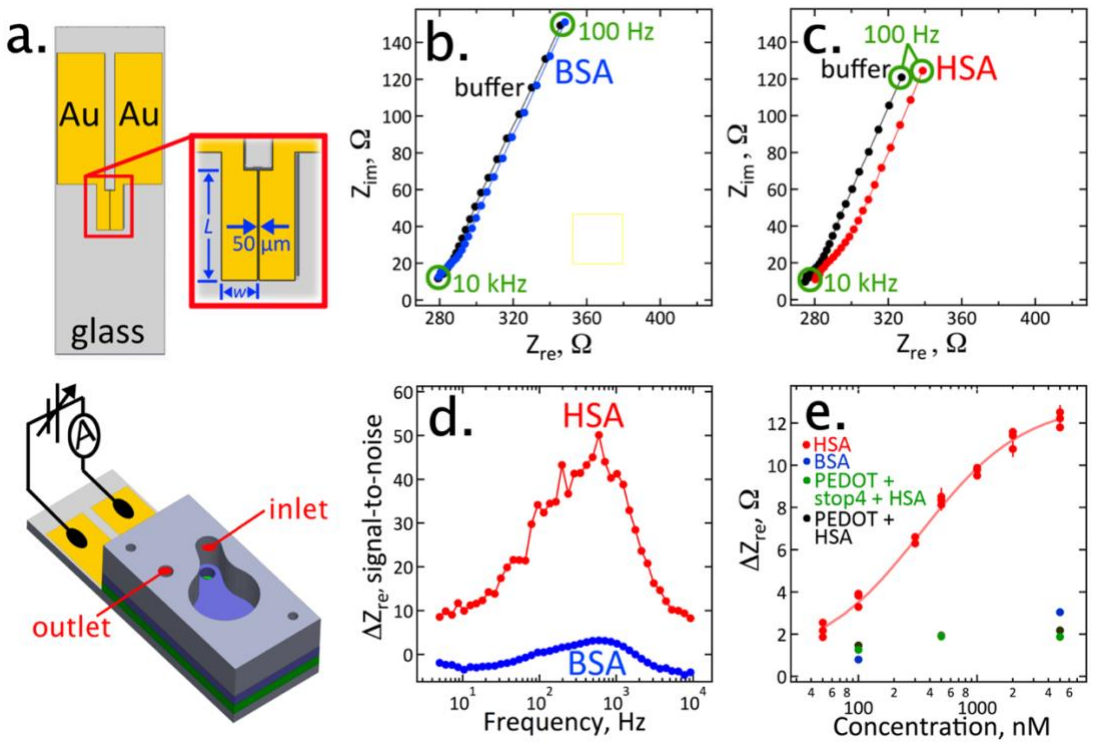

Figure 1.3 - The Two-Sided Biosensor: A Monolithic Biosensor for Human Serum Albumin (HSA). a). Engineering diagram of two electrode virus-PEDOT biosensor. b,c) Nyquist plots (Z_{im} vs. Z_{re}) for a control protein (BSA) and HSA. D). Signal-to-noise *versus* frequency plot for HSA and BSA. E). DR_{re} *versus* HSA concentration calibration curve. Controls for BSA, and off-virus binding also shown. After Ref.[44]

In spite of its simplicity, the two-sided virus-PEDOT biosensor reliably distinguished HSA from BSA – proteins of identical size and having a 76% sequence homology. This demonstrated that the inherent selectivity of the engineered virus could be recovered with this device (Figure 1.3b,c). At an optimized detecting frequency of 340 Hz (Figure 1.3d), the two-sided sensor produced a prompt increase in Z_{re} within 5 s and a stable Z_{re} signal within 15 min. HSA concentrations in the range from 100 nM, its LOD, to 5 µM were detectable using this device (Figure 1.3e). These single-use biosensors demonstrated excellent sensor-to-sensor reproducibility characterized by a coefficient-of-variation of 2−8% across the entire concentration range, a remarkable achievement considering each sensor was hand made in our laboratories.[57] Two-sided virus-PEDOT sensors in synthetic urine demonstrated a concentration dependent response to HSA similar to PBS buffer.

This performance provided reason for optimism, however the two-sided virus-PEDOT biosensor had two serious deficiencies: First, its 100 nM LOD for HSA was insufficient to enable the measurement of cancer markers in urine at sub-nanomolar concentrations. The two-sided sensor simply didn't produce enough signal - a *maximum* of 12 W of signal against a 100-200 W background (Figure 1.3e).[57] Second, the two-sided biosensor required that current was carried through the test solution between the two electrodes, thus convoluting the resistance change due to binding of the target protein with the resistance of the solution. Since urine and other bodily fluids have highly variable ionic conductivities, this imposes a barrier to the use of the biosensor for single patient samples. In order to provide reliable results for highly variable single patient clinical samples, a biosensor architecture that decoupled target binding from ionic conduction was required. On spite of these two issues, the two-sided virus-PEDOT biosensor was the progenitor of the VBR, which will be introduced and discussed in chapters 2 and 3.

1.4. Polymer Nanojunction Sensors

Chapter 4 of this dissertation will be focused on the invention of a single polymer nanojunction pH sensor within a single nanowire. This device is an extension of the VBR (discussed in chapters 2 and 3), as its creation was prompted from the questions:

1. How can the VBR be made to be nanoscopic in all 3 dimensions?
2. What kind of properties would a completely nanoscopic conducting polymer sensor have?

The work done in this section attempts to solve these questions. These experiments function as a proof of concept for future innovation of the VBR, since in the work presented here, viruses were not present in the sensor. These experiments were necessary due to the lack of literature on single nanojunction sensors. A Google Scholar search performed on August 10, 2022, for the keywords "nanojunction sensor" yielded ~150 publications since the year 2000. Furthermore, a search for "single nanojunction sensors" yields only 2 publications since 2000. This lack of research sparked curiosity regarding how the structure of a nanojunction can affect the function of the nanojunction as a sensor. Chapter 4 will discuss the ensuing systematic study on the fabrication of a single nanojunction sensor as well as its structural and electronic properties.

Chapter 2: The Virus BioResistor

This chapter is adapted from a research article “Virus Bioresistor (VBR) for Detection of Bladder Cancer Marker DJ-1 in Urine at 10 pM in One Minute”.

2.1. Introduction

Minimally invasive cancer screening using bodily fluids – so called “liquid biopsies” – may eventually eliminate the evaluation of suspected malignancies using surgery.[59] Liquid biopsies involve the detection in blood, urine, and other bodily fluids of nucleic acids, circulating tumor cells (in blood), or distinctive protein markers that signal the presence of a particular cancer. DJ-1, a 20.7 kDa protein, is elevated in the urine of people with bladder cancer (BC).[60] Presently, the measurement of DJ-1 in urine requires an enzyme-linked immunosorbent assay (ELISA), which is both slow and inconvenient. A biosensor for DJ-1 could accelerate its assessment for the detection of BC recurrence in patients who have undergone treatment for the disease. But no biosensor for DJ-1 has been demonstrated, to our knowledge. Here we demonstrate that a new type of biosensor – the Virus BioResistor or *VBR* - that uses virus particles as receptors can be programmed to detect DJ-1 in human urine.

The *VBR* is a bioresistor contacted with two gold electrodes. The bioresistor consists of an electronically conductive channel composed of a layer of poly(3,4-ethylene dioxythiophene) (PEDOT) doped with virus particles. Recently, [44] we demonstrated the *VBR* concept for the detection of human serum albumin (HSA, 66.5 kDa) in high salt (160 mM NaCl) buffer. A limit-of-detection for HSA (LOD_{HSA}) of 7 nM was achieved in that study. [44] However, a sub-1.0 nM LOD for protein markers is required to enable cancer surveillance in urine. Here we unlock higher sensitivity for *VBR*s simply by engineering the PEDOT channel to concentrate the impedance in an ultra-thin (≈90 nm) virus-PEDOT composite layer. With this modification, a limit-of-detection of (LOD_{DJ1}) of 10 pM is achieved in urine (synthetic and human), coupled with a dynamic range of more than four orders of magnitude from 10 pM to 300 nM. This performance is clinically relevant because it allows for the detection of elevated DJ-1 in the urine of patients who have bladder cancer (≈ 100 pM).[60–63] Importantly, the modifications to the *VBR* do not compromise either the speed or the simplicity of its operation. As before[44], the *VBR* operates in a dip-and-read modality, and produces a stable, quantitative signal within 1.0 min. The sensing performance reported here also eclipses prior virus-based biosensors that we have studied over a period of 14 years in our laboratories.[64–68]

The mechanism by which the *VBR* transduces protein binding remains under investigation. A hypothesis presented here proposes that a target protein permeates the virus-PEDOT layer as it undergoes immunoaffinity-driven partitioning to virus particles entrained in this layer. As the volume fraction of electrically insulating proteins increases, the electrical conductivity of the resistor channel imparted by PEDOT is reduced, generating the *VBR* signal.

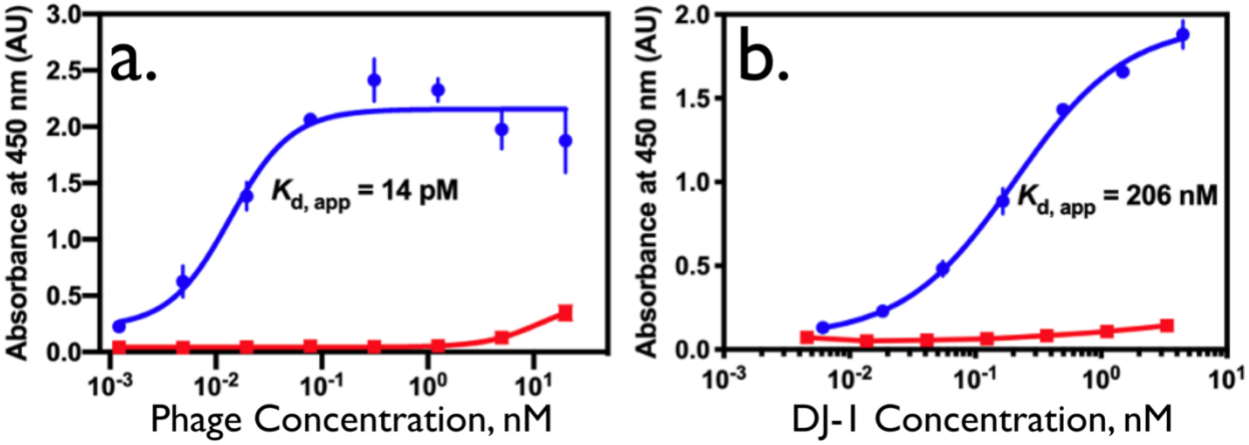

Figure 2.1 - Two ELISAs for M13 phage binding of DJ-1: a) Phage ELISA of the DJ-1-binding phage DL-1 and a negative control Stop4 phage. Here, DJ-1 is immobilized and the DL-1 phage is detected. The data were fit with a four-parameter logistic curve fit (R^2 = 0.9230). Measurements were performed in triplicate; error bars represent the standard deviation of the mean. b) Sandwich ELISA of DJ-1. In this case, DL-1 phage (or the control Stop4 phage) are immobilized and the DJ-1 protein is detected. This format mimics the function of the VBR. The data were fit as described above (R^2 = 0.9944). Measurements were performed in triplicate; error bars represent the standard deviation of the mean.

2.2. Experimental Methods

2.2.1. Materials and Methods

Gold electrodes were prepared by photolithography and physical vapor deposition. The following materials and reagents were purchased commercially and used as received: PMMA cells (Wainamics Inc., Fremont CA) and bare gold electrodes were oxygen plasma-cleaned (PDC-32G, Harrick Plasma). PEDOT-PSS (poly(3,4-ethylenedioxythiophene) polystyrene sulfonate) Heraeus Clevios™ PH1000 from Ossila; lithium perchlorate 99+% purity from Acros organics; EDOT (3,4-ethylenedioxythiophene) from Sigma Aldrich; ethylene glycol from Macron Fine Chemicals. Phosphate buffered saline (PBS, 10x concentrate) from Sigma Aldrich. 1x concentrate of the PBS yielded a phosphate-buffered saline solution at pH 7.4 with a sodium chloride concentration of 0.154 M and a phosphate buffer concentration of 0.01 M. The DJ-1 over-

expression plasmid pET3a-His-DJ1 was a gift from Michael J. Fox Foundation, MJFF (Addgene plasmid #51488). DJ-1 was recombinantly overexpressed in E. coli. Interleukin 6 (IL-6) was purchased from Tonbo Bioscences. M13 phage library design and procedures for the selection of DJ-1 binders using this library are described in the Appendix A.

The affinity of engineered M13 virus particles for DJ-1 can be seen from the results of two enzyme-linked immunosorbent assay (ELISA) measurements (Figure 2.1). The ELISA measurement was conducted two ways: With DJ-1 adsorbed onto a 96 well plate, measuring the recognition of adsorbed DJ-1 by phage particles in solution (Figure 2.1a), and by adsorbing the phage particles on the plate and measuring the binding of DJ-1 to this virus layer (Figure 2.1b). The latter configuration, which yields a much lower apparent dissociation constant, $K_{d,app}$, more closely resembles that situation relevant to the *VBR*.

2.2.2. VBR Fabrication

The fabrication process for the *VBR*s is similar to that described previously [44] with minor modifications. Briefly, gold-film electrodes were cleaned in an O_2 plasma for 10 min immediately before use. Thick (≈70 nm) and thin (≈48 nm) PEDOT-PSS films were prepared as follows: thick PEDOT-PSS films were obtained by stirring a solution of 3% (v/v) ethylene glycol with PEDOT-PSS for 30 min. Thin PEDOT-PSS films were obtained by stirring a solution of 1.5% (v/v) ethylene glycol in PEDOT-PSS for 30 min. These solutions were spin-coated on the gold electrodes at 2500 rpm for 80 s and then heated for 1 h at 90 °C. A PMMA cell was then attached to the PEDOT-PSS film and PEDOT-PSS coated gold electrodes were equilibrated in PBS for 30 min. Next, virus-PEDOT films were electropolymerized onto the PEDOT-PSS/gold-film electrodes using a platinum foil counter and MSE reference electrodes. Virus-PEDOT films were then electrodeposited onto the PEDOT-PSS film from aqueous solutions containing 8 nM M13 bacteriophage, 12.5 mM $LiClO_4$ and 2.5 mM EDOT by performing two voltammetric scans from 0.2 V to 0.8 V vs. MSE at a scan rate of 20 mV/s. A PARSTAT 2263 controlled by Electrochemistry PowerSuit 2.6 software was used for this deposition. All *VBR*s employed for sensing measurements conformed to the screening parameters applied at each step of the fabrication process, as described in detail in the SI. For additional detail, see Figure A.1.

2.2.3. Impedance Spectroscopy (IS)

All solutions were prepared and equilibrated at room temperature (20 °C) prior to IS measurements. The *VBR* cell was first rinsed three times with PBS after which impedance measurements were conducted as follows: Background IS measurement (in triplicate) was acquired in urine (synthetic or human) that contained no added protein, and a second IS measurement (again in triplicate) was acquired in the same urine containing added DJ-1 or IL-6 at the indicated concentrations. The difference in Z_{re} between these two measurements at each frequency is ΔR_{VBR}. The two R_{VBR} inputs to ΔR_{VBR} are obtained by fitting an impedance frequency spectrum that spans the range from 1 Hz to 40 kHz. All IS data were acquired using a Princeton Applied Research PARSTAT Model 2263 controlled by Electrochemistry PowerSuit 2.6 software. 50 data points were acquired across a frequency range of 1 Hz to 40 kHz. The amplitude of the applied voltage was 10 mV for all IS measurements. *VBR*s are single use devices. A different *VBR* was therefore used for each measurement. Equivalent circuit fitting was accomplished using EIS Analyzer (ABC Chemistry). Minimization algorithm Powell (300 iterations) was used to generate values for each circuit element.

2.2.4. Time Scan Experiment

The time scan experiment was performed on four different *VBR*s for four concentrations of DJ-1 protein, 10 pM, 30 pM, 100 pM and 1 nM. Each *VBR* was first equilibrated in synthetic urine for 9 min. A “pure” urine baseline R_{VBR} was then acquired at f = 0.1 Hz for 1.0 min. The synthetic urine was then removed from the PMMA cell and replaced with synthetic urine supplemented with DJ-1 protein at the specified concentration, without disconnecting the *VBR* from the potentiostat. After a one-minute exposure to the test solution, R_{VBR} was again recorded for 10 min.

2.2.5. Control Experiments

Three negative control experiments were undertaken to test for signal specificity. In the first, a Stop-4 M13 virus, which has no displayed peptide binding moieties, was substituted for DJ-1-binding phage. The Stop-4 control *VBR*s were exposed to 500 nM

DJ-1. Second, *VBR*s containing no phage were exposed to 500 nM DJ-1. Interleukin 6 (IL-6, 20.9 kDa, pI = 6.2) that is similar in size and pI to DJ-1, was used as a third control.

2.2.6. SEM Analysis

Scanning electron microscopy (SEM) data were acquired using a FEI Magellan 400L XHR FE-SEM. An accelerating voltage of 2 kV was used for uncoated films and 10 keV for samples coated with 3 nm of iridium.

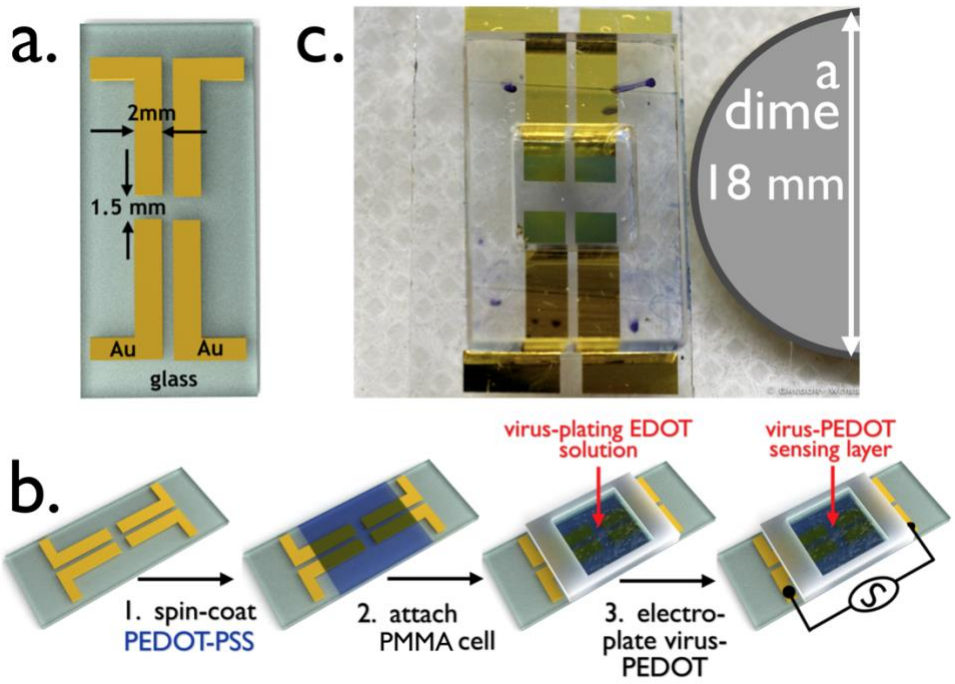

Figure 2.2 - The Virus BioResistor (VBR). a) Rendering of gold electrodes for a two-VBR chip showing its dimensions. The two electrodes at left comprise one VBR and the two on the right a second VBR. These two VBRs will share a single bioaffinity layer. b) The three-step process for fabricating a VBR: Step 1 – a conductive PEDOT-PSS base layer is spin-coated onto the gold-on-glass template shown in (a). This film is baked at 90 °C for 60 min; Step 2 – A poly(methylmethacrylate)(PMMA) cell is attached on top of the dried PEDOT-PSS film; Step 3 – the PMMA cell is filled with aqueous EDOT-virus plating solution, and a virus-PEDOT film is deposited by electrooxidation. This VBR biosensor is ready for use. c) Photograph of a two-VBR chip with PMMA solution cell.

2.3. Results and Discussion

2.3.1. VBR Fabrication and Characterization

Starting with patterned gold electrodes on glass (Figure 2.2a), *VBR*s are prepared in three steps (Figure 2.2b). First, a PEDOT-PSS layer is deposited by spin-coating. Second, a poly(methyl methacrylate) (PMMA) solution cell with adhesive backing is pressed onto

the PEDOT-PSS layer. Third, this solution cell is used to electrodeposit a virus-PEDOT layer. This electrodeposition process applied the following protocol: The *VBR* cell is rinsed with PBS buffer and filled with an aqueous solution of EDOT (2.5 mM), $LiClO_4$ (12.5 mM), and engineered M13 virus particles (8 nM). Using a mercurous sulphate reference electrode (MSE), and a platinum counter electrode, the virus-PEDOT composite layer is electrodeposited onto the PEDOT-PSS surface by scanning its potential (20 mV/s) from +0.20 V to +0.80 V and back versus MSE in two cycles (Figure 2.2a, b). Under these conditions, EDOT is oxidized and the growth of EDOT oligomers proceeds until insoluble cationic PEDOT is precipitated as a film, together with charge-compensating ClO_4^- anions, onto the PEDOT-PSS electrode.[69] If M13 virus is present in the plating solution, virus particles are incorporated into the growing film, a process promoted by the high negative charge density of these particles. At neutral pH, each M13 vision is blanketed with ≈6000 negative charges.[70] Previously, we have demonstrated that the electrodeposition of films from a plating solution containing M13 virus particles and EDOT produces a composite virus-PEDOT film that concentrates virus particles by a factor of 500 times relative to the M13 concentration in the plating solution.[71] As seen in the photograph of a *VBR* shown in Figure 2.1c, the resulting VBR "channel", consisting of a PEDOT-PSS bottom layer and a virus-PEDOT top layer, is transparent.

The *VBR* device architecture and polymeric channel resembles that of an organic electrochemical transistor (OECT).[72,73,74, 75, 76] The differences between these two types of devices are the following: 1). *The VBR is a two-terminal device with no gate electrode.* This simplifies its operation considerably, as the *VBR* measures the impedance of its channel at its rest potential in the analysis solution without the need for gate scans and the requirement for optimization of the gate potential prior to a measurement.[77] The VBR measures an impedance frequency spectrum for the channel, typically across five orders of magnitude in frequency instead of the DC resistance of the channel, as is common practice with EOCTs.[78,79] This impedance data set allows the channel impedance, R_{VBR}, which provides the *VBR* signal, to be cleanly separated from the solution impedance, R_{soln}, which is correlated with the salt concentration of the analysis solution. [44] For bodily fluids such as urine, R_{soln} has the potential to provide information relating to the hydration state of a patient. 3). *VBRs use engineered virus particles as receptors.* Virus particles

may be entrained in a PEDOT film by co-electrodeposition of the virus with the polymer as described above. A fourth difference may be the mechanism of signal generation, as described below.

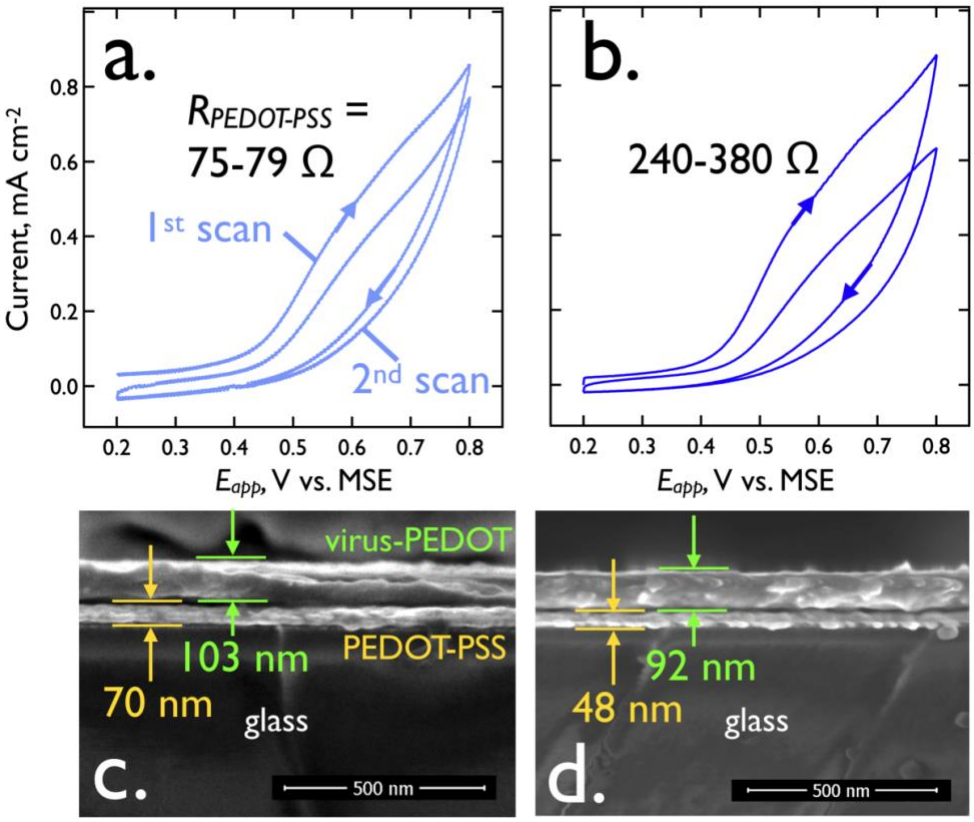

Figure 2.3 - Electrodeposition and SEM cross-sections of virus-PEDOT bioaffinity layers. a). A virus-PEDOT bioaffinity layer is electrodeposited on a PEDOT-PSS base layer using two voltametric scans, as shown. The plating solution is aqueous 2.5 mM EDOT and 12.5 mM $LiClO_4$, 8 nM virus, and the scan rate is 20 mV/s. The DC resistance, $R_{PEDOT-PSS}$, of the PEDOT-PSS layer here is 75 – 79 Ω. b). Same electrodeposition process for a thinner, PEDOT-PSS base layer with $R_{PEDOT-PSS}$ in the range from 240 – 380 Ω. c,d). Cross-sectional SEM images of these two layers show that the more conductive PEDOT-PSS layer ($R_{PEDOT-PSS}$ = 75 – 79 Ω) is 70 nm (± 3 nm) in thickness whereas the less conductive PEDOT-PSS layer is 48 nm (± 2 nm) in thickness. The electrodeposited virus-PEDOT layer is also somewhat thinner in (d) relative to (c) in accordance with the lower deposition currents observed for the second deposition scan.

The architecture and resultant properties of the *VBR* channel dictate its sensing performance. We focus attention here on the importance of the PEDOT-PSS layer thickness and electrical resistance. SEM cross-sectional images (Figure 2.3c,d) show that both polymer layers are tens of nanometers in total thickness. The thickness of the PEDOT-PSS bottom layer is influenced both by the presence of ethylene glycol (EG) in the deposition solution[80,81] and the spin coater speed. The addition of EG is known to

increase the conductivity of PEDOT-PSS by altering its morphology.[82,83] Relatively thick (70 (± 3) nm) low resistance films were obtained using 3% (v/v) EG while high resistance films (48 (± 2) nm) were prepared using 1.5% (v/v) EG (Figure 2.3c,d). The electrical resistance of these layers, $R_{PEDOT\text{-}PSS,}$ is = 75 – 79 Ω (thick) and 240 – 380 Ω (thin). The increased resistance of the PEDOT-PSS bottom layer has little effect on the thickness of the virus-PEDOT top layer electrodeposited on it and the virus-PEDOT top layers had similar thicknesses of 92 (± 4) nm (high PEDOT-PSS resistance) versus 103 (± 4) nm (low resistance). As we demonstrate below, a reduction in thickness of the PEDOT-PSS layer, and an increase in its resistance, boosts the sensitivity of the VBR for the detection of HSA and DJ-1.

Electrodeposited virus-PEDOT and PEDOT-only films have a characteristic topography imparted by PEDOT crystallites protruding by up to a micron from the planar surface of the PEDOT film (Figure 2.4). These “PEDOT stalagmites” are not related to virus particles as they are observed both in the absence (Figure 2.4a, b) and presence (Figure 2.4c, d) of added phage particles. PEDOT stalagmites have attributes of crystallites, including a faceted appearance, as previously reported in the literature. [84,85] In virus-PEDOT films, entrained M13 virus particles appear as black filamentous objects against a gray PEDOT background (Figure 2.4c,d,e). SEM examination of several samples show that the virus concentration within the plane of the virus-PEDOT film is nonuniform with 10 μm^2 - 30 μm^2 regions that are intensely black – indicating high virus concentrations – and other regions that are gray with a relatively low virus concentration. The clustering of virus particles within the film is interesting and surprising, given the high negative charge density of these particles.

2.3.2. VBR Electrical Response and Signal

As previously proposed [44], a simple equivalent circuit containing four circuit elements accounts for the measured frequency-dependent impedance of the *VBR* channel from DC to 40 kHz (Figure 2.5a). In this circuit, the capacitance of the virus-PEDOT/solution interface is represented by a total capacitance, *C.* This capacitance provides coupling between the AC voltage signal applied to the channel and the analyte solution. Three resistors represent the resistance of the analyte solution (R_{soln}), the resistance of the top

polymer layer ($R_{PEDOT\text{-}virus}$) and the resistance of the bottom PEDOT-PSS layer ($R_{PEDOT\text{-}PSS}$).

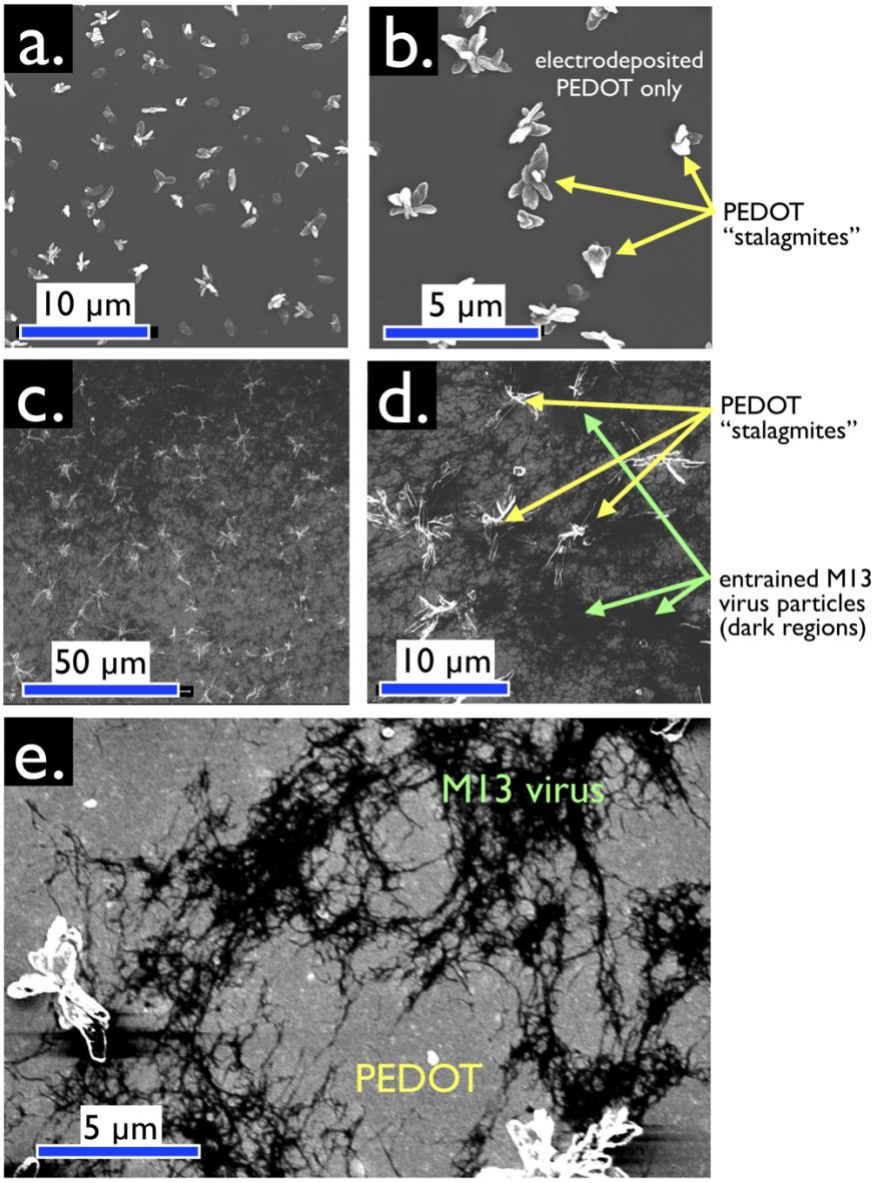

Figure 2.4 - Plan-view SEM images, acquired with secondary electron detection (SED), of virus-free (a,b) and virus-containing (c,d,e) bioaffinity layers. (a,b) Control VBR bioaffinity layer prepared by electrodeposition from a solution containing no virus particles. Micron scale protrusions from the surface of this film are characteristic of electrodeposited PEDOT. These protrusions are not seen at PEDOT-PSS films prepared by spin-coating. We refer to these structures as "PEDOT stalagmites". (c,d,e) VBR bioaffinity layers containing M13 virus particles. Filamentous M13 virus particles comprise the dark regions of these images. Lighter gray regions

contain no virus. PEDOT stalagmites are also observed. Enhanced contrast (e) exposes tangles of M13, again distributed nonuniformly inside a virus-PEDOT bioaffinity layer.

The impedance response of a *VBR* is characterized by a semi-circular Nyquist plot (Z_{im} versus Z_{re}, Figure 2.5b). A qualitative understanding of the *VBR* response is provided by examining its limiting behaviors at low and high frequencies across the range from 1.0 Hz to 40 kHz. At f = 1.0 Hz, the capacitive reactance of the virus-PEDOT/solution interface, ($Z_C = (2\pi fC)^{-1} \approx 6$ kΩ) is larger than R_{VBR} (≈ 2.1–2.7 kΩ, Table 1). So, although R_{soln} is small by comparison to R_{VBR} (289–330 Ω), the value of Z_C strongly attenuates the AC signal that accesses R_{soln}. In this limit, R_{VBR} is approximated by the parallel combination of $R_{PEDOT\text{-}virus}$ and $R_{PEDOT\text{-}PSS}$ (R_{VBR}, Eq. 1).

$$R_{VBR} \approx \frac{(R_{PEDOT-PSS})(R_{PEDOT-virus})}{R_{PEDOT-PSS}+R_{PEDOT-virus}} \quad [1]$$

As shown below and previously,[2] R_{VBR} increases in the presence of a target protein that is bound by virus particles in the virus-PEDOT layer. The difference between R_{VBR} in the presence and absence of this protein is the *VBR* signal, ΔR_{VBR}.

At the high frequency limit, f = 40 kHz, the capacitive reactance approaches zero ($Z_C = (2\pi fC)^{-1} \approx$ 0.15 Ω), and the circuit of Figure 2.6a simplifies to three resistors in parallel:

$$R_{VBR} \approx \frac{(R_{PEDOT-PSS})(R_{PEDOT-virus})(R_{soln})}{R_{PEDOT-PSS}R_{PEDOT-virus}+R_{soln}R_{PEDOT-virus}+R_{soln}R_{PEDOT-PSS}} \quad [2]$$

At f = 40 kHz, R_{VBR} is much lower than at 1 Hz because the small resistor R_{soln} is accessed in parallel to $R_{PEDOT\text{-}PSS}$ and $R_{virus\text{-}PEDOT}$. To a first approximation, the impedance at both of these frequency limits, 1.0 Hz and 40 kHz, is purely resistive but at intermediate frequencies, a significant capacitive component is introduced, producing the characteristic semicircular Nyquist plot that is observed, as seen in Figure 2.6b.

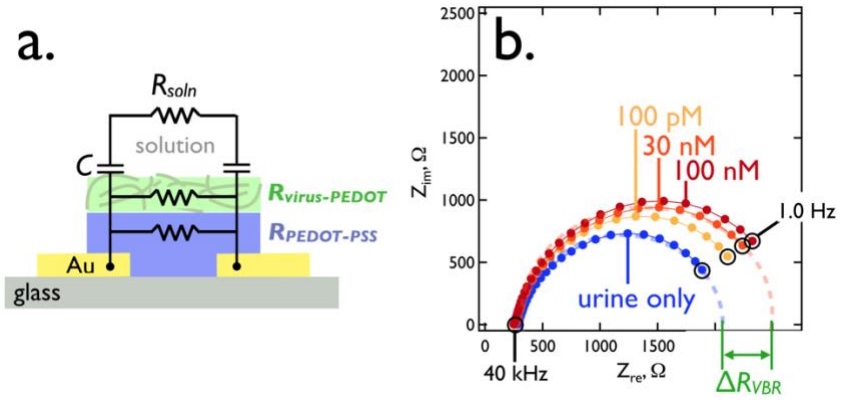

Figure 2.5 - The VBR equivalent circuit (a) and a typical impedance response (b). This Nyquist plot (Z_{im} versus Z_{re}) shows the impedance frequency spectrum plotted between 1.0 Hz and 40 kHz for a synthetic urine solution that was supplemented with DJ-1. A single VBR measured these solutions at the indicated DJ-1 concentrations.

The values of *C*, R_{soln}, and R_{VBR} (encompassing $R_{PEDOT-virus}$ and $R_{PEDOT-PSS}$) are obtained by deconvolution of the complex impedance data set. How do R_{VBR}, R_{soln}, and *C*, change in response to the concentration of a target protein? For DJ-1 concentrations from 0 – 100 nM, variations of R_{soln} are constant within the error bars for this measurement and are independent of DJ-1 concentration (Table 2.1). The capacitance, *C,* approximated as a constant phase element (CPE, $Z_C \approx Z_{CPE} = -\frac{1}{Q(i\omega)^n}$), varies weakly with the DJ-1 concentration (Table 2.1). R_{VBR} at low frequency, in contrast, is strongly correlated with the DJ-1 concentration and, as already indicated, ΔR_{VBR}, is used to transduce the concentration of a target protein bound by entrained virus particles (Table 2.1).

Table 2.1 - VBR circuit element values, and $\Delta R_{VBR,}$ corresponding to the Nyquist plots of Figure 2.5b.

	Synthetic Urine		100 pM DJ-1		30 nM DJ-1		100 nM DJ-1	
	value	st dev	value	st dev	value	st dev	value	st dev
R_{sol} (Ω)	331	8	288.7	0.9	293	7	279.3	0.2
R_{VBR} (Ω)	2156	1	2436	5	2641	4	2733	8

ΔR_{VBR} (Ω)	0		280		485		577	
[a]CPE, *Q* (F)	2.77 x 10^{-5}	0.03 x 10^{-5}	2.59 x 10^{-5}	0.01 x 10^{-5}	2.65 x 10^{-5}	0.02 x 10^{-5}	2.520 x 10^{-5}	0.009 x 10^{-5}
[a]CPE, *n*	0.84	0.00	0.85	0.00	0.85	0.00	0.86	0.00

[a]Constant phase element (CPE) approximation of the capacitance, *C*.[86] $Z_{CPE} = -\frac{1}{Q(i\omega)^n}$. The phase angle, Θ, of the impedance response is, $\Theta = -(90^*n)°$, with $0 > n > 1$. $n = 1$ corresponds to ideal capacitor behavior.

Since, as noted above, the VBR signal ΔR_{VBR} is best measured at low frequency, wouldn't it be simpler to use the DC resistance of the VBR channel to derive signal? In practice, the DC measurement does work, but there are two reasons for measuring the frequency spectrum instead: 1). In DC sensing mode, one does not acquire the high frequency impedance (Eq. 2) that permits deconvolution (and measurement) of the solution resistance from the ΔR_{VBR} signal. 2). The reproducibility of the impedance at low frequency is better than for a DC measurement. That is, the signal-to-noise at low frequencies down to 1 Hz is higher than the noise at DC (data not shown).

2.3.3. Tuning the VBR Signal Amplitude Using $R_{PEDOT\text{-}PSS}$

Eq. [1] predicts that at low frequencies, increasing $R_{PEDOT\text{-}PSS}$ causes R_{VBR} to converge on $R_{PEDOT\text{-}virus}$ (Figure 2.6a). If ΔR_{VBR} is generated by the virus-PEDOT top-layer, then an increase in $R_{PEDOT\text{-}PSS}$ should increase *VBR* sensitivity. This expectation is confirmed by measurement of ΔR_{VBR} for the protein human serum albumin, HSA, a 66.5 kDa protein that is a marker for renal failure (Figure 2.6). A plot of ΔR_{VBR} *versus* $R_{PEDOT\text{-}PSS}$ for [HSA] = 100 nM shows that increasing $R_{PEDOT\text{-}PSS}$ is from 70 Ω to 380 Ω by reducing thickness of this layer, increases the ΔR_{VBR} from 40 Ω to more than 500 Ω (Figure 2.6b).

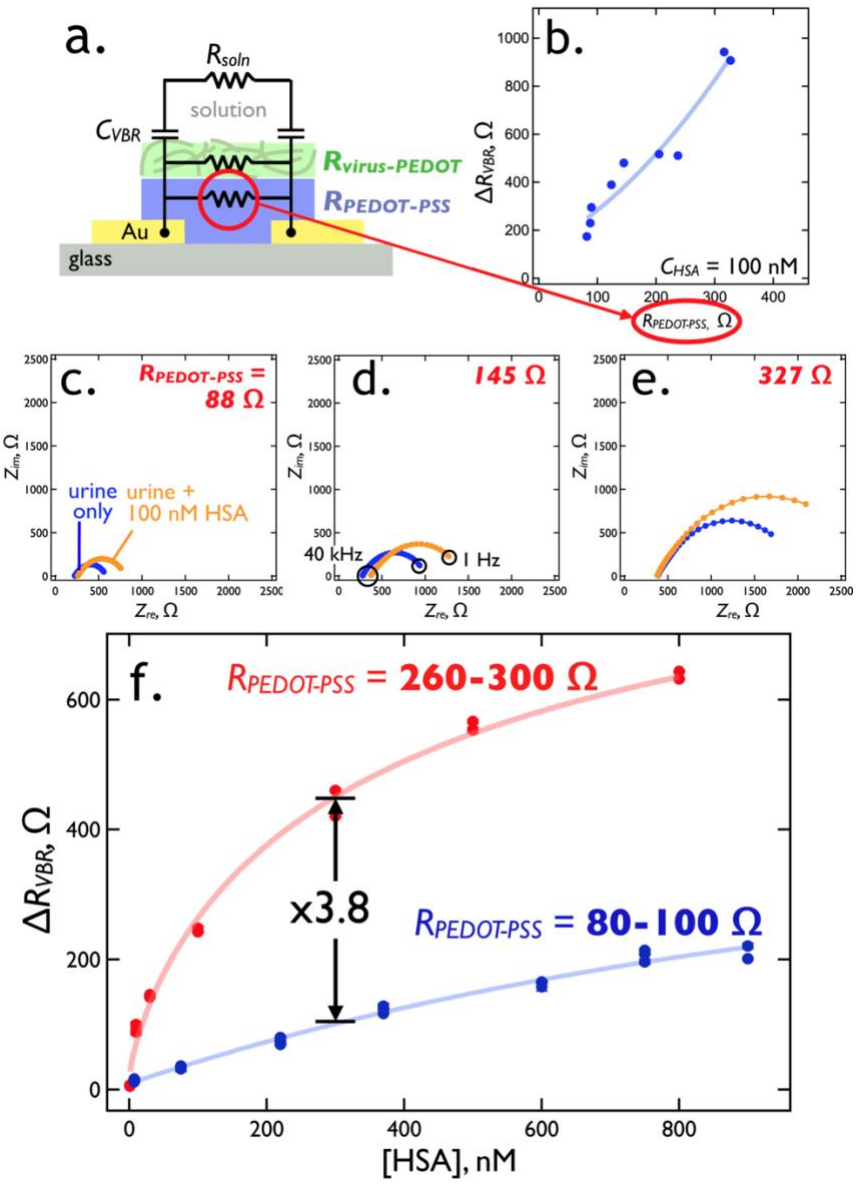

Figure 2.6 - $R_{PEDOT-PSS}$ tuning of the VBR sensitivity for HSA. (a) The equivalent circuit for the VBR places the electrical impedance of the virus-PEDOT layer, R_{VBR}, in parallel with that of the PEDOT-PSS bottom layer, $R_{PEDOT-PSS}$, forming a current divider. (b) Increasing $R_{PEDOT-PSS}$ from 80 Ω to 300 Ω, by reducing the PEDOT-PSS layer thickness, forces current, i, through the virus-PEDOT measurement layer, increasing the signal for 100 nM HSA by a factor of 3 to 5 from 200 Ω to more than 900 Ω. (c,d,e) Three Nyquist plots corresponding to three values of the resistor, $R_{PEDOT-PSS,}$ as indicated. In each plot, impedances are plotted in the complex plane from 1 Hz (right) to 40 kHz (left). A shift in the low frequency Z_{re} from synthetic urine only (blue trace) to 100 nM DJ-1 (orange trace) approximates the signal, ΔR_{VBR}. (f) R_{VBR} versus [HSA] calibration plots for a series of 42 VBR sensors (21 in each plot) with $R_{PEDOT-PSS}$ values in the range from 80 to 100 Ω and 260 to 300 Ω. The higher $R_{PEDOT-PSS}$ devices produce 3 to 5 times more signal amplitude across the HSA binding curve.

Nyquist plots for three $R_{PEDOT\text{-}PSS}$ values (Figure 2.6c,d,e) document the increase in sensitivity for three *VBR*s. It should be noted that $R_{PEDOT\text{-}PSS} \approx 300\ \Omega$ is a practical upper limit in our experiments. Attempts to further thin the PEDOT-PSS layer to achieve even higher sensitivities resulted in pronounced irreproducibility in both $R_{PEDOT\text{-}PSS}$ and measured ΔR_{VBR} values.

Two calibration plots for HSA in PBS buffer solution acquired using *VBR*s compare the performance of high resistance PEDOT-PSS layers, ($R_{PEDOT\text{-}PSS}$ = 260 - 300 Ω) with low resistance PEDOT-PSS layers ($R_{PEDOT\text{-}PSS}$ = = 80 - 100 Ω, Figure 2.6f). The ΔR_{VBR} signal for HSA increases by between 10x (at low concentrations) to 3x (at high concentrations) across the HSA concentration range encompassed by these data.

$R_{PEDOT\text{-}PSS}$ tuning of the *VBR* sensitivity also works for DJ-1 – a bladder cancer marker that is significantly smaller than HSA (20.8 kDa versus 66.5 kDa). Again, a plot of ΔR_{VBR} *versus* $R_{PEDOT\text{-}PSS}$ for a concentration of DJ-1 of 100 nM in synthetic urine shows that increasing $R_{PEDOT\text{-}PSS}$ from 75 Ω to 300 Ω increases ΔR_{VBR} from 50 Ω to 550 Ω (Figure 2.7a). Nyquist plots for three $R_{PEDOT\text{-}PSS}$ values (Figure 2.7b, c, d) document the increase in sensitivity for three *VBR*s.

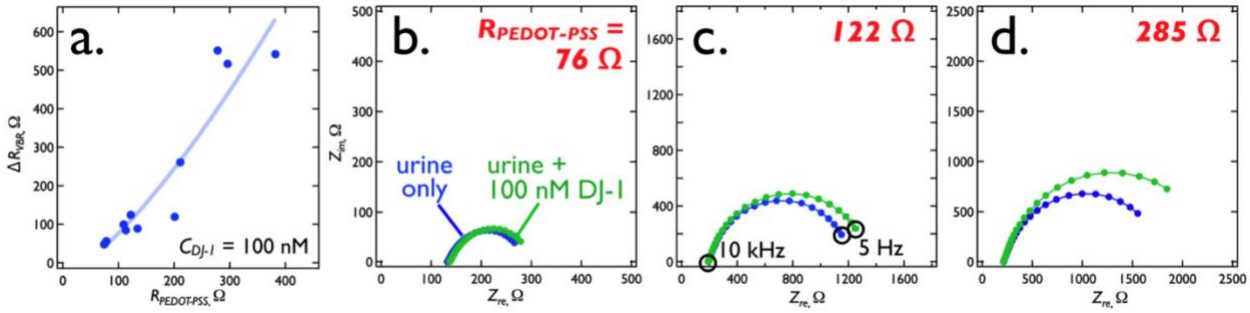

Figure 2.7 - $R_{PEDOT\text{-}PSS}$ tuning of the VBR sensitivity for DJ-1. (a) Increasing $R_{PEDOT\text{-}PSS}$ from 80 Ω to 300 Ω, by reducing the PEDOT-PSS layer thickness increases the signal for 100 nM DJ-1 by a factor of ≈10 from 50 Ω to 550 Ω. (b,c,d) Three Nyquist plots corresponding to three values of the resistor, $R_{PEDOT\text{-}PSS}$, as indicated. In each plot, impedances are plotted in the complex plane from 1 Hz (right) to 40 kHz (left). A shift in the low frequency Z_{re} from synthetic urine only (blue trace) to 100 nM DJ-1 (green trace) approximates the signal, ΔR_{VBR}.

Looking more carefully at the DJ-1 sensing performance of VBRs with high resistance PEDOT-PSS layers ($R_{PEDOT\text{-}PSS} \approx 300\ \Omega$) Nyquist plots (Figure 2.8a, b, c) show the accessible DJ-1 dynamic range extends from a limit-of-detection of 10 pM to 300 nM – a range of more than four orders of magnitude (see values of all circuit elements for these three *VBR* sensors in Table A.1). A plot of ΔR_{VBR} *versus* DJ-1 concentration across

this same range for a total of 35 *VBR* sensors (Figure 2.8d) conforms to the Hill Equation:[87]

$$\Delta R_{VBR} = \Delta R_{VBR,0} + \frac{\Delta R_{VBR,lim} - \Delta R_{VBR,0}}{1 + \left(\frac{K_D}{[\mathrm{DJ-1}]}\right)^h} \quad [3]$$

A best fit of equation [3] to these data yields the following parameter values: $\Delta R_{VBR,lim}$ = 950 ± 640 Ω, $\Delta R_{VBR,0}$ = 50 ± 140 Ω, K_D = 39 ± 170 nM, h = 0.3 ± 0.2, and R^2 = 0.94. It should be noted that these data encompass measurements of DJ-1 in synthetic urine (21 sensors) and in pooled human urine (14 sensors). Each of these *VBR*s was used for a single DJ-1 concentration data point in Figure 2.8d. The measured value of h indicates strong negative cooperativity, meaning that the microscopic dissociation constant, K_D, is increased (the affinity interaction is reduced) as the fraction of binding sites occupied by the target protein increases.[87] This has the effect of stretching the binding curve across a wider range of DJ-1 concentration range – exceeding four orders of magnitude in the present case (Figure 2.8d).

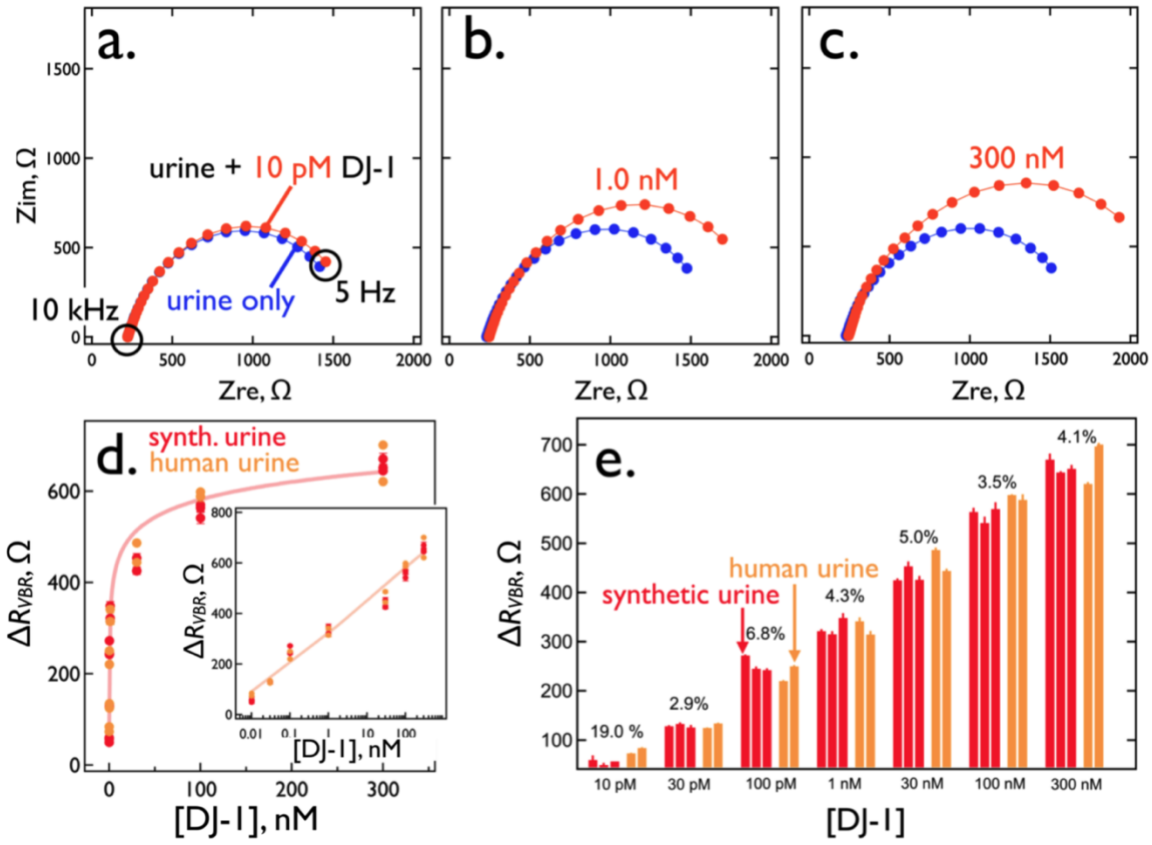

Figure 2.8 - DJ-1 sensing performance using VBRs with $R_{PEDOT-PSS}$ = 280 to 300 Ω. (a,b,c) Nyquist plots for three DJ-1 concentrations of (a) 10 pM, (b) 1 nM, and (c) 300 nM. Also shown (blue traces) are background Nyquist responses in synthetic urine only. (d) A calibration curve for the detection of DJ-1 using the R_{VBR} signal constructed using 21 individual measurements from the same number of VBRs, at seven concentrations. Values of K_D and h (the Hill exponent) obtained from a best fit of the experimental data to equation (2), are indicated. (e) Bar plot for ΔR_{VBR} measurements acquired from 21 electrodes, illustrating the sensor-to-sensor reproducibility of these data. CoVs for these data, shown, are in the 2 to 8% range across four orders of magnitude in DJ-1 concentration. The values of each of the circuit elements is indicated in Table A.1.

In principle, the absence of a gate and an applied gate potential referenced to an external reference electrode, leaves open the possibility of potential drift of the channel that could drive doping and de-doping reactions of the PEDOT sensing layers, causing baseline drift of the sensor and degrading reproducibility of the concentration measurements. But the data of Figure 2.8e shows that this "channel conductivity drift" is inconsequential on the time scale of 1-2 minutes required for carrying out VBR measurements of concentration. To this end, we made measurements of DJ-1 conducted in triplicate (for synthetic urine) and duplicate (for human urine) document the reproducibility of *VBR*s (Figure 2.8e). Sensor-to-sensor coefficients-of-variation (CoV) vary from 2.9% (30 pM), to 4.1% (300 nM), extraordinarily low values. As expected, at the 10 pM LOD, a higher CoV of 19% is obtained. It should be noted that *VBR*s are effectively single use devices, because the off-rate for bound DJ-1 after a single exposure is several hours (data not shown). This means that individual *VBR*s cannot be calibrated; every *VBR* sensor must respond to the same calibration curve placing a premium on the sensor-to-sensor reproducibility.

Nonspecific adsorption at the unmodified virus-PEDOT surface of a *VBR* is negligible, contributing to the simplicity of *VBR* fabrication (Figure 2.2b). Blocking, often accomplished by pre-equilibrating a bioaffinity layer with solutions of bovine serum albumin (BSA), casein,[88,89,90] or poly(ethylene glycol),[91] prior to exposure to a target protein, is not required. Three sets of negative controls (Figure 2.9a) for *VBR*s containing no phage, *VBR*s prepared using Stop-4 phage (which has no displayed peptides at its surface), and *VBR*s prepared using DJ-1 binding phage in the presence of Interleukin 6 or IL-6 (a protein of similar size, 20.9 kDa, and pI, 6.2 versus 6.7 for DJ-1) - either produce no measurable signal or a small "negative" signal, corresponding to a negative value of ΔR_{VBR} (Figure 2.9a).

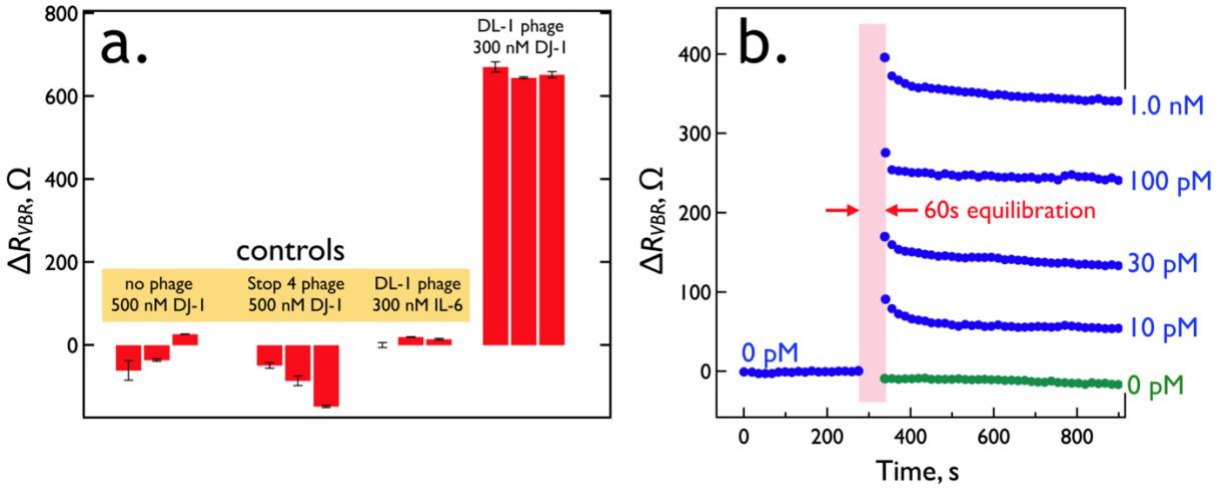

Figure 2.9 - VBR specificity and speed. (a) Three control experiments: At left is the response of three VBRs prepared with no phage exposed to 500 nM DJ-1. To the right of this is the response of three VBRs prepared with Stop-4 phage that has no displayed peptides on its surface. Finally, at right are shown the results of three VBRs containing DL1 phage (selected for the binding to DJ-1) upon exposure to IL-6, a protein of similar MW (20.9 kDa) and pI (6.2) to DJ-1 (20.7 kDa and pI of 6.7, respectively). (b) Real-time VBR sensing data. Responses for five VBR sensors are shown for DJ-1 exposures of 0 pM (green trace), 10 pM, 30 pM, 100 pM, and 1.0 nM. These traces were obtained by first stabilizing sensors in synthetic urine for 9 min, measuring a R_{VBR} baseline at 0.10 Hz, and then interrupting for 1.0 min while the synthetic urine was replaced with synthetic urine supplemented with DJ-1 at the specified concentration, after which ΔR_{VBR} signal was acquired.

Analysis speed and simplicity of operation are two requirements for biosensors that are used either at the point-of-care (PoC) or outside a care facility, at a point-of-need (PoN).[92,93] The *VBR* provides for detection of DJ-1 across a range of concentrations within one minute in a dip-and-read modality (Figure 2.9b). Thus, the *VBR* is well-adapted to PoC and PoN applications.

The frequency-dependent signal-to-noise ratio (S/N) for the *VBR* (Figure 2.10a) increases with decreasing frequency from 40 kHz to 1.0 Hz. In this measurement, noise is defined as the standard deviation of repetitive measurements (N = 3) for ΔR_{VBR} (the signal) at a defined concentration of target protein. At a DJ-1 concentration of 300 nM, S/N peaks at 150 at 1.0 Hz and decreases to 60 at 100 pM and 4 at 10 pM, the limit-of-detection. S/N ratios at 40 kHz, in contrast, are in the range from 2 to 14 for this range of DJ-1 concentration. Consistent with the equivalent circuit of Figure 2.5a, increasing frequency reduces the impedance of the virus-PEDOT solution capacitance, Z_C, opening a low impedance path through the analyte solution, R_{soln} and by-passing the signal-generating current path of the channel. It should be noted that the S/N versus frequency

data sets (Figure 2.10a) are themselves noisy. Repeated measurements of these data shows that the sharp peaks and valleys seen in these traces are not reproduced. This means that there are temporal variations in the noise present in the *VBR* circuit. However, the trend of increasing S/N with decreasing frequency remains prominent in these data.

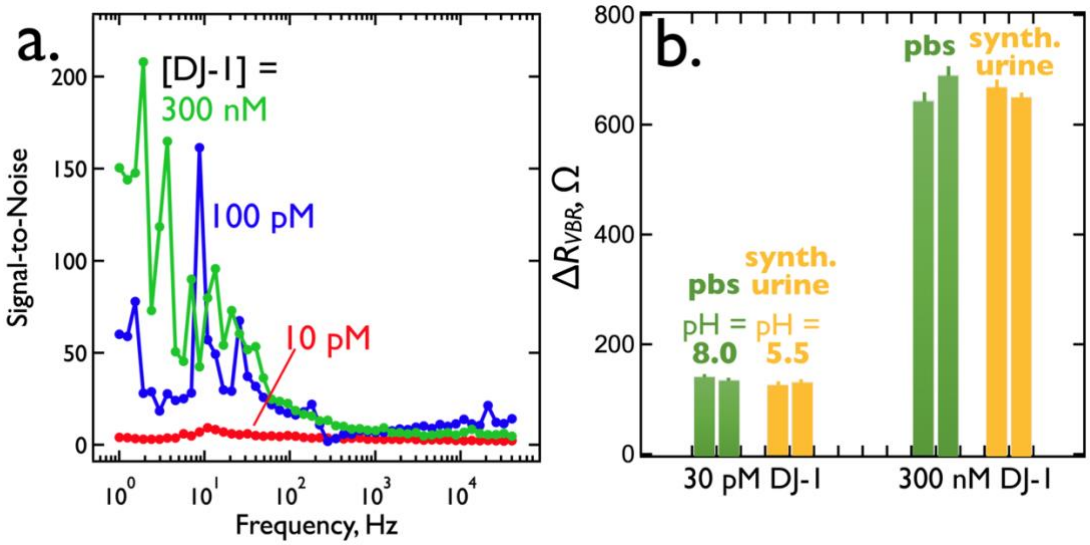

Figure 2.10 - (a) Signal-to-noise (S/N) versus frequency for the detection of DJ-1. Shown are three plots of S/N versus frequency measured for three VBRs immersed in three DJ-1-spiked synthetic urine solutions containing DJ-1 at the indicated concentrations. Noise is calculated as the standard deviation of three replicate measurements at each frequency. S/N consistently increases from high to low frequencies. (b) Comparison of ΔR_{VBR} for the detection of DJ-1 in two electrolytes: synthetic urine (pH = 5.5) and PBS buffer (pH = 8.0). The charge state of DJ-1 (pI = 6.7) inverts across this pH difference, and is negatively charged at pH = 8.0 and positively charged at pH = 5.5. However, ΔR_{VBR} at two different concentrations are the same, despite changes in pH, within the reproducibility of these measurements.

2.3.4. A Proposed Mechanism for VBR Signal Generation

The mechanism by which the *VBR* produces an impedance increase in the presence of target protein is of interest. This mechanism must account for three experimental observations: 1). ΔR_{VBR} is positive. In particular, the sign of the protein charge, positive or negative, has no influence on the signal. For example, DJ-1 (pI = 6.7) can be measured both at pH = 5.5 and at 8.0, corresponding to a positively charged protein, and a negatively charged protein, respectively (Figure 2.10b). ΔR_{VBR} signal is unaffected by this charge inversion. 2). *VBR* signal is insensitive to the salt concentration of the test solution. Previously, [44] we demonstrated this for the detection of 75 nM HSA in salt solutions ranging from 134 mM to 670 mM NaCl where no significant change in HSA signal was observed. Collectively, (1) and (2) imply that a charge gating mechanism,

responsible for signal in field-effect transistors,[94] cannot be operating in *VBR*s. 3) The signal-to-noise ratio is strongly frequency dependent - S/N is high at low frequency (≈ 1 Hz) and near zero at high frequency (≈ 40 kHz) where it is also independent of the concentration of a target protein. The implication is that the signal generating process does not require the transmission of AC signal through electrolyte. This includes electrolyte that is present in the voids within the porous virus-PEDOT signal-generating layer. Thus, R_{VBR} decreases by just 24 Ω or 4% (against a background of 600 Ω) in protein-free aqueous NaCl as C_{NaCl} is increased by a factor of 50 from 0.02 M to 1.00 M (Figure A.2).

A simple mechanism that may account for these observations is shown schematically in Figure 2.11. Here, just the virus-PEDOT layer is illustrated. The virus-PEDOT layer itself is semi-crystalline, containing crystalline PEDOT-only domains surrounded by disordered domains that contain disordered PEDOT chains and, likely, most of the virus particles (Figure 2.11a). Electrical conduction within this layer occurs by two processes: i) intrachain charge transport (via bipolarons) and, ii) interchain electron hopping (Figure 2.11a). Interchain hopping, in particular, can be disrupted by the partitioning of protein into this layer, promoted by the immunoaffinity partitioning of target protein by virus particles entrained in the virus-PEDOT film.[95]

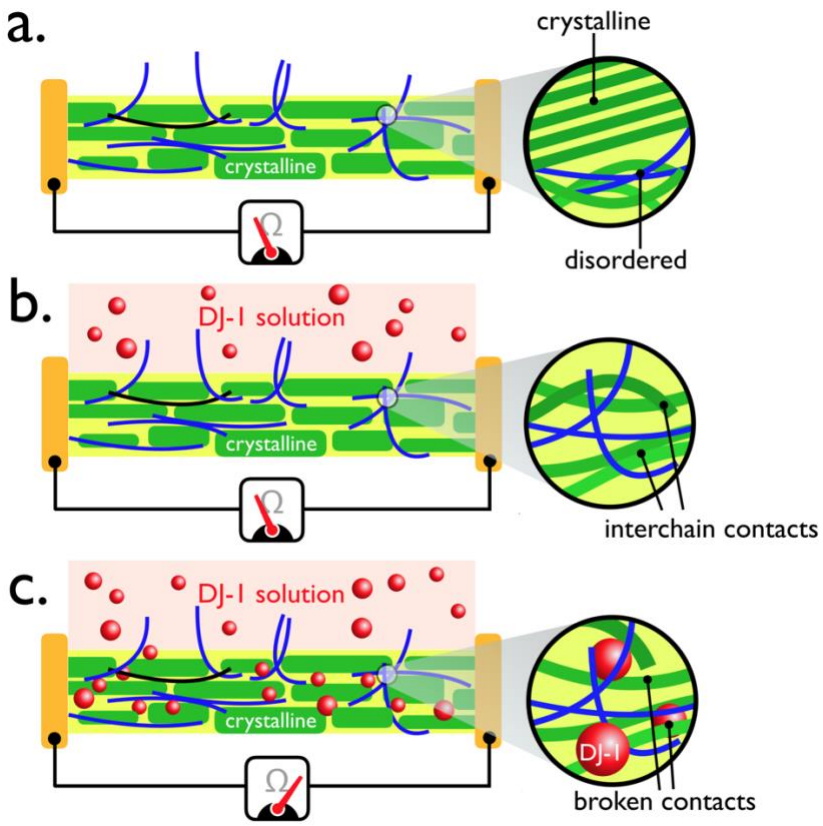

Figure 2.11 - Schematic representation of a hypothesized signal transduction mechanism for the VBR. (a) The virus-PEDOT layer shown here consists of semi-crystalline PEDOT with virus particles that are concentrated within disordered regions of the PEDOT layer, (b) When exposed to the DJ-1 protein solution, ΔR_{VBR} is initially zero, because an induction time is associated with the rate-limiting diffusion of the protein into the virus-PEDOT layer. (c) Permeation of the virus-PEDOT layer by DJ-1 is associated with an increase in its resistance as the insulating protein interferes with conduction pathways within this layer.

This mechanism is analogous to that proposed for chemiresistive gas sensors that exploit a carbon/polymer composite chemiresistor.[96–100] In these systems, permeation of a carbon/polymer (insulating) composite by a molecule in the vapor phase causes an increase in the volume of the composite and a decrease in the volume fraction of the conducting carbon phase, leading to a reduction in the conductivity of the composite, a process that is described by percolation theory:[101,102]

$$\sigma = \sigma_0[V - V_c]^{\alpha} \qquad [4]$$

Where σ_0 is the conductivity of the composite in the absence of permeating vapor species, σ is the conductivity of the composite after exposure to this vapor, V is the volume fraction

of the conductive component of the composite, V_c is the volume fraction of the conductive phase at the percolation threshold, and α is a scaling exponent that depends only on the dimensionality of the percolation process (2 dimensional or 3 dimensional). Eq (4) is intended to model the conductivity at values of V near the percolation threshold, but more generally, it provides a signal transduction mechanism for chemiresistors in which the resistor is comprised of a nonconductive and a conductive component and for which permeation of analyte(s) induces swelling of this system.

The mechanism depicted (Figure 2.11) requires that target protein diffuses into the virus-PEDOT layer. Does this occur on the one-minute time-scale of signal generation, and if so, what mass loading of protein is obtained in this layer during this brief period? These questions can be addressed using quartz crystal microbalance (QCM) gravimetry. In this measurement, a two-layer PEDOT-PSS + virus-PEDOT bioaffinity layer is prepared on a QCM crystal coated with a thin photoresist layer. Exactly the same processes used for *VBR* fabrication (Figure 2.12a), involving the PVD deposition of gold electrodes, spin-coating of the PEDOT-PSS layer, and electrodeposition of the virus-PEDOT layer, are used for the preparation of these layers, for these experiments, the gold electrodes are not used to make electrical measurements.

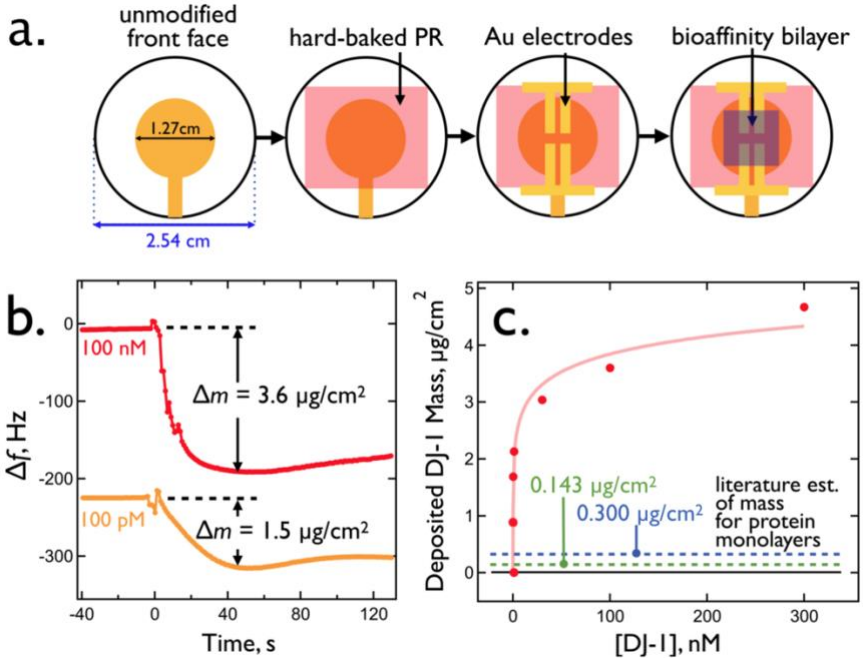

Figure 2.12 - Measurement of DJ-1 mass loading for VBR bioaffinity layers using quartz crystal microbalance (QCM) gravimetry. (a) Four step fabrication of a complete VBR bioaffinity layer on a commercial QCM crystal. (b) Change in frequency, Δf, versus time for the exposure of two

VBRs to solutions of DJ-1 at 100 pM and 100 nM. The measured DJ-1 mass loading is indicated and traces are shifted along the Δf axis for clarity. (c) The concentration of DJ-1 versus its measured mass loading. This isotherm was acquired in PBS buffer solution.

Upon exposure to DJ-1 solutions, the resonant frequency, f_R, decreases within seconds and stabilizes within ≈40-60 s (Figure 2.12b) Using the Sauerbrey Equation[103] the observed frequency change, Δf, can be translated into a mass change, Δm:

$$\Delta f = -\frac{f_R}{\rho_q d A}\Delta m \qquad [5]$$

where f_R is the resonant frequency of the quartz crystal oscillator in air, ρ_q, is the density of this crystal, d is its thickness, and A is the area of the gold electrodes deposited onto this crystal.

A plot of Δm *versus* DJ-1 concentration shows saturation behavior resembling the *VBR* calibration plot for DJ-1 (Figure 2.8d). The mass loading saturates at ≈ 4 μg/cm^2 which corresponds to more than 1.0 monolayer of DJ-1 at the surface of the virus-PEDOT layer - even if this layer has significant roughness. For purposes of comparison, the mass of a hydrated protein monolayers has been measured using QCM for several proteins including RNAase (13.7 kDa, 300 ng/cm^2 on silica), bovine serum albumen (66.5 kDa, 150 ng/cm^2 on silica)[104], and human serum albumin (66.5 kDa, 230 ng/cm^2 on oxidized gold)[105] An estimate of the mass of a closest packed DJ-1 monolayer can also be derived from the dimensions of this protein previously reported using single crystal x-ray diffraction[106]. The refined crystallographic data includes 323 structural water molecules per DJ-1 protein, which should be considered a lower bound to the actual water content of this system. The mass of this monolayer is predicted to be 146 ng/cm^2.

The low end (146 ng/cm^2) and high end of these estimates (300 ng/cm^2) are indicated by dashed lines in Figure 2.12c. Based upon these numbers, the ≈4 μg/cm^2 plateau measured for DJ-1 corresponds to 13-27 equivalent protein monolayers. These data are consistent with permeation of DJ-1 into the virus-PEDOT layer, and perhaps the PEDOT-PSS layer as well, on the one-minute time scale as required by the mechanism depicted in Figure 2.11.

Finally, it is useful to confirm that the diffusion coefficient, D_{DJ-1}, required for DJ-1 permeation by diffusion in one minute is physically realistic. D_{DJ-1} can be estimated using the equation:[107] $D_{DJ-1} = T^2/2t$ where T is the total thickness of the two-layer channel (≈ 150 – 170 nm) and t is the time required for diffusive permeation of DJ-1 (≈60 s) which we estimate as the time required for signal generation. The range of calculated D_{DJ-1} values is (1.9 – 2.4) x 10^{-12} cm^2/s, which is approximately 5-6 orders of magnitude slower than the diffusion coefficient for proteins of this size (D ≈ 10^{-7} - 10^{-6} cm^2/s)[108] in aqueous electrolyte solutions, qualitatively as expected. Potentially, the estimates of T, derived from SEM data (Figure 2.3), could be too low because these values pertain to dried films. However, doubling the estimate of T (≈ 300 – 340 nm) produces D_{DJ-1} values of (7.5 – 9.6) x 10^{-12} cm^2/s within an order of magnitude of the dried values.

To test the signal transduction mechanism for VBRs proposed here, simultaneous measurements of the electrical impedance and direct QCM measurements of the mass loading of protein, are required for comparison with the predictions of Eq. [4]. We expect to carry out these measurements soon.

2.4. Summary

The *VBR* is a biosensor that exploits direct electrical communication with virus particles to measure the concentration of protein biomarkers for cancer and disease. These virus particles, which are engineered to recognize and bind a target protein of interest, are entrained within an electrodeposited virus-PEDOT film. The electrical impedance of this film directly produces the signal required for protein quantitation, eliminating the need for any additional amplification. In addition, no reagents such as redox couples are required for these measurements.

The conductive polymer bilayer comprising the *VBR* channel can be engineered to adjust its sensitivity. In particular, a reduction in the thickness of the PEDOT-PSS bottom layer from 70 nm to 48 nm significantly increases the resistance of this layer, from ≈80 Ω to ≈300 Ω increasing the *VBR* signal for HSA (66.5 kDa) by a factor of 3x to 10x. Applying this strategy to the detection of a smaller protein, DJ-1 (20.8 kDa) enables the measurement of this bladder cancer marker at concentrations down to 10 pM using a measurement time of 1.0 min. in a dip-and-read modality. The extreme simplicity of the

VBR allows for its fabrication in three steps, contributing to excellent sensor-to-sensor reproducibility characterized by CoVs below 7% down to 30 pM for DJ-1, across the entire DJ-1 binding curve spanning four orders of magnitude in concentration.

Direct *QCM* measurement of the mass of the bioaffinity bilayer demonstrates that the equivalent of multiple (>10) monolayers of DJ-1 protein are able to diffuse into this layer from solution within one minute, a process that coincides temporally with the generation of the *VBR* impedance signal. The resulting QCM binding curve for DJ-1 resembles the binding curve measured by the *VBR* for this protein. Based upon this observation as well as other evidence, a simple model is proposed for signal transduction involving the dilution of the PEDOT conductor by insulating protein molecules resulting in an increased resistance for this layer, a mechanism analogous to that operating in carbon/polymer chemiresistor gas sensors.

Chapter 3: Enhancing the Sensitivity of the Virus BioResistor by Over -Oxidization: Detecting IgG Antibodies.

This chapter is adapted from a research article “Enhancing the Sensitivity of the Virus BioResistor by Overoxidation: Detecting IgG Antibodies”.

3.1. Introduction

Biosensors capable of rapid, sensitive quantitation of protein disease markers in a variety of bodily fluids at the point-of-care could aid in the diagnosis of disease and improve prognoses.[109–111] The Virus BioResistor or VBR is a biosensor that exploits engineered virus particles (Figure B.1) as receptors to detect proteins. The device's simple chemiresistor device architecture consists of embedded virus particles in a two-layer polymeric channel consisting of a conductive poly(3,4 ethylenedioxythiophene)-poly(styrene sulfonate) or PEDOT-PSS bottom layer prepared by spin coating, and an electrodeposited virus-PEDOT top sensing layer. [43,44] We recently demonstrated that VBRs can be used to detect the bladder cancer marker DJ-1 (MW of 22 kDa) with a limit-of-detection, LOD_{DJ-1}, of 10 pM in human urine. However, the VBR is less sensitive to a larger protein, human serum albumin (HSA, 66 kDa), where a LOD_{HSA} of 7.5 nM has been achieved. [43,44] The reduced sensitivity of the VBR can be traced to reduction of the signal, DR_{VBR}, for measurements of HSA compared to DJ-1 (Figure 3.1). This depressed sensitivity of HSA relative to DJ-1 is observed across the entire VBR dynamic range for the detection of these two proteins.

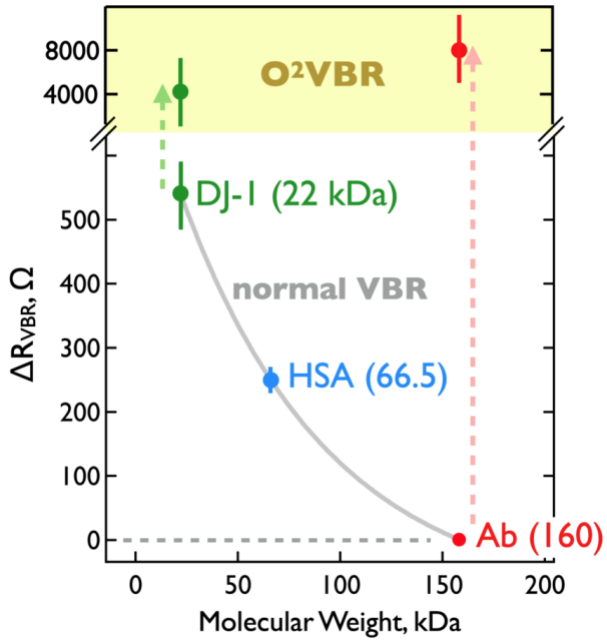

Figure 3.1 - Larger proteins produce less VBR signal. The signal, ΔR_{VBR}, produced by optimized VBRs for three proteins at 100 nM in buffer versus the molecular weight of these proteins. The over-oxidation process described here produces O^2VBRs that generate significantly more signal

for both large and small proteins. DJ-1 = protein deglycase, [43] HSA = human serum albumin, [44] Ab = IgG antibody.

IgG antibodies (MW of 150 kDa) pose a more challenging problem for the VBR as follows. No signal at all is observed in buffer solutions containing significant concentrations (>300 ng/mL or 1.8 nM) of these large proteins (Figure 3.1). Together with the data for DJ-1 and HSA, these observations define a trend toward lower VBR sensitivity with increasing protein size. This trend could represent a serious limitation for the practical use of VBRs in point-of-care diagnostics.

Recently, [44] we reported that the sensitivity of VBRs can be enhanced by reducing the thickness of the PEDOT-PSS bottom layer from 70 nm (±3 nm) to 48 nm (±2 nm). This modification enhances the signal amplitude for HSA by a factor of 3-5 across the entire HSA calibration curve. [44] However, this strategy for signal enhancement is limited: 48 nm is the minimum thickness possible for PEDOT-PSS layers prepared by spin-coating in our laboratory. It should be noted that all of the "normal" VBR data discussed in this manuscript pertain to the use of VBRs prepared using such ultra-thin, 48 nm (±2 nm), PEDOT-PSS layers. [44] The extra sensitivity conferred by this modification is not sufficient to enable the detection of antibodies by VBRs.

A second method for increasing signal amplitudes is described here. It is demonstrated that the electrochemical processing of the VBR channel can significantly increase the signal amplitudes produced by VBRs – beyond the enhancement provided by ultra-thin PEDOT-PSS layers – for both small and large proteins. In this electrochemical process, the VBR channel is subjected to irreversible electrochemical oxidation, or "over-oxidation" [112–116], resulting in an "O^2VBR". Here, the efficacy of over-oxidation for "amplifying" signals to measure concentrations of DJ-1 and two different IgG antibodies are reported. O^2VBRs enable the detection of one of the antibodies investigated here at concentrations as low as 40 ng/mL (250 pM), with a dynamic range for quantitation extending to concentrations an order of magnitude higher. Sensor-to-sensor reproducibility is not degraded by over-oxidation, and coefficients-of-variation (CoVs) remain <20% across the entire calibration curve. A mechanism by which over-oxidation generates larger VBR signals is also proposed.

3.2. Experimental Section

3.2.1. Materials and Methods

All materials used were the same as previously reported. [43] Phosphate buffered saline (PBS, 10x concentrate, Sigma Aldrich). Dilution to 1x PBS yielded a phosphate-buffered saline solution at pH 7.4 with a sodium chloride concentration of 0.154 M and a phosphate buffer concentration of 0.01 M. Data for two IgG antibodies are reported: The monoclonal anti-FLAG M2 antibody produced in mouse was purchased from Sigma Aldrich and the monoclonal anti-M13 P8 antibody produced in mouse was purchased from Creative Diagnostics. The concentrations of the as-received antibody solutions were determined by performing Bradford Assays.

3.2.2. O^2VBR fabrication

The fabrication of O^2VBRs follows the same procedure used for the fabrication of VBRs (Figure B.3),[44] except for the addition of the electrochemical over-oxidation process. In summary, bare gold electrodes were O_2 plasma cleaned for 10 minutes. Well-mixed PEDOT-PSS containing ~1.5% (v/v) ethylene glycol (EG) was spin-coated onto the electrodes at 2500 rpm for 80 s and baked at 90°C for 1 h to achieve films with a DC resistance between 260 to 360 Ω. A polymethylmethacrylate cell to contain the sample was glued to the PEDOT-PSS thin film, and the device was incubated for 30 min in 1x PBS. The PBS was removed, and a solution of 2.5 mM EDOT, 12.5 mM $LiClO_4$, and 8 nM phage was introduced to the cell. Two voltametric scans from +0.2 to +0.8 V (vs a mercurous sulfate reference electrode, MSE) at 20 mV/s electropolymerized the EDOT, simultaneously entrapping the phage particles in the PEDOT polymer.[117,118] The over-oxidation of the VBR channel was accomplished potentiostatically at +0.8 V vs MSE for 100-150 s in aqueous 12.5 mM $LiClO_4$. This process caused an increase in the dc channel resistance, measured in PBS buffer, from an initial range of 1 - 2 kΩ before oxidation, to 12 - 25 kΩ after oxidation.

3.2.3. Impedance Spectroscopy (IS)

VBRs and O^2VBRs were washed twice with room temperature 1x PBS, and equilibrated in PBS for 20 min prior to the acquisition of triplicate IS measurements in 1x PBS. After the baseline was acquired, the sensor was exposed to an antibody or DJ-1 solution in 1x PBS and allowed to equilibrate for 20 min prior to the acquisition of triplicate IS data sets. Importantly, VBRs and O^2VBRs were used for the measurement of a single antibody solution or a single DJ-1

solution. All IS measurements used an applied voltage amplitude of 10 mV. 50 impedance measurements were acquired between 1 Hz and 4 kHz for each data set.

3.2.4. SEM Experiments

Scanning electron microscopy (SEM) images were obtained using a FEI Magellan 400L XHR FE-SEM. An accelerative voltage of 2 keV was used for uncoated films and 15 keV for samples sputter-coated with 3 nm of iridium.

3.2.5. Liquid Tapping AFM Experiments

To obtain the topographical information for VBRs in solution, 50 µL of PBS buffer was pipetted onto the PEDOT-virus layer surface. All AFM images in a liquid environment were collected using a MFP-3D (Asylum Research) in liquid AC (tapping) mode in PBS buffer using DNP-S10 silicon nitride tips (maximum tip radius: 40 nm, Bruker).

3.3. Results and Discussion

3.3.1. O^2VBR Fabrication and Characterization

VBRs and O^2VBRs share the same device architecture consisting of a two-layer polymeric channel that is deposited on top of two gold electrodes spaced by 1.5 mm. The top-most PEDOT polymer layer also contains virus particles that are engineered using the technique of phage display to recognize and bind a particular protein. The gold electrodes measure the electrical impedance of the polymeric channel, which increases when the embedded virus particles bind to their target protein.

A mechanism for signal transduction in the VBR has recently been proposed,[43] . Briefly, this mechanism is similar to that proposed for chemiresistive gas sensors that exploit a conductive carbon/insulating polymer composite chemiresistor.[119–124] In these systems, the chemiresistor is permeated by a vapor phase molecule with affinity to the polymeric component causing swelling of this channel and a decrease in the volume fraction of the conducting carbon phase, leading to a reduction in the conductivity of the composite. It has been proposed [43] that the virus-PEDOT layer of the VBR operates analogously to these chemiresistors with the conductive PEDOT component of the virus-PEDOT layer undergoing a decrease in volume fraction upon affinity driven absorption of target protein molecules by the entrained virus particles and concomitant swelling of the virus-PEDOT layer. [43] The resulting increase in the electrical impedance of the VBR is

correlated with the concentration of the target protein over a concentration range spanning two to four orders of magnitude. [43]

The fabrication of a O^2VBRs begins with the fabrication of a VBR – just the final fabrication process step differentiates these two devices. Briefly, starting with patterned gold electrodes on glass (Figure B.3a), VBRs are prepared in three steps. First, a PEDOT-PSS layer is deposited by spin-coating and dried (Figure B.3a, step 1). Second, a poly(methyl methacrylate) or PMMA solution cell with adhesive backing is pressed onto the PEDOT-PSS layer (Figure B.3a, step 2). Third, this solution cell is used to contain an aqueous plating solution containing both EDOT and virus particles. From this solution, a virus-PEDOT composite layer is electrodeposited by potentiodynamic oxidation of the EDOT monomer (Figure B.3c) for two voltametric scans to a positive limit of +0.80 V vs. MSE causing the formation of insoluble, cationic PEDOT that precipitates on the PEDOT-PSS electrode as a film. Negatively charged virus particles present in the plating solution also deposit with the PEDOT,[71] forming a virus-PEDOT composite top layer (Figure B.3a, step 3). As seen in the photograph of a VBR shown in Figure B.3b, the resulting VBR "channel" is blue in color, and transparent. The blue color is characteristic of the PEDOT-PSS base layer in its oxidized, electronically conductive state.[125,126]

An O^2VBR is obtained by the potentiostatic electrochemical over-oxidation of the VBR channel. This is accomplished by stepping the potential of the channel to +0.80 V in aqueous $LiClO_4$ using external reference and counter electrodes (Figure B.3a, step 4 and Figure B.3d). The over-oxidation process causes a bleaching of the blue VBR channel (Figure B.3b), rendering the channel of the O^2VBR colorless and transparent, consistent with strong de-doping of the PEDOT-PSS layer of the channel. [127] Nyquist plots for a VBR and O^2VBRs (Figure B.3e) show a characteristic semicircular response expected for the VBR. [43] The resistive component of the channel impedance, Z_{re}, is approximately equal to the low frequency limit of these traces, which increases from 2 kW for the VBR (green), to 7.5 kW for the O^2VBR prepared using a 50 s (red) over-oxidation duration, to 16.3 kW for the O^2VBR prepared using a 100 s duration of over-oxidation (purple). This impedance increase is also consistent with a loss of mobile polaron and bipolaron charge carriers from the VBR channel.[127] The O^2VBRs prepared for this study employed an over-

oxidation time of 100-150 s oxidation durations within this range produced identical results within our experimental error.

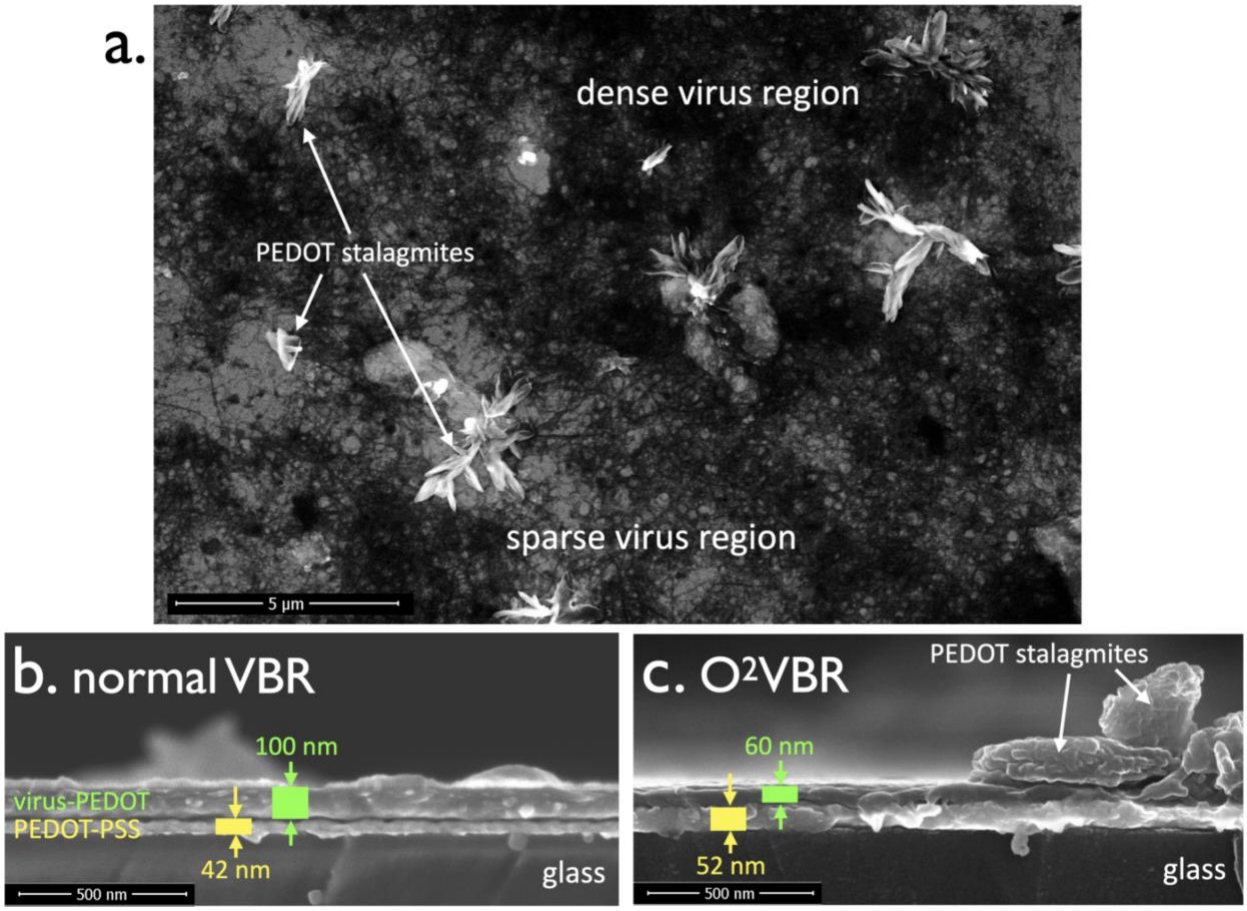

Figure 3.2 - Plan-view SEM image of a O^2VBR channel (a). Darker regions of this image denote regions of high M13 virus density within the virus-PEDOT. Light regions have lower M13 densities. Crystalline PEDOT asperities or "stalagmites" are unrelated to the presence or absence of virus particles. Plan-view images of VBR and O^2VBR are indistinguishable. Cross-sectional view of a VBR (b) and O^2VBR (c) showing thinning of the virus-PEDOT layer from ≈100 nm to ≈60 nm associated with over-oxidation.

The application of chemical and electrochemical over-oxidation to PEDOT for purposes of modifying the electrical conductivity of PEDOT films for applications unrelated to the modification of biosensors has been previously reported.[128–130] Over-oxidation is simply the irreversible oxidation of the PEDOT culminating in a sharp reduction in its conductivity. The mechanism of the overoxidation process is proposed[129] to involve a multi-step oxidation starting with conversion of the thiophene ring sulfur to a sulfonyl (-S=O), and the elimination of -S=O from the polymer backbone as sulfate,

leaving hydroxyl groups in the backbone at both positions adjacent to where the sulfur was formerly located in the thiophene.[129]

Over-oxidation alters the topography and thickness of the virus-PEDOT layer exposed at the surface of the VBR channel. Plan-view SEM images of VBRs and O^2VBRs (shown in Figure 3.2a) are indistinguishable, however. In these images, M13 virus particles and aggregates of particles appear black because they are electrical insulators and PEDOT, a conductor, appears gray. Regions of high M13 density and low M13 density are thus readily identified. Cross-sectional SEM images (Figure 3.2b,c) can be used to directly measure the thickness of the virus-PEDOT and PEDOT-PSS layers of the channel. These images show that the PEDOT-PSS bottom layer is consistently 40 to 55 nm in thickness and unaffected by over-oxidation. The virus-PEDOT top layer, however, is reduced in thickness from ≈100 nm in VBRs to ≈60 nm in O^2VBRs. In principle, this reduction in thickness of the virus-PEDOT top layer should increase its resistance, contributing to the observed increase in the O^2VBR's channel (Figure B.3e).

The topography of the virus-PEDOT top-layer can be inspected using atomic force microscopy (AFM, Figure 3.3). These AFM images show a dramatic reduction in surface roughness for O^2VBRs relative to VBRs. The filamentous texture seen in AFM images of a VBR is caused by M13 virus particles projecting from the virus-PEDOT surface (Figure 3.3 a,c). This texture is not observed for O^2VBR channels (Figure 3.3 b,d), and the surface roughness of the virus-PEDOT layer is reduced, shaving ≈30 nm from the surface. This loss in layer thickness is approximately equal to the thickness reduction of the virus-PEDOT layer seen for O^2VBRs compared with VBRs (Figure 3.2b,c). But it should be noted that, as clearly seen in SEM plan view images (Figure 3.2a), over-oxidation does not remove virus particles from the interior of the virus-PEDOT layer; they are selectively removed from the surface. As will be clear from the data presented below, this apparent loss of virus particles does not impair the sensitivity of the O^2VBR. This surprising result suggests that the carpet of virus particles anchored to the PEDOT layer, but not embedded within it, plays no roll in VBR signal transduction.

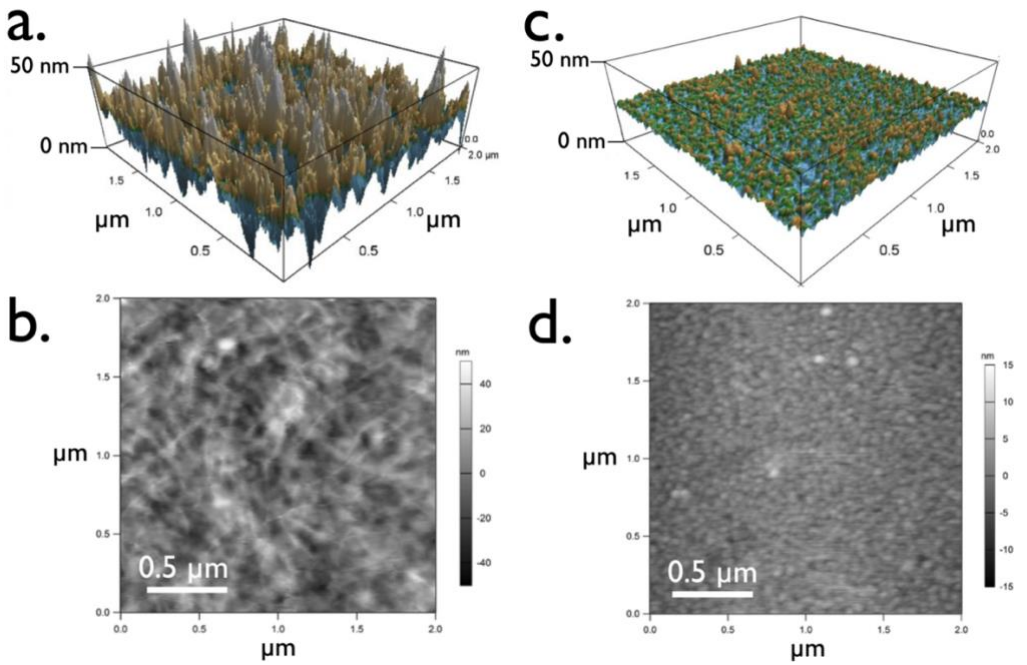

Figure 3.3 - AFM images of VBR (a,b) and O^2VBR (c,d) surfaces.

Two other analytical methods – Raman microprobe spectroscopy (Figure B.4) and X-ray photoelectron spectroscopy (XPS, Figures B.5 and B.6) – have been applied to the characterization of the over-oxidation process. While subtle differences between VBRs and O^2VBR are apparent from these data, the differences do not provide a chemical justification for the enhancement in signal amplitudes for Abs reported here. Instead, the source of these enhanced signal amplitudes appears to derive from the altered *electrical* properties of the O^2VBR's channel.

3.3.2. VBR and O^2VBR Measurements of Antibodies

The response of VBRs and O^2VBR were compared for two IgG antibodies (Abs): anti-M13, an Ab that recognizes and binds the P8 coat protein of the M13 virus, and anti-FLAG, an Ab that binds to FLAG epitopes displayed as *C*-terminal fusions to some of the P8 coat proteins on the M13 virus. Two different M13 virus particles are used as receptors for the detection of these Abs (Figure B.1). The first of these, KO7, is a wild-type M13 virus with no modifications to its P8 coat peptides (Figure B.1a). This virus presents 2700 copies of P8 on its surface that can be recognized by the anti-M13 antibody. The second virus, M13 FLAG, has a FLAG-tag (with the aa sequence DYKDDDDK, where D =

aspartic acid, Y = tyrosine, K = lysine) appended to a subset of the P8 proteins. (Figure B.1b). VBRs containing the FLAG-tag bind to anti-FLAG Abs. In principle, M13 KO7 possesses 2700 binding sites for anti-M13 whereas M13-FLAG has a smaller number of binding sites, typically <10% of the total number of P8 proteins, although the precise number is unknown.

An enzyme-linked immunosorbent assay (ELISA) can assess the affinity of anti-M13 and anti-FLAG for the two viruses (Figure B.2 a,b). Plots of absorbance for the indicator substrate 3,3',5,5'-tetramethylbenzidine (TNB) as a function of Ab concentration, representing the ELISA signal, show the sigmoidal response expected for Ab binding. The signal at half of the saturation value (EC_{50}) provides an estimate of the magnitude of the Ab affinity interaction with its virus. The measured values of EC_{50} of 7.3 ng/mL (anti-M13) and 7.6 ng/mL (anti-FLAG) are typical of affinities expected for binding by commercial Abs (Figure B.2 a,b).

VBRs prepared with either of these two virus receptors, however, do not sense their complimentary antibodies, even at Ab concentrations well above EC_{50}. Nyquist plots for two anti-M13 and two anti-FLAG concentrations show no measurable signal, even for Ab concentrations as high as 328 ng/mL and 556 ng/mL, respectively (Figure B.2 c-f). The insensitivity of VBRs to Abs is especially surprising because the limit-of-detection for DJ-1, a much smaller, 22 kDa protein, is just 0.20 ng/mL or 10 pM. [43]

3.3.3. Remediating VBR Ab Insensitivity Using Over-Oxidation

A remedy for the Ab insensitivity seen for VBRs in Figure B.2 can be devised by considering the equivalent circuit responsible for the VBR response (Figure 3.4d). [43] This equivalent circuit has just five elements: two capacitors that provide coupling between the AC voltage signal applied to the channel and the analyte solution, and three resistors, representing the resistances of the analyte solution (R_{soln}), the top virus-PEDOT composite layer ($R_{PEDOT\text{-}virus}$) and the bottom PEDOT-PSS layer ($R_{PEDOT\text{-}PSS}$). The two capacitors, C, are arranged electrically in series with the electrolyte solution and can be further simplified to a single capacitor, C_{total}, with a value given by $C_{total} = C/2$.

The semicircular Nyquist response produced by VBRs (e.g., Figure B.2 c-f) results from the parallel arrangement of C_{total} and R_{VBR}, the effective low-frequency resistance of the two-layer polymer channel: [43]

$$R_{VBR} \approx \frac{(R_{PEDOT-PSS})(R_{PEDOT-virus})}{R_{PEDOT-PSS}+R_{PEDOT-virus}} \quad [1]$$

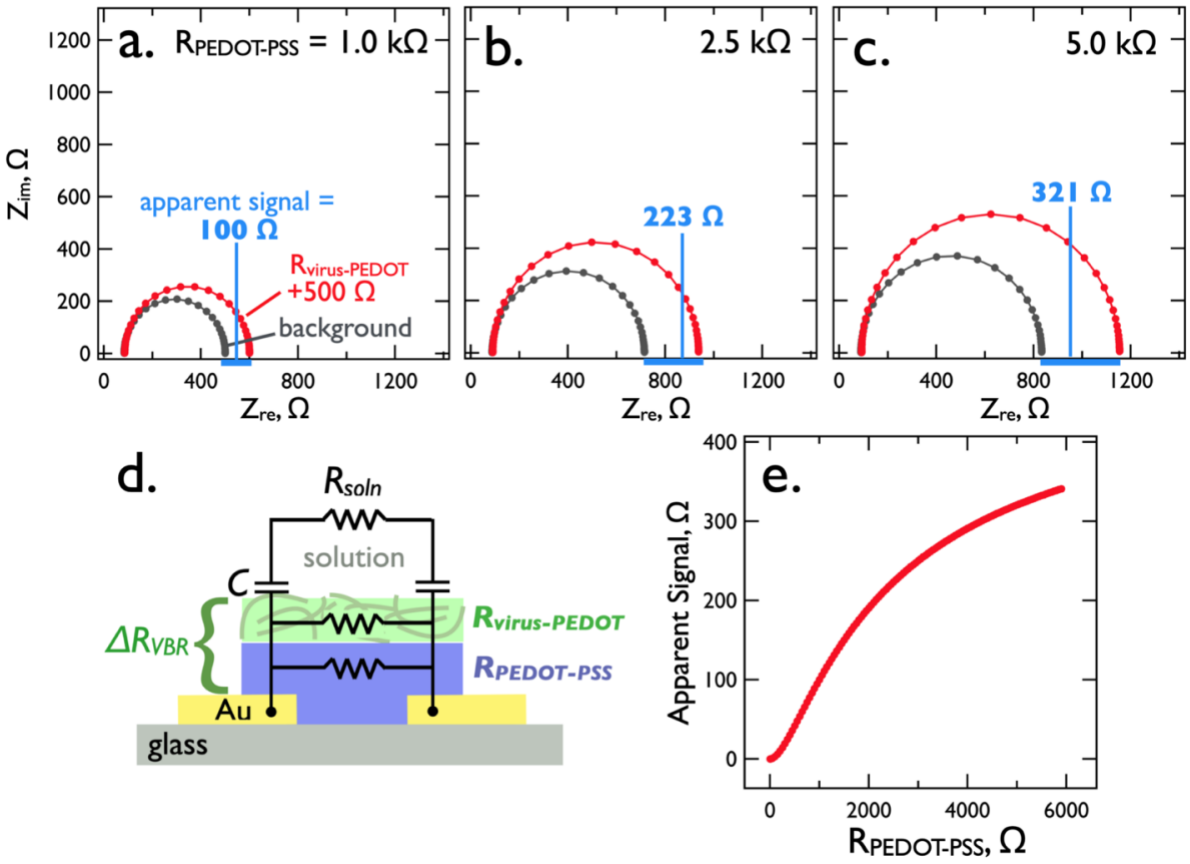

Figure 3.4 - Calculations showing the influence of increased $R_{PEDOT-PSS}$ (as indicated) on the apparent signal, DR_{VBR}. a-c) Calculated Nyquist plots for VBRs as a function of the PEDOT-PSS layer resistance, $R_{PEDOT-PSS}$. In the background traces (black), $R_{virus-PEDOT}$ = 1000 Ω, C_{total} = 10 µF, R_{soln} = 100 Ω. In red traces, 500 Ω of "signal" are added to $R_{virus-PEDOT}$ for a total of 1500 Ω. The values of other circuit elements remain unchanged. d). Schematic diagram illustrating the equivalent circuit of the VBR, e) Plot of the apparent signal (DR_{VBR}, Ω) versus $R_{PEDOT-PSS}$.

At the low frequency limit (f < 1 Hz), the impedance of C_{total} increases to $Z_{im} = (2\pi f C_{total})^{-1}$, exceeding the value of R_{VBR}. In this low f limit, the coupling of the AC signal into the solution is strongly attenuated and virtually all of the signal is distributed across the current divider $R_{PEDOT-PSS}$ and $R_{virus-PEDOT}$ having an effective resistance, R_{VBR}. When $R_{PEDOT-PSS}$

and $R_{virus\text{-}PEDOT}$ are equal in size, Eq. [1] predicts that they contribute equally to R_{VBR}, but just the virus-PEDOT layer generates signal related to the presence of a target protein in the solution. This means that just $R_{virus\text{-}PEDOT}$, not $R_{PEDOT\text{-}PSS}$, is increased by target binding. Unfortunately, $R_{virus\text{-}PEDOT}$ cannot be independently measured because it is connected in parallel with $R_{PEDOT\text{-}PSS}$. Instead, the VBR signal, given by: $\Delta R_{VBR} = R_{VBR\text{-}target} - R_{VBR\text{-}cntrl.}$, representing the difference in R_{VBR} in the presence and absence of target protein, is attenuated by the shunting of some current through the PEDOT-PSS bottom layer. To increase ΔR_{VBR}, $R_{PEDOT\text{-}PSS}$ must be increased relative to $R_{virus\text{-}PEDOT}$. Of course, complete removal of the PEDOT-PSS bottom layer would provide an even more effective solution to this problem, however this layer is required to serve as an electrode for the deposition of the virus-PEDOT composite top layer (Figure B.3c).

Since the response of a VBR can be calculated, the influence of changes in $R_{PEDOT\text{-}PSS}$ for constant values of a 500 Ω test signal, and $R_{virus\text{-}PEDOT}$ = 1000 Ω + 500 Ω signal = 1500 Ω can be assessed (Figure 3.4). When $R_{PEDOT\text{-}PSS}$ = 1000 Ω, the apparent signal, ΔR_{VBR} is just 100 Ω (Figure 3.4a). For $R_{PEDOT\text{-}PSS}$ = 2500 Ω, ΔR_{VBR} increases to 223 Ω (Figure 3.4b) and $R_{PEDOT\text{-}PSS}$ = 5000 Ω produces ΔR_{VBR} = 321 Ω (Figure 3.4c). Note that both the control trace (black) and the target trace (red) are influenced by $R_{PEDOT\text{-}PSS}$. As $R_{PEDOT\text{-}PSS}$ increases further (Figure 3.4e), ΔR_{VBR} asymptotically approaches the true value of the signal, 500 Ω. Our hypothesis is that a disproportionate increase in $R_{PEDOT\text{-}PSS}$ *versus* $R_{virus\text{-}PEDOT}$ is also occurring during the over-oxidation process to produce the O^2VBR. Unfortunately, direct confirmation of this mechanism, involving the measurement of resistance for each of these two layers, is not possible because of the nanometer-scale dimensions of both of these layers.

3.3.4. Testing an O^2VBR for the Detection of DJ-1

What effect does the over-oxidation process have on the detection of DJ-1, a relatively small protein? DJ-1 can be detected at concentrations down to a $LOD_{DJ\text{-}1}$ of 10 pM using a VBR. [43] Nyquist plots for three DJ-1 concentrations (Figure 3.5a,b,c) compare three VBRs and three O^2VBRs. At concentrations of 1.0, 30, and 100 nM, VBRs generate $D R_{VBR}$ signal of 320, 420, and 540 Ω, respectively. For O^2VBRs these signals are increased to 926 Ω, 2.53 kΩ, and 4.10 kΩ - corresponding to factors of 2.9x to 7.6x relative to the VBRs. For [DJ-1] = 100 pM (Nyquist not shown), ΔR_{VBR} increases from 122 Ω

(VBR) to 785 Ω (O^2VBR), an increase by a factor of 6.4x. The increase in sensitivity provided by the O^2VBR for DJ-1, can be seen in the bar graph of Figure 3.5g.

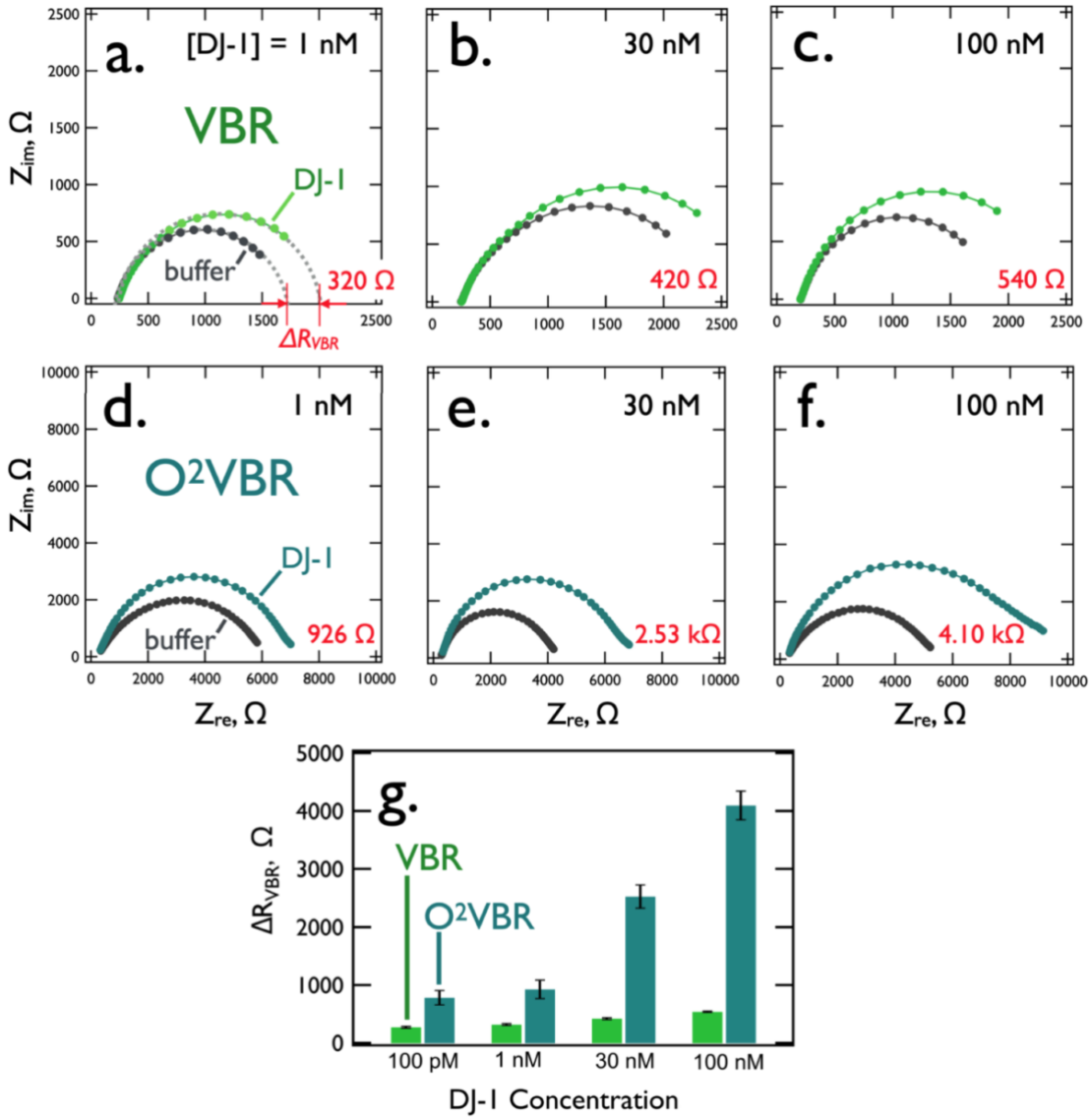

Figure 3.5 - VBR (a-c) and O^2VBR (d-f) Nyquist diagrams showing responses to DJ-1 at the specified concentrations. g). Bar graph of VBR and O^2VBR signal amplitudes as a function of the DJ-1 concentration. A 3- to 4-fold increase in signal amplitude is observed for the O^2VBR across the DJ-1 concentration range from 1 nM to 100 nM.

It should be noted that the Nyquist plots produced by O^2VBRs for DJ-1 exhibit a "tail" at low frequencies, deviating from the precise semi-circular traces seen in Figure 3.8a-c, and previously. These deviations correspond to higher values of Z_{im} and Z_{re} at frequencies, $f < 10$ Hz. These deviations are more pronounced as the concentrations of

DJ-1 increase and are nearly absent for control curves acquired in the absence of DJ-1 (Figure 3.5d-e). This tail is a feature of O²VBRs generally. For the purposes of applying the equivalent circuit of Figure 3.4d and measuring DR_{VBR}, the impedance data set was truncated at 8 Hz prior to curve fitting. This procedure was used to estimate the DR_{VBR} signal amplitudes quoted above, and also for Ab data discussed below. The mechanistic origin of this deviation is interesting and remains under investigation.

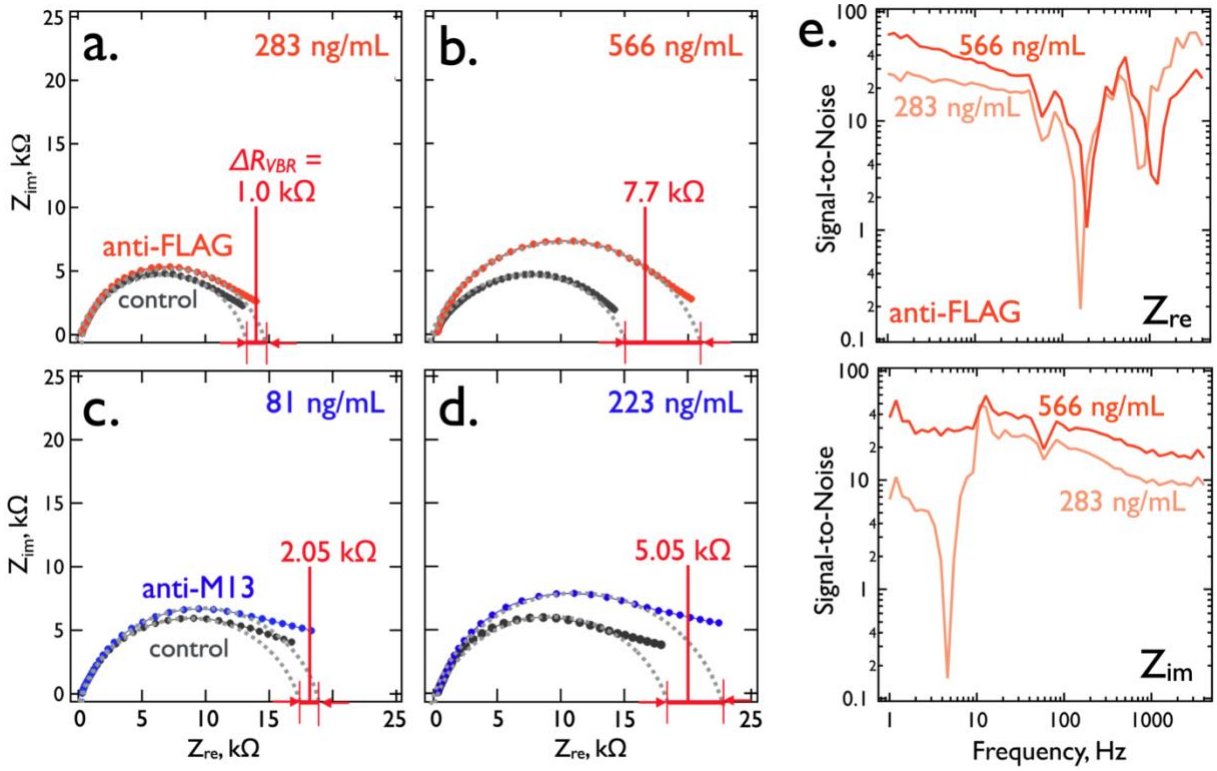

Figure 3.6 - Nyquist diagrams showing responses of four O²VBRs to two antibodies at the specified concentrations. (a-d) Impedance data sets were truncated at 5 Hz. e). Signal-to-noise (S/N) ratios for the real (Z_{re}) and imaginary (Z_{im}) components of the impedance calculated for the detection of anti-FLAG at the two concentrations. On average, somewhat higher S/N ratios are obtained at low frequency.

3.3.5. Detecting Antibodies using O²VBRs

As already noted in Figure B.2, in contrast to DJ-1, Abs are not detected by VBRs. For this reason, the Nyquist plots of Figure B.2a-d showing raw impedance data for the detection of two antibodies using four O²VBRs, are striking. DR_{VBR} signal amplitudes for these two Abs range from 1 - 8 kΩ range in these examples. The lowest Ab concentration of 81 ng/mL corresponds to 0.54 nM.

The signal-to-noise of the O^{2}VBR measurement (Figure 3.6e,f) is optimized in the Z_{re} channel at low frequency ranging from 25 – 60 (Figure 3.6e, top). At high frequency, the ordering of concentrations is actually inverted (Figure 3.6e, bottom). The signal-to-noise of Z_{im} is somewhat lower than Z_{re}, ranging from 7 to 40 for anti-FLAG at 283 and 566 ng/mL.

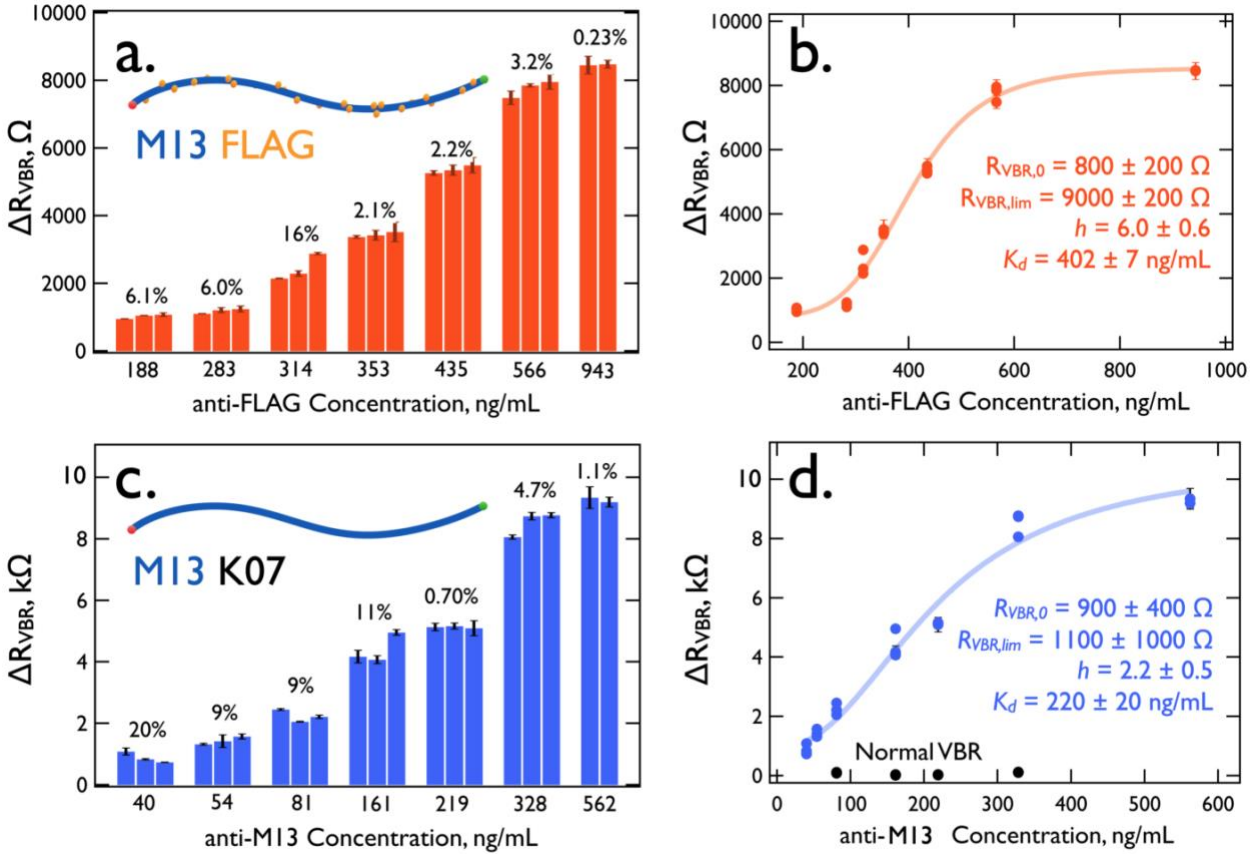

Figure 3.7 - Calibration plots for the detection by O^{2}VBRs of anti-FLAG (a,b) and anti-M13 (c,d). Each bar shown in (a) and (c) correspond to a measurement by a single O^{2}VBR. The coefficient-of-variation is shown for each concentration. Maximum signal amplitudes for these two antibodies of ≈ 8 kΩ are similar.

Bar graphs, showing the signal produced by each O^{2}VBR and the sensor-to-sensor reproducibility (Figure 3.7a,c) reveal that low coefficient-of-variation values in the range from 0.2% (highest Ab concentrations) to 20% (lowest concentrations) are obtained. This level of sensor-to-sensor reproducibility is unusual and testifies to the reproducibility of the over-oxidation process.

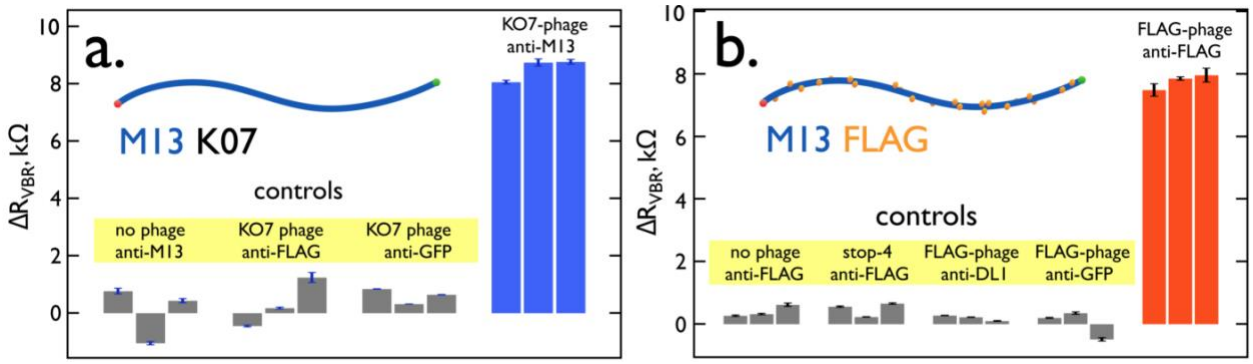

Figure 3.8 - Control experiments for the detection by O^{2}VBRs of anti-M13 and anti-FLAG. All experiments were performed using 100 nM of target (anti-DL-1, anti-GFP, anti-FLAG, and anti-M13) in PBS buffer.

Calibration curves for both Abs show classical sigmoidal behavior that conforms to the Hill Equation (Figure 3.7b,d):[131]

$$\Delta R_{VBR} = \Delta R_{VBR,0} + \frac{\Delta R_{VBR,lim} - \Delta R_{VBR,0}}{1 + \left(\frac{K_D}{[\mathrm{DJ}-1]}\right)^h} \qquad [2]$$

Fitting the calibration data using Eq [2], with fitting parameters *h* and K_D provides values of *h* of 2.2 ± 0.5 (anti-M13) and 6.0 ± 0.6 (anti-FLAG). Values of *h* greater than 1.0 are indicative of strong positive cooperativity, meaning that the microscopic dissociation constant, K_D, is decreased (the affinity interaction is increased) as the fraction of binding sites occupied by the target protein increases.[87] This has the effect of compressing the binding curve resulting in a narrow range of Ab concentrations over which the O^{2}VBR is responsive. This resulting dynamic range is 200 to 600 ng/mL for anti-FLAG (*h* = 6.0) and 50 to 500 ng/mL for anti-M13 (*h* = 2.2). K_D values of 220 (± 20) ng/mL (anti-M13) and 402 (± 7) ng/mL (anti-FLAG) are observed for these two Abs.

Finally, the issue of selectivity of the O^{2}VBR response is addressed by the control experiments summarized in Figure 3.8. Shown in these controls are no phage controls, in which no phage is present in the electrodeposited PEDOT top layer. Two other antibodies, anti-DL-1 (DL-1 is a phage displaying peptide epitopes for DJ-1) and anti-GFP (green fluorescent protein) were also assessed. And O^{2}VBRs containing M13 phage

were assess as controls for the detection of anti-FLAG (Figure 3.8). The level of selectivity seen here is similar to that reported for VBRs in our prior studies.

3.4. Summary

The sensitivity of Virus BioResistors (VBRs) is dramatically enhanced by applying a simple electrochemical process in which the conductivity of the polymeric channel is reduced by a potentiostatic over-oxidation process requiring just 3 to 5 min. The resulting biosensors are termed O^2VBRs. For a smaller protein, DJ-1 (22 kDa) at 100 nM, the signal amplitude generated by O^2VBRs increases by a factor of 4 to 7 kΩ, relative to unmodified VBRs. For much larger IgG antibodies (150 kDa) that are undetectable by VBRs at 100 nM, a signal of 8 kΩ is obtained using O^2VBRs at 100 nM.

The data coupled with our calculations implicate a mechanism for the increased sensitivity of O^2VBRs that involves the strong and disproportionate increase in resistance of the PEDOT-PSS base layer of the channel relative to the virus-PEDOT sensing layer. However, this study does not rule out the influence on sensitivity of significant morphological changes caused by the oxidation process that may, for example, increasing the porosity or mean pore diameter of the virus-PEDOT layer. Pronounced changes to the topography of the virus-PEDOT layer caused by over-oxidation are observed in SEM and AFM images, but we are not able to determine their influence, if any, on the ability of large proteins to permeate the virus-PEDOT layer.

Chapter 4: First Steps Towards the Nano-VBR: A Nanojunction pH Sensor within a Nanowire

This chapter is adapted from a research article “A Nanojunction pH Sensor within a Nanowire”.

4.1. Introduction

The measurement of pH is fundamental to understanding and controlling a diverse range of chemical and biological phenomena occurring in aqueous solutions. The glass membrane pH electrode, dating to the early 1900's[132] permits the pH of a solution to be correlated with a trans-membrane DC potential that is measurable in seconds under optimal conditions. Miniaturization of the glass pH electrode to the 60-80 µm scale for measurements of single cells was demonstrated in 1964 using glass micropipettes.[133] These micropipette pH sensors are macroscopic in length, but microscopic in diameter with modern versions in the 1-5 µm diameter range.[134] Nanometer-scale pH probes capable of still higher spatial resolution require other architectures and transduction mechanisms.

Lieber and coworkers[135] fabricated the first single nanowire-based pH sensor in 2001. These authors employed electron-beam lithography to fabricate a 10 – 20 nm x 2 – 4 µm silicon nanowire field effect transistor (SiNW FET), that was functionalized with 3-aminopropyltriethoxysilane (APTES). This sensor transduced pH using dc conductance. This is still the only prior example of a single nanowire-based pH sensor, as far as we are aware.

Several optical pH sensors with nanometer-scale dimensions have been described (Table C.1). Fujisaku *et al.* [136] used chemically-modified diamond nanocrystals containing nitrogen vacancies to optically transduce pH. In their study, the relaxation of electron spins of the nitrogen vacancies was correlated with the local pH environment.[136] Shen *et al.* [137] demonstrated pH sensing using gold nanoclusters modified with L-/D-cysteine by measuring the phosphorescence after the self-assembly of microstructures from the gold nanoclusters.[137]

Electronically conductive polymer nanojunction sensors were pioneered by Nongjian Tao and coworkers.[138–141] Using an array of focused ion beam (FIB)-patterned metal gaps as electrical contacts, electropolymerization was used to form nanojunctions of poly(ethylene-dioxythiophene) (PEDOT), poly(aniline)(PANI), and other conductive polymers, doped with chemically responsive molecules. Vapor sensors for detecting trinitrotoluene (TNT) were demonstrated.[141] Solution phase sensors for detecting

glucose[142], and redox active analytes such as dopamine and hydroquinone [140] were also described.

PANI can also function as a resistance-based pH transducer. In its protonated, emeraldine salt state, PANI has high electrical conductivity (> 10^2 S/cm).[143] Deprotonation of the salt to form the emeraldine base reduces the conductivity to 10^{-8} S/cm – a difference of ten orders of magnitude (Scheme C.1). [143] Kaner and coworkers[144,145] employed PANI nanofibers for chemical sensing. This work demonstrated that nanostructured PANI could produce larger and more rapid resistance responses when exposed to acidic or basic vapors including as ammonia and HCl, compared to PANI films. In these experiments, the sensing element consisted of a mat of PANI nanofibers, rather than single nanofibers.[144,145] Subsequently, Choi and coworkers[146] electropolymerized PANI with the same nanofiber mat morphology in lithographically fabricated 5 μm × 3 mm microgaps for solution phase pH measurements.

To our knowledge no attempt has been made to create a single polymer nanojunction sensor for any analyte. In fact, few examples exist of single polymer nanowire sensors for any analyte in the literature.[147,148] These have been achieved by drop-casting a nanowire slurry between many gold microelectrodes and using AC dielectrophoretic alignment to bridge the electrodes. Extra nanowires, beyond the one required, are then physically removed using a micro-probe.[147,148] Scanned tip electrospinning has also been employed to create a single PANI nanofibers between two gold electrodes[149] but such nanofibers have not been applied to measurements in liquids. A third approach has involved chemical polymerization of aniline within trenches on surfaces formed by electron beam lithography.[150] The dc resistance of single PANI nanowires formed using this process was measured as it was exposed to solutions with different pH values. However, pH values above 4.5 were not accessible because of the excessive magnitude of the resistance in these experiments.

Here, it is demonstrated that PANI nanojunctions embedded within single gold nanowires can be reproducibly fabricated. These single nanojunctions (henceforth, *NJ-pH* sensors) transduce pH and generate an impedance signal that is measurable at the two nanowire contacts, producing a pH sensing “node” that is nanoscopic in all three dimensions. Moreover, impedance allows for electrical signals to be measured far past

the metal-insulator transition of PANI, at its $pK_a \approx 4.0$. *NJ-pH* sensors constitute a rapid-responding (30 s), reversible, reusable, and robust pH measuring system with a wide pH dynamic range of 2.0 - 9.0.

4.2. Experimental Section

4.2.1. Materials

All chemicals were used as purchased without further purification. Nickel pellets (99.995%) and Au pellets, (99.999%) were purchased from the Kurt J. Lesker Company. Clean Earth Cyanide Free Plating Solution 24ct Yellow was purchased from Stuller.com. Aniline, ACS reagent grade (≥99.5%) was purchased from Sigma Aldrich. Sodium phosphate (monobasic, anhydrous, enzyme grade >99%), sodium phosphate dibasic (heptahydrate, 99.4%), and sodium chloride (≥99.0%), nitric acid (certified ACS Plus), concentrated sulfuric acid (certified ACS Plus), Ricca chemical Synthetic Urine Solution, and concentrated hydrochloric acid (certified ACS Plus) were purchased from Fisher Scientific. Lithium perchlorate (>99%) was purchased from Arcos Organics. Microposit S1808 positive photoresist and Microposit MF-319 developer were purchased from Kayaku Advanced Materials. Phosphate-buffered saline (10x concentrate, BioPerformance Certified) was purchased from Sigma Aldrich.

4.2.2. Single Au Nanowire Fabrication

The electrodeposition of single gold nanowires was accomplished using the lithographically patterned nanowire electrodeposition (LPNE) process, as previously described (Figure C.1 steps 1 – 5).[151]

4.2.3. Electromigration

The automated, feedback-controlled electromigration process used to prepare nanogaps in single gold nanowires has been described elsewhere and is shown step 10 (Figure C.1).[152]

4.2.4. Poly(aniline) Electropolymerization

The electropolymerization of PANI onto the gold nanowire containing a nanogap was performed in aqueous 0.1 M PANI, 0.5 M H_2SO_4 using a three-electrode cell in which the fractured nanowire, contacted on both ends, served as the working electrode in conjunction with a mercurous sulfate reference electrode (MSE) and a platinum counter electrode (Figure C.1, step 11). Cyclic voltammetry was used to initiate the

electropolymerize PANI using five consecutive scans from -0.1 V to +0.6 V vs. MSE at 50 mV/s. Continued growth of the PANI layer was then carried out for 10-20 growth cycles by sweeping from -0.1 to +0.45 V vs. MSE at 50 mV/s until the nanogap was filled with PANI, as indicated by a stepwise reduction in the low frequency wire impedance, measure *in-situ*. This two-step process involving decreasing the positive potential limit after the nucleation scans enabled the electropolymerization of a highly uniform PANI layer while avoiding over-oxidation of the polymer.[153] A PalmSens3 potentiostat running v2.8 software was used to perform electropolymerization.

4.2.5. PBS Buffers for pH Sensing

The automated, feedback-controlled electromigration process used to prepare nanogaps in single gold nanowires has been described elsewhere and is shown step 10 (Figure C.1).[152]

4.2.6. Electrochemical Impedance Spectroscopy

EIS was performed using a Palmsens3 potentiostat running v2.8 software, a Princeton Applied Research 2263 potentiostat, or a Biologic potentiostat running EC-lab software. Measurements were acquired using a 10 mV AC amplitude at the rest potential of the nanowire. For temporally resolved pH measurements, a frequency of 5 Hz was used, and the impedance was sampled at two second intervals.

4.2.7. Salt Correction

Solutions with specified pH values and varying NaCl concentrations were prepared with a fixed, total phosphate concentration of 50 mM. This corresponded to the lowest salt concentration investigated in this study. Solutions with higher salt concentrations were obtained by adding NaCl to this phosphate buffer. pH was confirmed using a standard pH electrode measurement.

4.2.8. Scanning Electron Microscopy

Scanning electron microscopy (SEM) images were acquired using a FEI Magellan 400L XHR FE-SEM operating at an accelerating voltage of 10 kV. All samples were coated with 5 nm of iridium.

4.3. Results and Discussion

4.3.1. Fabrication of Nanowire Nanojunction pH Sensors

The fabrication of a *NJ-pH* sensor involves four steps (Figure 4.1). First a gold nanowire is prepared using lithographically patterned nanowire electrodeposition (LPNE, Figure C.1).[151,154] Second, gold contacts are applied (Figure 4.1a) and insulated by a photoresist overlayer (Figure 4.1b). A nanogap is then formed in the gold nanowire using feedback-controlled electromigration (Figure 4.1c). Finally, a nanojunction is formed by filling this nanogap with PANI by electropolymerization (Figure 4.1d). Although PANI coats the entire gold nanowire while forming the nanojunction, control experiments demonstrate that just the polymer within the nanojunction participates in pH transduction because only at the nanojunction is the through-wire impedance modulated by pH (Figures C.2 and C.3).

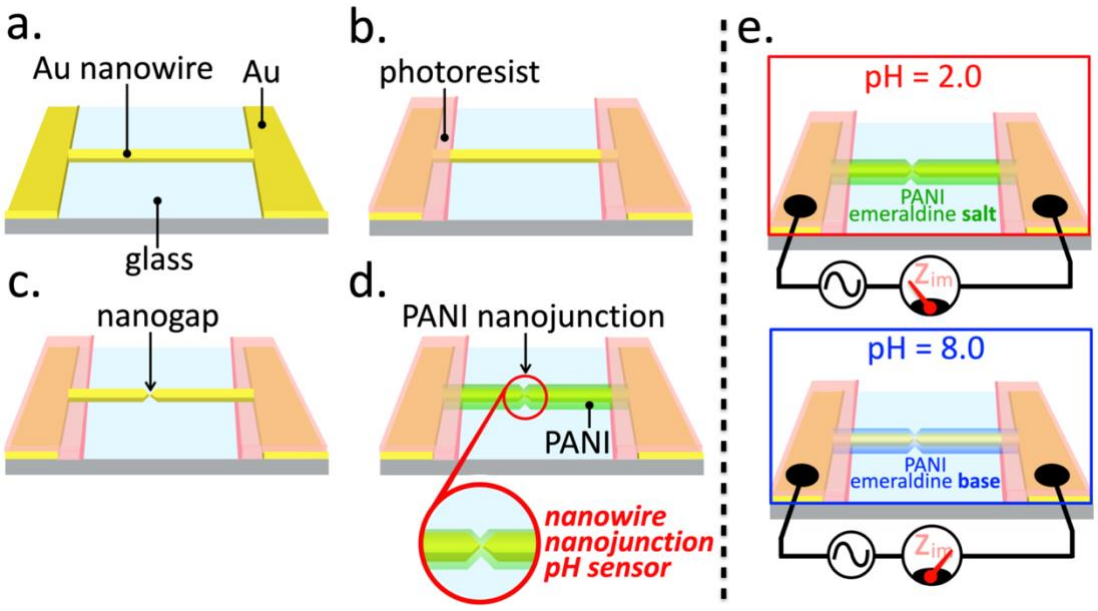

Figure 4.1 - Fabrication of a NJ-pH sensor. a). A gold nanowire (dimensions: 50 µm (l), 100 - 200 nm (w) and 40 nm (h)) is prepared on a glass surface using lithographically patterned nanowire electrodeposition (LPNE). Gold electrical contacts to the nanowire are deposited by evaporation. b). A photoresist layer insulates the gold contacts. c). Feedback-controlled electromigration is used to produce a single nanogap (50 ± 30 nm) within the nanowire, d). Filling the nanogap with PANI using electropolymerization produces a NJ-pH sensor. e). The imaginary component of the electrical impedance, Z_{im} is correlated with pH across the range from 2.0 - 9.0 with a response time of 30 s.

The formation of the nanogap in Step 3 is accomplished using feedback-controlled electromigration (Figure 4.2a)[152,155–161]. This involves increasing the voltage applied to a gold

nanowire, E_{app}, from an initial value of 10 mV at 5 mV/s, while measuring the resistance of the nanowire. A reference resistance, R_{ref}, is measured at the beginning of the experiment, and when the resistance of the nanowire changes by ± 1.5% of R_{ref}, the E_{app} is decreased by 50 mV and a new R_{ref} is measured. 50 mV E_{app} reductions are seen as glitches in the blue (Resistance) and red (E_{app}) traces (Figure 4.2a). The nanowire resistance decreases as the electromigration process proceeds because grain growth occurs in parallel with the formation of constrictions by electromigration and acts in opposition to the increase in resistance caused by these constrictions. A sudden increase in resistance at 600 s in Figure 4.2a signals the formation of a nanogap, terminating the electromigration program.

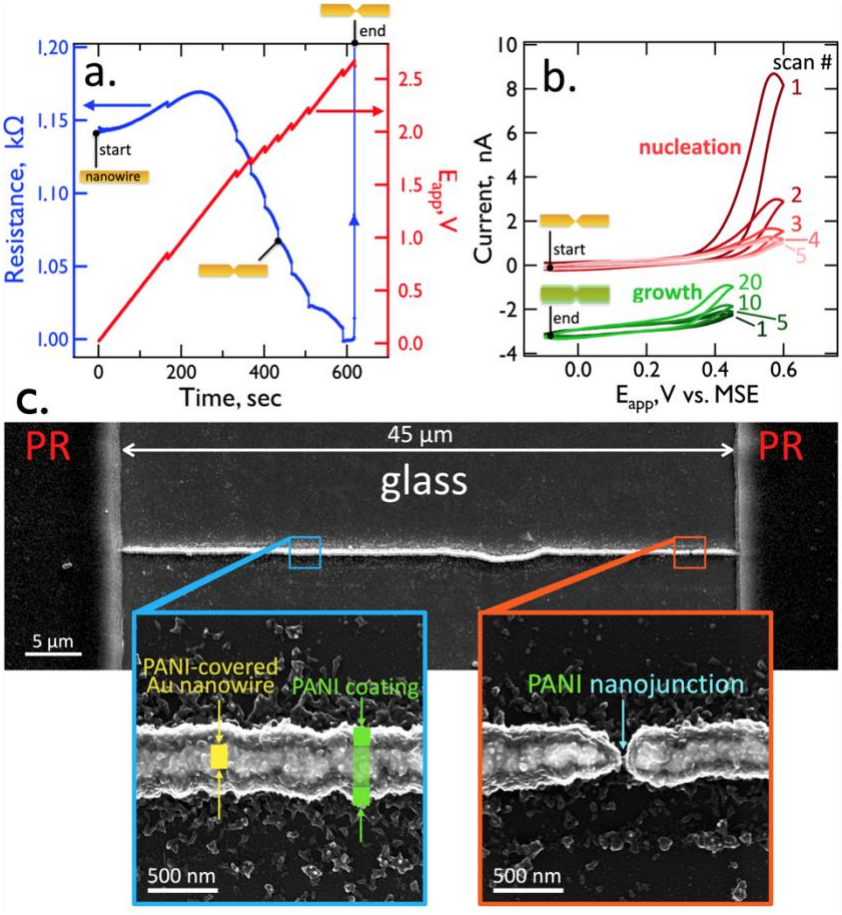

Figure 4.2 - Fabricating a NJ-pH sensor. a). Plot of the resistance of a gold nanowire (blue) and the applied potential (red) as a function of time during feedback-controlled electromigration to form a nanogap. Breaks in both curves indicate points at which the applied voltage was reduced by 50 mV. b). Cyclic voltammograms (50 mV/s) for a bare gold nanowire with a nanogap in an aqueous 0.50 M H_2SO_4 solution containing 0.1 M aniline. Five initial nucleation scans to a +0.60 V vs. MSE positive limit prepare PANI nuclei on gold surfaces. A second series of 10-20 scans to +0.45 V grow a continuous PANI layer. These growth scans are terminated when electrical continuity across the nanojunction is detected. c). SEM images of a PANI-coated Au nanowire

containing a nanogap, showing, at higher magnification (bottom) the PANI-coated gold nanowire and the PANI nanojunction.

The anodic electropolymerization of aniline to form PANI on the nanowire and in the nanogap was accomplished using cyclic voltammetry (Figure 4.2b). From an initial potential of −0.10 V vs. MSE, the potential was initially scanned at a rate of 50 mV/s to +0.60 V on five consecutive cycles to form PANI nuclei on all nanowire surfaces (Figure 4.2b). Then, an additional 20 growth scans to a positive limit of +0.45 V were performed to grow a conformal PANI layer over the entire nanowire, bridging the nanogap (Figure 4.2b). PANI growth was terminated when the through-wire resistance of the nanowire and nanogap was reduced to the kΩ range, indicating PANI had formed a nanojunction by filling the gap and closing the circuit.

This fabrication process does not afford the ability to produce identical sensors with identical performance. While the reproducibility of the LPNE fabrication process for preparing the gold nanowire is excellent, the precision of the wire thickness and width dimensions are still subject to a variability of ≈10% and 20-30%, respectively. The variability of the length of the nanogap formed by electromigration is >50%, leading to different required thicknesses of PANI form the nanojunction and thus slightly different impedimetric properties between samples. Like the familiar glass electrode pH meter, each *NJ-pH* sensor requires calibration prior to use.

Scanning electron microscopy (SEM) images of PANI-coated gold nanowires (Figure 4.2c) demonstrate that the brighter gold nanowire core can be clearly distinguished from the PANI coating. A high degree of uniformity for the PANI coating is apparent from such SEM images. However, it should be appreciated that the dehydration of the PANI during evacuation of the SEM prior to imaging likely causes shrinkage of the PANI layer, and a reduction in its thickness as the polymer is dehydrated. Additionally, PANI nanoparticles can be seen around the nanowire because of the precipitation of the polymer near the nanowire during electro-polymerization. We do not expect these particles are believed to influence the measurement since the gold nanowire is much more conductive than PANI, thus only the PANI in the region where the gold nanowire is discontinuous will modulate the impedance.

4.3.2. Signal Transduction

Measurement of the electrical impedance has not been exploited to transduce nanowire sensors for any purpose, to our knowledge. In this application, impedance-based transduction enables higher signal-to-noise and confers the ability to correct the measured pH for the influence of salt in the test solution, as described below. To understand the impedance response of the *NJ-pH* sensor, it is instructive to compare the three device architectures shown in Figure 4.3: A solid gold nanowire (Figure 4.3a), a gold nanowire containing a nanogap (Figure 4.3b), and the nanowire nanojunction corresponding to a gold nanowire containing a nanogap coated with PANI (Figure 4.3c). Shown in Figure 4.3 are experimental Nyquist plots of the impedance response for each circuit (red data), and the best fit corresponding to the equivalent circuit shown in Figure 4.3d,e and f respectively (blue data). The equivalent circuits for these three devices (Figure 4.3d-f) are constructed using just four circuit elements: The solution resistance (R_{soln}), the through-wire resistance of the gold nanowire (R_{wire}), a capacitor that accounts for the double-layer capacitance of the nanowire-solution interface ($C_{dl\text{-}wire}$), and in the case of the *NJ-pH* only, a resistor representing the PANI nanojunction (R_{PANI}).

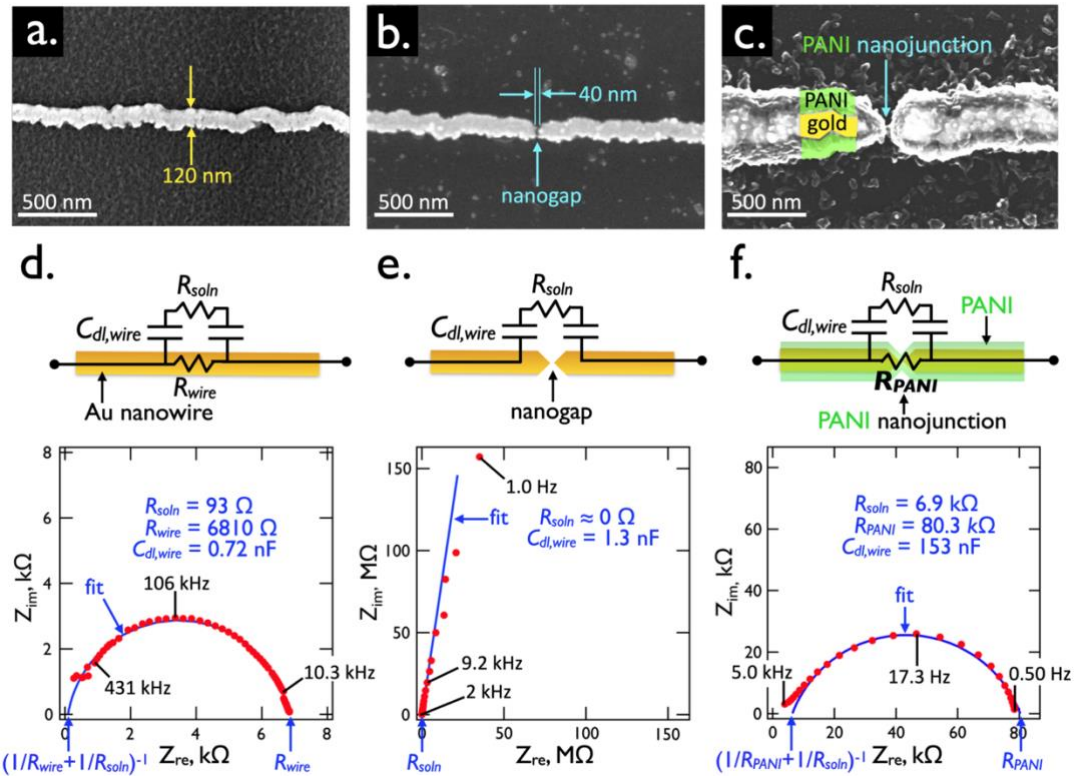

Figure 4.3 - Impedance signatures for three types of nanowires. a-c). SEM images of three types nanowires, as follows: a) a solid gold nanowire with dimensions 120 nm (w) and 40 nm (h), b) a solid gold nanowire containing a nanogap, and (c) a solid gold nanowire containing a PANI nanojunction. d-f). The equivalent circuit corresponding to each of these three nanowires (top), together with their characteristic Nyquist plots acquired in aqueous pH = 3.0 (Z_{im} versus Z_{re} as a function of frequency, as indicated, at bottom). In (d) and (f), semicircular Nyquist plots are produced by parallel resistors and capacitors, but impedance values are shifted by a factor of ten in these two data sets. In (e), the nanogap eliminates the through-wire resistor, and transforms the Nyquist plot into a near-vertical trace, approximating a series RC circuit. All Nyquist plots were acquired in aqueous pH = 3.0, phosphate buffer.

Nyquist plots (Z_{im} *versus* Z_{re}) as a function of frequency, *f*, show two limiting behaviors for these three devices: A semicircular plot, when C and R elements are electrically connected in parallel (Figure 4.3d,f), and a near-vertical plot, for a series RC circuit (Figure 4.3e). The values of the three circuit elements can be extracted by simulation, and these are indicated in each of the three Nyquist plots. For a gold nanowire with dimensions seen in Figure 4.3a the measured R_{wire} = 6.8 kΩ. This R_{wire} value coincides with the intercept of the semicircle with the Z_{re} axis at low frequency, as indicated (Figure 4.3d). The value of $Z_{im} = (2\pi fC)^{-1}$ is small relative to this 6.8 kΩ observed for this circuit indicating that because the high impedance of the capacitors at low frequencies "disconnects" R_{soln} from the circuit. At a high frequency of ≈300 kHz,

the capacitors have negligible impedance, and a second intercept with the Z_{re} axis is observed (Figure 4.3d), corresponding to the parallel combination of R_{soln} and R_{wire}: $R_{parallel} = (R_{wire}^{-1} + R_{soln}^{-1})^{-1}$. Altering the salt concentration and extracting R_{soln} and R_{wire} from impedance data (Figure C.4) validates the equivalent circuit, showing R_{soln} decreases with increased salt concentration, while R_{wire} remains unchanged.

Eliminating the R_{wire} resistor by forming a nanogap produces the characteristic vertical trace of a series RC circuit (Figure 4.3e). The intercept of this line with the Z_{re} axis corresponds to R_{soln}. We use a constant phase element (Qc) [86] in place of a capacitor to account for the slope of this trace likely due to the nanoscale heterogeneity in the surface of the nanowire, which results in non-uniform capacitance[162]:

$$Z_Q = \frac{1}{Q_0(j2\pi f)^n} \quad (1)$$

Where n is the constant phase ($-90^o \times n$), with $0 < n < 1$. The value of n in the Nyquist plot of Figure 4.3e is 0.91. Q_0 is the capacitance corresponding to $n = 1.0$. [86] This equivalent circuit was validated (Figure C.5) by tracking impedance changes R_{soln} and $Q_{dl,wire}$ with salt concentration.

A semicircular Nyquist plot is recovered again when the nanowire with a nanogap is coated with conductive PANI forming a PANI nanojunction and restoring R_{wire} (now called R_{PANI}). The Nyquist plot for the nanojunction pH sensor shown in Figure 4.3f was acquired in pH = 3.0 buffer. At this pH, the PANI layer is highly conductive, and the plot resembles that of the solid gold nanowire (Figure 4.3d) except that R_{soln} (6.9 kΩ) and R_{PANI} (80.3 kΩ) are higher, where R_{PANI} should be compared to R_{wire}. This is a clear indication that, relative to a solid gold nanowire, the low-frequency impedance of the PANI nanojunction is an order of magnitude higher and dominates the through-wire impedance measured at low frequency. Thus, changes in R_{PANI} can be assumed to be responsive to the local pH at the PANI nanojunction. Finally, the measured C increases by roughly two orders of magnitude, likely because of the pseudo-capacitance of the PANI, an electroactive polymer. This equivalent circuit highlights the benefit of using impedance as opposed to measuring a DC resistance, as the resistance of the nanojunction at low frequency is decoupled from the resistance of the solution at high

frequency. The difference in the measured R_{soln} values between the three types of nanowires and circuits is likely due to the imperfect surface capacitance at each step in the process. The semicircular Nyquist plot in Figure 4.3f representing the PANI NJ is much more depressed and non-ideal at high frequency compared to the solid gold nanowire Nyquist plot in Figure 3d. This ultimately diminishes the ability to extract an accurate R_{soln} from the best fit equivalent circuit. However, as will be discussed in a future section, only the impedance at one high frequency is needed to predict R_{soln} and thus the salt concentration.

4.3.3. Randomized pH Sensing: Properties and Performance of the *NJ-pH* Sensor

Nyquist plots for pH values from 1.0 – 9.0 (Figure 4.4a,b) show that at low pH values (< 4.0), semicircular Nyquist plots resembling that presented in Figure 4.3f are observed because the PANI ($pK_a \approx 4$) within the nanojunction is conductive in its protonated state. However, the diameter of the semicircle increases sharply as pH increases over this range, from 100 kΩ (pH = 1.0) to 1.3 MΩ (pH = 4.0) (Figure 4.4b). This indicates an increase in resistance of R_{PANI} in Figure 4.4f, as expected. At still higher pH values ≥5.0, the semicircle disappears, signaling the loss of through-nanojunction conduction. In this pH range, Nyquist plots resemble that of the “open” nanogap as seen in Figure 4.3e. Low frequency impedance values gradually increase over this pH range (Figure 4.4a) as protonated PANI is neutralized. Circuit values have been extracted from these Nyquist plots (Figure C.6, Table C.2).

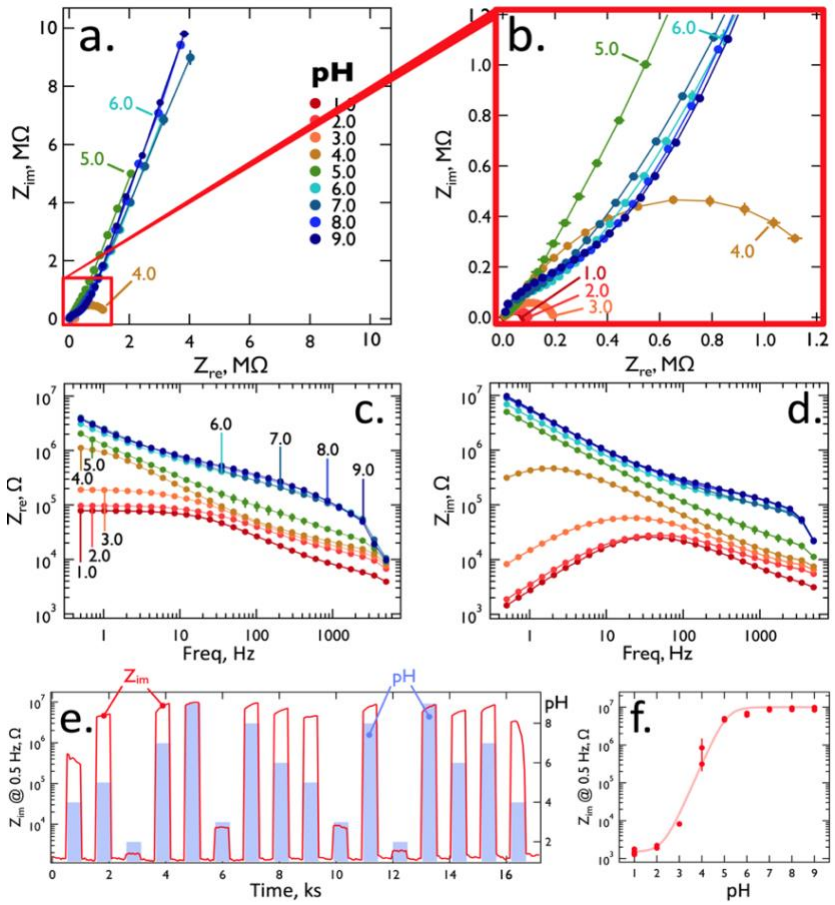

Figure 4.4 - Randomized pH sensing with a NJ-pH sensor. a,b). Nyquist plots for pH values of 1.0 – 9.0. At pH ≤ 4.0, a semi-circular trace is observed, consistent with the circuit shown in Figure 4.3f. At pH ≥ 5.0, a near-vertical Nyquist plot is observed, as seen for Figure 4.3e, because the PANI has very low electronic conductivity in this pH range. c,d). Plots of log [Z_{re}] and log [Z_{im}] versus frequency. e). Plot of log [Z_{im}] at 0.5 Hz versus time for 16 exposures of the sensor to solutions having pH values ranging from 2.0 – 9.0. Between exposures, the sensor was equilibrated with pH = 1.0 PBS. f). Log [Z_{im}] at 0.5 Hz versus pH calibration plot composed of replicate, non-adjacent, exposures to each pH. Impedance data was not fit to an equivalent circuit due to the large impedance of the deprotonated poly(aniline).

The dynamic range of the pH response for the *NJ-pH* sensor can been seen in Bode plots of log Z_{im} and log Z_{re} *versus* Log *f* (Figure 4.4c,d). These plots show that the sensitivity of the *NJ-pH* sensor is greatest at low frequency and is much larger for the Z_{im} channel than the Z_{re} channel. At f = 0.8 Hz, Z_{im} increases by four orders of magnitude as pH increases from 2.0 – 9.0 (Figure 4.4d). Z_{re}, by contrast, increases by just 50× across this same pH range. Equations for the imaginary ($Z_{im,NJ}$) and real ($Z_{re,NJ}$) components of the *NJ-pH* sensor impedance, equations (2) and (3) respectively, predict that $Z_{im,NJ}$ is more weakly affected than $Z_{re,NJ}$, by R_{soln} relative to R_{PANI}.

$$Z_{im,NJ} = \frac{-{R_{PANI}}^2 C_{dl} 2\pi f}{1+{C_{dl}}^2 2\pi f^2 (R_{soln}+R_{PANI})^2} \quad (2)$$

$$Z_{re,NJ} = \frac{R_{PANI}+ {C_{dl}}^2 R_{PANI}\, R_{soln}(R_{soln}+R_{PANI})2\pi f^2}{1+{C_{dl}}^2 2\pi f^2 (R_{soln}+R_{PANI})^2} \quad (3)$$

Real-time, randomized exposures of the *NJ-pH* sensor to solutions ranging from pH = 2.0 - 9.0 (Figure 4.4e) show that the PANI nanojunction equilibrates rapidly and completely producing nearly flat peak plateaus approximating ideal sensor response characteristics. In this experiment, the *NJ-pH* sensor was immersed in a pH = 1.0 solution between each exposure to buffers at higher pH (purple bars). So called "memory effects", in which the amplitude of a sensor response is dependent upon the pH value of the previous exposure, are minimal. Two exposures to the same pH, separated by several exposures to different solutions, produced nearly identical Z_{im} responses.

The measured value of Z_{im} at low frequency is strongly correlated with pH (Figure 4.4f) creating a sigmoidal response function of log Z_{im} *versus* pH. While this plot suggests a loss of pH sensitivity at high pH values, >5.0, in fact, Z_{im} increases substantially, by 4.8 MΩ, in the pH range from 5.0 – 9.0 enabling measurement of the pH in this range with good signal-to-noise. The pH = 1.0 baseline is stable across 17 separate exposures throughout nearly 5 hours.

The plot of log Z_{im} *versus* time (Figure 4.5a) shows the equilibration of a *NJ-pH* sensor upon exposure to buffers ranging from pH 2.0 – 9.0. More rapid equilibration is observed at high pH, ≥ 6.0 with response times of < 10 s. Equilibration is slower (30-60 s) for solutions of intermediate pH from 3.0 to 5.0. A plot of the pH measured by a PANI nanojunction *versus* the actual pH measured by a macroscopic glass-membrane pH electrode(Figure 4.5b) shows the influence of this equilibration behavior on the accuracy of the pH measurements acquired at four settling times (10, 30, 45, and 120 s). The pH measured by the *NJ-pH* sensor was determined through use of the best fit function from the saturated signal. The degree of correlation between measured pH and actual pH, measured using the Pearson correlation coefficient, r, increases with settling time (where r = 1.000 indicates a perfect correlation). At 120 s, r = 0.988 indicating excellent correlation, but a high r = 0.981 is obtained at a settling time of 30 s.

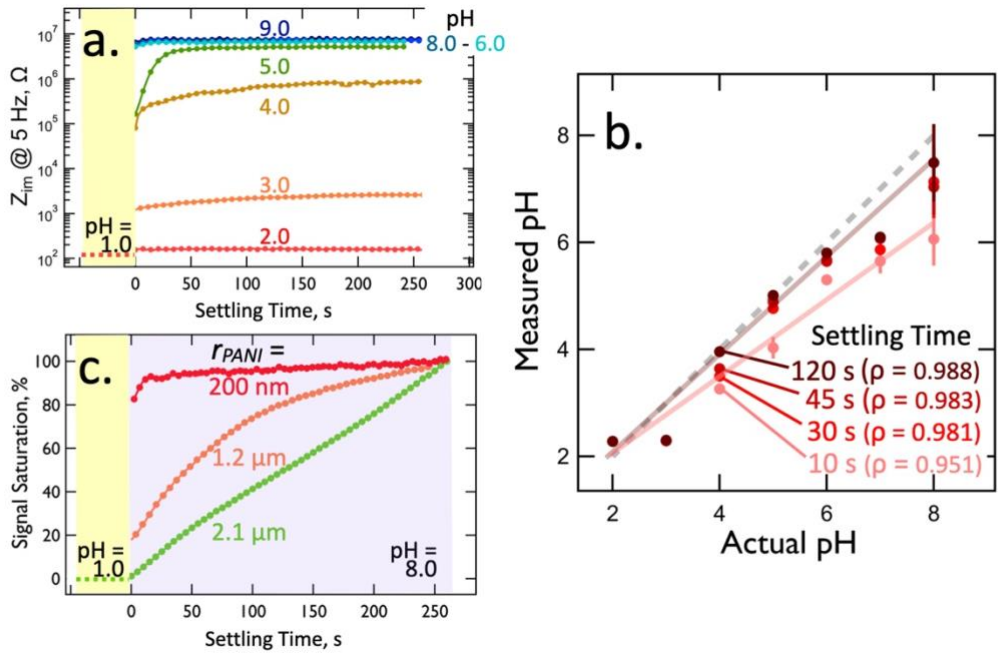

Figure 4.5 - Temporal properties of pH detection. a). Log [Z_{im}] at 5 Hz versus pH calibration curves acquired at three time points after exposure of the PANI nanojunction sensor equilibrated in solutions ranging from pH = 1.0 to pH = 8.0. b). Measured pH versus actual pH for four settling times, as indicated. Covariance of the measured pH from the actual pH was assessed by the Pearson correlation coefficient, ρ. c). % Signal saturation versus time for three NJ-pH of varying wire radii, encompassing the gold nanowire and the PANI coating. Equilibration of the impedance for the smallest, r_{PANI} ≈200 nm, occurs within 10 s.

In view of the nanoscopic dimensions of this pH sensor, is a ≈30s response time reasonable? One response rate-limiting process could be the diffusion of H_3O^+ and OH^- in the PANI, which is required for equilibration of solution-phase concentrations with the polymer. The Einstein equation[163], $t = x^2/2D$, provides the means for estimating the time, t, required for the diffusion of a species with a diffusion coefficient, D, to diffuse a distance, x. The diffusion coefficient of small ions in electrodeposited PANI is in the range from 10^{-12} to 10^{-13} cm^2/s.[164] If a diffusion distance of x = 50 nm is assumed, the Einstein equation yields values of t in the range: 12.5 s < t < 125 s. The observed time response of the *NJ-pH* sensor is in the middle of this range. Thus, the slow diffusion of H_3O^+ and OH^- in the PANI could reasonably account for the measured time response of these sensors, which becomes dramatically slower as the thickness of the PANI coating increases up to 2 µm as shown in Figure 4.5c.

The response times reported here – ranging from 10 s to 2 min for the smallest *NJ-pH* sensors – are similar to, or somewhat faster than, the response times reported for

nanoscopic PANI-based gas sensors for small molecules (30 s - 9 min) including: NH_3[165], NO_2[165], O_3[166], and H_2S[167,168]. The similarity of response times observed for a variety of PANI-based nanoscopic sensor systems and analytes supports the hypothesis that the slow diffusion of analyte species in PANI is rate-limiting in terms of sensor response. Therefore, it is necessary to fabricate a nanoscopic PANI junction to ensure rapid response times.

4.3.4. The Influence of Salt Concentration on the Accuracy of the *NJ-pH* Sensor

At low frequencies, $f < 1$ Hz, the *NJ-pH* capacitors (Figure 4.3f) "pinch off" the coupling of charge from the PANI-coated nanowire into the solution, because the impedance of the interfacial capacitor is proportional to $1/f$:

$$Z_{Cdl,wire} = \frac{1}{(2\pi f C_{dl})} \quad (4)$$

In principle, this minimizes the influence of R_{soln} on the sensor signal. Experimentally, however, we find that the pH calibration of the *NJ-pH* is affected by the salt concentration of the solution. This observation suggests that the ionic environment surrounding PANI in the nanojunction directly modifies R_{PANI} through a Donnan equilibrium.[169] Due to the positive charge of PANI in its protonated state, a Donnan-like potential forms at its interface with the solution, opposing the uptake of protons. The strength of this field depends on the anion concentration in the solution, as the anions compensate this charge and diminish the field strength. Thus, the concentration of salt in the solution will alter the nanojunction's protonation state.

Nyquist plots obtained as a function of the salt concentration at constant pH = 3.9 (Figure 4.6a,b) and pH = 6.9 (Figures 4.6c,d) show considerable variations as the salt concentration increases from 0 (+0.050 M phosphate buffer) to 1.0 M. When these impedance data for the full range of pH values are translated into Z_{im} *versus* pH calibration curves (Figure 4.6f) the influence of salt over this concentration range is seen to be approximately 1 pH unit at pH = 4.0, on the rising portion of the calibration curve, but up to 2 pH units at pH > 5, on the rising plateau of the curve. The accuracy issue posed by the variation of the salt concentration is similar to that encountered with conventional

glass pH electrodes, where liquid junction potentials, sodium ions, and activity effects combine to introduce pH errors of similar magnitudes.[170]

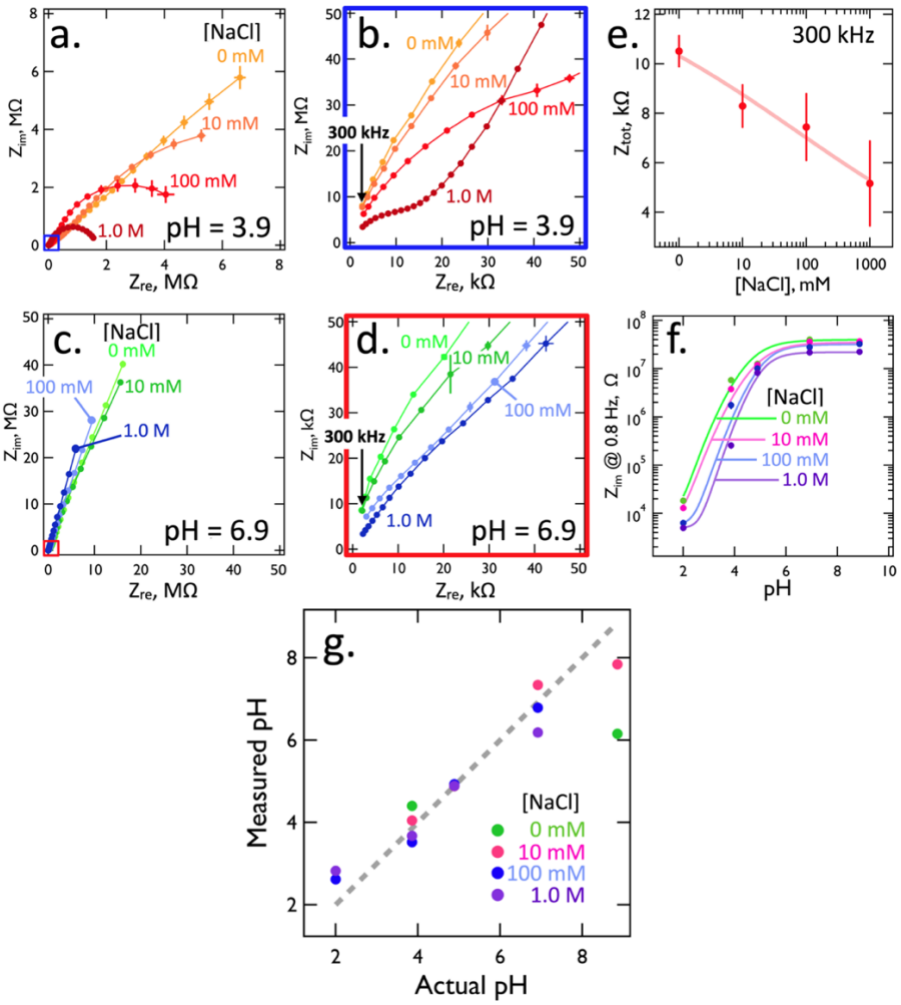

Figure 4.6 - pH measurement correction for NaCl. a,b). Nyquist plots for solutions at pH = 3.9 with NaCl concentrations of 0, 10, 100 mM and 1.0 M (+50 mM phosphate buffer) as indicated. c,d). Nyquist plots for solutions at pH = 6.9 with salt concentrations of 0, 10, 100 mM and 1.0 M as indicated. e). Z_{tot} measured at 300 kHz is logarithmically correlated with the salt concentration. f). Four Z_{im} (measured at 0.8 Hz) versus pH for salt concentrations of 0, 10, 100 mM, and 1.0 M (+50 mM phosphate buffer), added to 50 mM phosphate buffer, as indicated. g) Salt-corrected measured versus actual pH for salt concentrations of 0, 10, 100, and 1.0 M (+50 mM phosphate buffer). Impedance data was not fit to an equivalent circuit due to the large impedance of the deprotonated poly(aniline).

However, impedance read-out of the PANI nanojunction provides a means for correcting the measured pH for the influence of salt. The key is that Z_{tot} at very high frequency, f = 300 kHz, is logarithmically correlated with the salt concentration, irrespective of pH (Figure 4.6e). Therefore, the salt concentration of a test solution can be determined at f = 300 kHz, and an appropriate calibration curve can be selected for

the pH measurement (Figures 4.6f, B.7). This strategy eliminates the deleterious influence of salt on measurement accuracy within the range from 0.05 M to 1.05 M, except at pH values > 8.0 where measured pH value remains somewhat too low (Figure 4.6g). The accuracy of the *NJ-pH* sensors in synthetic urine was also tested and shown in figure S8. For a synthetic urine solution with a measured pH of 6.62 by a glass pH-electrode, the *NJ-pH* sensor measured pH = 6.72 ± 0.04, further confirming that this sensor can accurately predict pH in complex media.

4.4. Conclusions

A pH sensing "node" that is <100 nm in all three dimensions is realized using a sensor architecture in which a gold nanowire controllably fractured and the resulting nanogap is filled with pH-responsive poly(aniline). Using a frequency of ≈1.0 Hz, the electrical impedance measured across the nanogap is used to read-out the pH in the PANI nanojunction. A second, high frequency impedance measurement allows for the determination of the salt concentrations and correction of the measured pH, if necessary. The use of impedance instead of a dc resistance measurement permits signal to be extracted at pH values well removed from the pK_a of PANI, and at high pH values where PANI is has little conductivity. The properties of the PANI nanojunction for measuring pH are similar those of macroscopic glass membrane electrodes: A pH measurement range of 2.0 to 9.0, a reversible response, a response time of 30 s, and reusability. However, the dimensions of the PANI nanojunction are less than 100 nm.

It should be emphasized that the *NJ-pH* sensor is obtained exclusively by high-throughput wet-chemical processing steps, and does not require a clean-room, focused ion-beam milling, electron beam lithography, or other time-intensive and expensive microfabrication processes and facilities. Even the LPNE process required to fabricate single gold nanowires is compliant with the atmosphere of a normal wet chemistry laboratory. A clear path for the generalization of PANI nanojunction pH sensor to the measurement of metal ions, nucleic acids, and proteins is provided by the fact that the required recognition elements (ss-DNA, antibodies, engineered virus particles, chelating agents) have previously been incorporated into the polymer matrix of PANI and other conductive polymers during the electropolymerization process[171–176]. We look forward to testing this hypothesis in our subsequent investigations.

Bibliography

(1) Diaz, A. F.; Logan, J. A. Electroactive Polyaniline Films. *Journal of Electroanalytical Chemistry and Interfacial Electrochemistry* 1980, *111* (1), 111–114. https://doi.org/10.1016/S0022-0728(80)80081-7.

(2) Diaz, A. F.; Castillo, J. I.; Logan, J. A.; Lee, W. Y. Electrochemistry of Conducting Polypyrrole Films. *Journal of Electroanalytical Chemistry* 1981, *129* (1–2), 115–132. https://doi.org/10.1016/S0022-0728(81)80008-3.

(3) Waltman, R. J.; Bargon, J.; Diaz, A. F. Electrochemical Studies of Some Conducting Polythiophene Films. *Journal of Physical Chemistry* 1983, *87* (8), 1459–1463. https://doi.org/10.1021/j100231a035.

(4) Diaz, A. F.; Hall, B. Mechanical Properties of Electrochemically Prepared Polypyrrole Films. *IBM Journal of Research and Development* 1983, *27* (4), 342–347. https://doi.org/10.1147/rd.274.0342.

(5) Diaz, A. F.; Kanazawa, K. K.; Gardini, G. P. Electrochemical Polymerization of Pyrrole. *Journal of the Chemical Society, Chemical Communications* 1979, No. 14, 635–636. https://doi.org/10.1039/C39790000635.

(6) Sato, M.; Tanaka, S.; Kaeriyama, K. Electrochemical Preparation of Conducting Poly(3-Methylthiophene): Comparison with Polythiophene and Poly(3-Ethylthiophene). *Synthetic Metals* 1986, *14* (4), 279–288. https://doi.org/10.1016/0379-6779(86)90041-X.

(7) Heywang, G.; Jonas, F. Poly(Alkylenedioxythiophene)s—New, Very Stable Conducting Polymers. *Advanced Materials* 1992, *4* (2), 116–118. https://doi.org/10.1002/adma.19920040213.

(8) Janata, J. Historical Review: Twenty Years of Ion-Selective Field-Effect Transistors. *Analyst* 1994, *119* (11), 2275–2278. https://doi.org/10.1039/AN9941902275.

(9) Janata, J.; Josowicz, M. Conducting Polymers in Electronic Chemical Sensors. *Nature Materials* 2003, *2* (1), 19–24. https://doi.org/10.1038/nmat768.

(10) Janata, J. Potentiometric Microsensors. *Chemical Reviews* 1990, *90* (5), 691–703. https://doi.org/10.1021/cr00103a001.

(11) Josowicz, Mira.; Janata, J. Suspended Gate Field Effect Transistor Modified with Polypyrrole as Alcohol Sensor. *Analytical Chemistry* 1986, *58* (3), 514–517. https://doi.org/10.1021/ac00294a003.

(12) Miasik, J. J.; Hooper, A.; Tofield, B. C. Conducting Polymer Gas Sensors. *Journal of the Chemical Society, Faraday Transactions 1: Physical Chemistry in Condensed Phases* 1986, *82* (4), 1117. https://doi.org/10.1039/f19868201117.

(13) Umana, Mirtha.; Waller, Jess. Protein-Modified Electrodes. The Glucose Oxidase/Polypyrrole System. *Analytical Chemistry* 1986, *58* (14), 2979–2983. https://doi.org/10.1021/ac00127a018.

(14) Foulds, N. C.; Lowe, C. R. Enzyme Entrapment in Electrically Conducting Polymers. Immobilisation of Glucose Oxidase in Polypyrrole and Its Application in Amperometric Glucose Sensors. *Journal of the Chemical Society, Faraday Transactions 1: Physical Chemistry in Condensed Phases* 1986, *82* (4), 1259–1264. https://doi.org/10.1039/F19868201259.

(15) Walter, E. C.; Murray, B. J.; Favier, F.; Kaltenpoth, G.; Grunze, M.; Penner, R. M. Noble and Coinage Metal Nanowires by Electrochemical Step Edge Decoration. *The Journal of Physical Chemistry B* 2002, *106* (44), 11407–11411. https://doi.org/10.1021/jp026389p.

(16) Zach, M. P.; Ng, K. H.; Penner, R. M. Molybdenum Nanowires by Electrodeposition. *Science (1979)* 2000, *290* (5499), 2120–2123. https://doi.org/10.1126/science.290.5499.2120.

(17) Favier, F.; Walter, E. C.; Zach, M. P.; Benter, T.; Penner, R. M. Hydrogen Sensors and Switches from Electrodeposited Palladium Mesowire Arrays. *Science (1979)* 2001, *293* (5538), 2227–2231. https://doi.org/10.1126/science.1063189.

(18) Walter, E. C.; Favier, F.; Penner, R. M. Palladium Mesowire Arrays for Fast Hydrogen Sensors and Hydrogen-Actuated Switches. *Analytical Chemistry* 2002, *74* (7). https://doi.org/10.1021/ac0110449.

(19) He, H. X.; Li, C. Z.; Tao, N. J. Conductance of Polymer Nanowires Fabricated by a Combined Electrodeposition and Mechanical Break Junction Method. *Applied Physics Letters* 2001. https://doi.org/10.1063/1.1335551.

(20) Yun, M.; Myung, N. V.; Vasquez, R. P.; Lee, C.; Menke, E.; Penner, R. M. Electrochemically Grown Wires for Individually Addressable Sensor Arrays. *Nano Letters* 2004, *4* (3), 419–422. https://doi.org/10.1021/nl035069u.

(21) Ramanathan, K.; Bangar, M. A.; Yun, M.; Chen, W.; Mulchandani, A.; Myung, N. V. Individually Addressable Conducting Polymer Nanowires Array. *Nano Letters* 2004, *4* (7), 1237–1239. https://doi.org/10.1021/nl049477p.

(22) Im, Y.; Lee, C.; Vasquez, R. P.; Bangar, M. A.; Myung, N. V.; Menke, E. J.; Penner, R. M.; Yun, M. Investigation of a Single Pd Nanowire for Use as a Hydrogen Sensor. *Small* 2006, *2* (3), 356–358. https://doi.org/10.1002/smll.200500365.

(23) Babu, S.; Ndungu, P.; Bradley, J. C.; Rossi, M. P.; Gogotsi, Y. Guiding Water into Carbon Nanopipes with the Aid of Bipolar Electrochemistry. *Microfluidics and Nanofluidics* 2005, *1* (3), 284–288. https://doi.org/10.1007/S10404-005-0037-8/FIGURES/4.

(24) Park, S.-J.; Taton, T. A.; Mirkin, C. A. Array-Based Electrical Detection of DNA with Nanoparticle Probes. *Science (1979)* 2002, *295* (5559), 1503–1506. https://doi.org/10.1126/science.1067003.

(25) HACKER, G. W. Silver-Enhanced Colloidal Gold for Light Microscopy. In *Colloidal Gold*; Elsevier, 1989; pp 297–321. https://doi.org/10.1016/B978-0-12-333927-0.50015-5.

(26) Su, X.; O'Shea, S. J.; Li, S. F. Y. Au Nanoparticle- and Silver-Enhancement Reaction-Amplified Microgravimetric Biosensor. *Chemical Communications* 2001, No. 8, 755–756. https://doi.org/10.1039/b009768n.

(27) Menke, E. J.; Thompson, M. A.; Xiang, C.; Yang, L. C.; Penner, R. M. Lithographically Patterned Nanowire Electrodeposition. *Nature Materials* 2006, *5* (11), 914–919. https://doi.org/10.1038/nmat1759.

(28) Xiang, C.; Yang, Y.; Penner, R. M. Cheating the Diffraction Limit: Electrodeposited Nanowires Patterned by Photolithography. *Chemical Communications* 2009, No. 8, 859–873. https://doi.org/10.1039/b815603d.

(29) Yun, M.; Myung, N. V.; Vasquez, R. P.; Lee, C.; Menke, E.; Penner, R. M. Electrochemically Grown Wires for Individually Addressable Sensor Arrays. *Nano Letters* 2004, *4* (3), 419–422. https://doi.org/10.1021/nl035069u.

(30) Ramanathan, K.; Bangar, M. A.; Yun, M.; Chen, W.; Mulchandani, A.; Myung, N. V. Individually Addressable Conducting Polymer Nanowires Array. *Nano Letters* 2004, *4* (7), 1237–1239. https://doi.org/10.1021/nl049477p.

(31) Yang, F.; Taggart, D. K.; Penner, R. M. Fast, Sensitive Hydrogen Gas Detection Using Single Palladium Nanowires That Resist Fracture. *Nano Letters* 2009, *9* (5), 2177–2182. https://doi.org/10.1021/nl9008474.

(32) Soleymani, L.; Fang, Z.; Sargent, E. H.; Kelley, S. O. Programming the Detection Limits of Biosensors through Controlled Nanostructuring. *Nature Nanotechnology* 2009, *4* (12), 844–848. https://doi.org/10.1038/nnano.2009.276.

(33) Soleymani, L.; Fang, Z.; Kelley, S. O.; Sargent, E. H. Integrated Nanostructures for Direct Detection of DNA at Attomolar Concentrations. *Applied Physics Letters* 2009, *95* (14), 143701. https://doi.org/10.1063/1.3226103.

(34) Soleymani, L.; Fang, Z.; Sun, X.; Yang, H.; Taft, B. J.; Sargent, E. H.; Kelley, S. O. Nanostructuring of Patterned Microelectrodes To Enhance the Sensitivity of Electrochemical Nucleic Acids Detection. *Angewandte Chemie International Edition* 2009, *48* (45), 8457–8460. https://doi.org/10.1002/anie.200902439.

(35) Sage, A. T.; Besant, J. D.; Lam, B.; Sargent, E. H.; Kelley, S. O. Ultrasensitive Electrochemical Biomolecular Detection Using Nanostructured Microelectrodes. *Accounts of Chemical Research* 2014, *47* (8), 2417–2425. https://doi.org/10.1021/ar500130m.

(36) Kelley, S. O.; Mirkin, C. A.; Walt, D. R.; Ismagilov, R. F.; Toner, M.; Sargent, E. H. Advancing the Speed, Sensitivity and Accuracy of Biomolecular Detection Using Multi-Length-Scale Engineering. *Nature Nanotechnology* 2014, *9* (12), 969–980. https://doi.org/10.1038/nnano.2014.261.

(37) Soleymani, L.; Fang, Z.; Sargent, E. H.; Kelley, S. O. Programming the Detection Limits of Biosensors through Controlled Nanostructuring. *Nature Nanotechnology* 2009, *4* (12), 844–848. https://doi.org/10.1038/nnano.2009.276.

(38) Yang, L. M. C.; Tam, P. Y.; Murray, B. J.; McIntire, T. M.; Overstreet, C. M.; Weiss, G. A.; Penner, R. M. Virus Electrodes for Universal Biodetection. *Analytical Chemistry* 2006, *78* (10), 3265–3270. https://doi.org/10.1021/ac052287u.

(39) Smith, G. P.; Petrenko, V. A. Phage Display. *Chemical Reviews* 1997, *97* (2), 391–410. https://doi.org/10.1021/cr960065d.

(40) Smith, G. P. Phage Display: Simple Evolution in a Petri Dish (Nobel Lecture). *Angewandte Chemie International Edition* 2019, *58* (41), 14428–14437. https://doi.org/10.1002/anie.201908308.

(41) Winter, G.; Milstein, C. Man-Made Antibodies. *Nature*. January 1991, pp 293–299. https://doi.org/10.1038/349293a0.

(42) Marks, J. D.; Hoogenboom, H. R.; Bonnert, T. P.; McCafferty, J.; Griffiths, A. D.; Winter, G. By-Passing Immunization: Human Antibodies from V-Gene Libraries Displayed on Phage. *Journal of Molecular Biology* 1991, *222* (3), 581–597. https://doi.org/10.1016/0022-2836(91)90498-U.

(43) Bhasin, A.; Sanders, E. C.; Ziegler, J. M.; Briggs, J. S.; Drago, N. P.; Attar, A. M.; Santos, A. M.; True, M. Y.; Ogata, A. F.; Yoon, D. V; Majumdar, S.; Wheat, A. J.; Patterson, S. V.; Weiss, G. A.; Penner, R. M. Virus Bioresistor (VBR) for Detection of Bladder Cancer Marker DJ-1 in Urine at 10 PM in One Minute. *Analytical Chemistry* 2020, *92* (9), 6654–6666. https://doi.org/10.1021/acs.analchem.0c00534.

(44) Bhasin, A.; Ogata, A. F.; Briggs, J. S.; Tam, P. Y.; Tan, M. X.; Weiss, G. A.; Penner, R. M. The Virus Bioresistor: Wiring Virus Particles for the Direct, Label-Free Detection of Target Proteins. *Nano Letters* 2018, *18* (6), 3623–3629. https://doi.org/10.1021/acs.nanolett.8b00723.

(45) Taggart, D. K.; Yang, Y.; Kung, S.-C.; McIntire, T. M.; Penner, R. M. Enhanced Thermoelectric Metrics in Ultra-Long Electrodeposited PEDOT Nanowires. *Nano Letters* 2011, *11* (1), 125–131. https://doi.org/10.1021/nl103003d.

(46) Xiang, C.; Kung, S.-C.; Taggart, D. K.; Yang, F.; Thompson, M. A.; Güell, A. G.; Yang, Y.; Penner, R. M. Lithographically Patterned Nanowire Electrodeposition: A Method for Patterning Electrically Continuous Metal Nanowires on Dielectrics. *ACS Nano* 2008, *2* (9), 1939–1949. https://doi.org/10.1021/nn800394k.

(47) Xiang, C.; Yang, Y.; Penner, R. M. Cheating the Diffraction Limit: Electrodeposited Nanowires Patterned by Photolithography. *Chemical Communications* 2009, No. 8, 859. https://doi.org/10.1039/b815603d.

(48) Lamboy, J. A.; Arter, J. A.; Knopp, K. A.; Der, D.; Overstreet, C. M.; Palermo, E. F.; Urakami, H.; Yu, T.-B.; Tezgel, O.; Tew, G. N.; Guan, Z.; Kuroda, K.; Weiss, G. A. Phage Wrapping with Cationic Polymers Eliminates Nonspecific Binding between M13 Phage and High p I Target Proteins. *J Am Chem Soc* 2009, *131* (45), 16454–16460. https://doi.org/10.1021/ja9050873.

(49) Donavan, K. C.; Arter, J. A.; Weiss, G. A.; Penner, R. M. Virus-Poly(3,4-Ethylenedioxythiophene) Biocomposite Films. *Langmuir* 2012, *28* (34), 12581–12587. https://doi.org/10.1021/la302473j.

(50) Arter, J. A.; Taggart, D. K.; McIntire, T. M.; Penner, R. M.; Weiss, G. A. Virus-PEDOT Nanowires for Biosensing. *Nano Letters* 2010, *10* (12), 4858–4862. https://doi.org/10.1021/nl1025826.

(51) Donavan, K. C.; Arter, J. A.; Pilolli, R.; Cioffi, N.; Weiss, G. A.; Penner, R. M. Virus-Poly(3,4-Ethylenedioxythiophene) Composite Films for Impedance-Based Biosensing. *Analytical Chemistry* 2011, *83* (7), 2420–2424. https://doi.org/10.1021/ac2000835.

(52) Arter, J. A.; Diaz, J. E.; Donavan, K. C.; Yuan, T.; Penner, R. M.; Weiss, G. A. Virus–Polymer Hybrid Nanowires Tailored to Detect Prostate-Specific Membrane Antigen. *Anal. Chem.* 2012, *84* (6), 2776–2783. https://doi.org/10.1021/ac203143y.

(53) Yang, L.-M. C.; Diaz, J. E.; McIntire, T. M.; Weiss, G. A.; Penner, R. M. Covalent Virus Layer for Mass-Based Biosensing. *Analytical Chemistry* 2008, *80* (4), 933–943. https://doi.org/10.1021/ac071470f.

(54) Diaz, J. E.; Yang, L.-M. C.; Lamboy, J. A.; Penner, R. M.; Weiss, G. A. Synthesis of a Virus Electrode for Measurement of Prostate Specific Membrane Antigen. In *Methods in molecular biology (Clifton, N.J.)*; 2009; pp 255–274. https://doi.org/10.1007/978-1-60327-569-9_16.

(55) Mohan, K.; Penner, R. M.; Weiss, G. A. Biosensing with Virus Electrode Hybrids. *Current Protocols in Chemical Biology* 2015, *7* (2), 53–72. https://doi.org/10.1002/9780470559277.ch140213.

(56) Yang, L.-M. C.; Diaz, J. E.; McIntire, T. M.; Weiss, G. A.; Penner, R. M. Direct Electrical Transduction of Antibody Binding to a Covalent Virus Layer Using Electrochemical Impedance. *Analytical Chemistry* 2008, *80* (15), 5695–5705. https://doi.org/10.1021/ac8008109.

(57) Ogata, A. F.; Edgar, J. M.; Majumdar, S.; Briggs, J. S.; Patterson, S. V.; Tan, M. X.; Kudlacek, S. T.; Schneider, C. A.; Weiss, G. A.; Penner, R. M. Virus-Enabled Biosensor for Human Serum Albumin. *Analytical Chemistry* 2017, *89* (2), 1373–1381. https://doi.org/10.1021/acs.analchem.6b04840.

(58) Mohan, K.; Donavan, K. C.; Arter, J. A.; Penner, R. M.; Weiss, G. A. Sub-Nanomolar Detection of Prostate-Specific Membrane Antigen in Synthetic Urine by Synergistic, Dual-Ligand Phage. *J Am Chem Soc* 2013, *135* (20), 7761–7767. https://doi.org/10.1021/ja4028082.

(59) Di Meo, A.; Bartlett, J.; Cheng, Y.; Pasic, M. D.; Yousef, G. M. Liquid Biopsy: A Step Forward towards Precision Medicine in Urologic Malignancies. *Molecular Cancer*. 2017. https://doi.org/10.1186/s12943-017-0644-5.

(60) Soukup, V.; Capoun, O.; Pesl, M.; Vavrova, L.; Sobotka, R.; Levova, K.; Hanus, T.; Zima, T.; Kalousova, M. The Significance of Calprotectin, CD147, APOA4 and DJ-1 in Non-Invasive Detection of Urinary Bladder Carcinoma. *Neoplasma* 2019. https://doi.org/10.4149/neo_2019_190124N74.

(61) Kumar, P.; Nandi, S.; Tan, T. Z.; Ler, S. G.; Chia, K. S.; Lim, W.-Y.; Bütow, Z.; Vordos, D.; De laTaille, A.; Al-Haddawi, M.; Raida, M.; Beyer, B.; Ricci, E.; Colombel, M.; Chong, T. W.; Chiong, E.; Soo, R.; Park, M. K.; Ha, H. K.; Gunaratne, J.; Thiery, J. P. Highly Sensitive and Specific Novel Biomarkers for the Diagnosis of Transitional Bladder Carcinoma. *Oncotarget* 2015, *6* (15). https://doi.org/10.18632/oncotarget.3841.

(62) Ku, J. Y.; Lee, C. H.; Lee, K.; Kim, K. H.; Baek, S. R.; Park, J. H.; Lee, J. Z.; Park, H. J.; Han, S. H.; Jeong, I. Y.; Kwon, M. J.; Ha, H. K.; Jean, P. T. Highly Sensitive and Specific Novel Biomarkers for the Diagnosis of Transitional Bladder Carcinoma. *European Urology Supplements* 2017, *16* (3), e1450–e1453. https://doi.org/10.1016/S1569-9056(17)30884-9.

(63) D'Costa, J. J.; Goldsmith, J. C.; Wilson, J. S.; Bryan, R. T.; Ward, D. G. A Systematic Review of the Diagnostic and Prognostic Value of Urinary Protein Biomarkers in Urothelial Bladder Cancer. *Bladder Cancer* 2016, *2* (3), 301–317. https://doi.org/10.3233/BLC-160054.

(64) Yang, L.-M. C.; Tam, P. Y.; Murray, B. J.; McIntire, T. M.; Overstreet, C. M.; Weiss, G. A.; Penner, R. M. Virus Electrodes for Universal Biodetection. *Analytical Chemistry* 2006, *78* (10), 3265–3270. https://doi.org/10.1021/ac052287u.

(65) Yang, L.-M. C.; Diaz, J. E.; McIntire, T. M.; Weiss, G. A.; Penner, R. M. Covalent Virus Layer for Mass-Based Biosensing. *Analytical Chemistry* 2008, *80* (4), 933–943. https://doi.org/10.1021/ac071470f.

(66) Donavan, K. C.; Arter, J. A.; Pilolli, R.; Cioffi, N.; Weiss, G. A.; Penner, R. M. Virus−Poly(3,4-Ethylenedioxythiophene) Composite Films for Impedance-Based Biosensing. *Analytical Chemistry* 2011, *83* (7), 2420–2424. https://doi.org/10.1021/ac2000835.

(67) Arter, J. A.; Diaz, J. E.; Donavan, K. C.; Yuan, T.; Penner, R. M.; Weiss, G. A. Virus-Polymer Hybrid Nanowires Tailored to Detect Prostate-Specific Membrane Antigen. *Analytical Chemistry* 2012. https://doi.org/10.1021/ac203143y.

(68) Mohan, K.; Donavan, K. C.; Arter, J. A.; Penner, R. M.; Weiss, G. A. Sub-Nanomolar Detection of Prostate-Specific Membrane Antigen in Synthetic Urine by Synergistic, Dual-Ligand Phage. *J Am Chem Soc* 2013, *135* (20), 7761–7767. https://doi.org/10.1021/ja4028082.

(69) Seki, Y.; Takahashi, M.; Takashiri, M. Effects of Different Electrolytes and Film Thicknesses on Structural and Thermoelectric Properties of Electropolymerized Poly(3,4-Ethylenedioxythiophene) Films. *RSC Advances* 2019, *9* (28), 15957–15965. https://doi.org/10.1039/C9RA02310K.

(70) Purdy, K. R.; Fraden, S. Isotropic-Cholesteric Phase Transition of Filamentous Virus Suspensions as a Function of Rod Length and Charge. *Physical Review E* 2004, *70* (6), 061703. https://doi.org/10.1103/PhysRevE.70.061703.

(71) Donavan, K. C.; Arter, J. A.; Weiss, G. A.; Penner, R. M. Virus-Poly(3,4-Ethylenedioxythiophene) Biocomposite Films. *Langmuir* 2012, *28* (34), 12581–12587. https://doi.org/10.1021/la302473j.

(72) Kim, D.-J.; Lee, N.-E.; Park, J.-S.; Park, I.-J.; Kim, J.-G.; Cho, H. J. Organic Electrochemical Transistor Based Immunosensor for Prostate Specific Antigen (PSA) Detection Using Gold Nanoparticles for Signal Amplification. *Biosensors and Bioelectronics* 2010, *25* (11), 2477–2482. https://doi.org/10.1016/j.bios.2010.04.013.

(73) Picca, R. A.; Manoli, K.; Macchia, E.; Sarcina, L.; Di Franco, C.; Cioffi, N.; Blasi, D.; Österbacka, R.; Torricelli, F.; Scamarcio, G.; Torsi, L. Ultimately Sensitive Organic Bioelectronic Transistor Sensors by Materials and Device Structures' Design. *Advanced Functional Materials* 2019, *1904513*, 1904513. https://doi.org/10.1002/adfm.201904513.

(74) Gentili, D.; D'Angelo, P.; Militano, F.; Mazzei, R.; Poerio, T.; Brucale, M.; Tarabella, G.; Bonetti, S.; Marasso, S. L.; Cocuzza, M.; Giorno, L.; Iannotta, S.; Cavallini, M. Integration of Organic Electrochemical Transistors and Immuno-Affinity Membranes for Label-Free Detection of Interleukin-6 in the Physiological Concentration Range through Antibody–Antigen Recognition. *Journal of Materials Chemistry B* 2018, *6* (33), 5400–5406. https://doi.org/10.1039/C8TB01697F.

(75) Gualandi, I.; Tessarolo, M.; Mariani, F.; Cramer, T.; Tonelli, D.; Scavetta, E.; Fraboni, B. Nanoparticle Gated Semiconducting Polymer for a New Generation of Electrochemical Sensors. *Sensors and Actuators B: Chemical* 2018, *273*, 834–841. https://doi.org/10.1016/j.snb.2018.06.109.

(76) Kim, Y.; Lim, T.; Kim, C.-H.; Yeo, C. S.; Seo, K.; Kim, S.-M.; Kim, J.; Park, S. Y.; Ju, S.; Yoon, M.-H. Organic Electrochemical Transistor-Based Channel Dimension-Independent Single-Strand Wearable Sweat Sensors. *NPG Asia Materials* 2018, *10* (11), 1086–1095. https://doi.org/10.1038/s41427-018-0097-3.

(77) Macchia, E.; Romele, P.; Manoli, K.; Ghittorelli, M.; Magliulo, M.; Kovács-Vajna, Z. M.; Torricelli, F.; Torsi, L. Ultra-Sensitive Protein Detection with Organic Electrochemical Transistors Printed on Plastic Substrates. *Flexible and Printed Electronics* 2018, *3* (3), 034002. https://doi.org/10.1088/2058-8585/aad0cb.

(78) Fu, Y.; Wang, N.; Yang, A.; Law, H. K.; Li, L.; Yan, F. Highly Sensitive Detection of Protein Biomarkers with Organic Electrochemical Transistors. *Advanced Materials* 2017, *29* (41), 1703787. https://doi.org/10.1002/adma.201703787.

(79) Gualandi, I.; Tonelli, D.; Mariani, F.; Scavetta, E.; Marzocchi, M.; Fraboni, B. Selective Detection of Dopamine with an All PEDOT:PSS Organic Electrochemical Transistor. *Scientific Reports* 2016, *6* (1), 35419. https://doi.org/10.1038/srep35419.

(80) Zhang, F.; Johansson, M.; Andersson, M. R.; Hummelen, J. C.; Inganäs, O. Polymer Photovoltaic Cells with Conducting Polymer Anodes. *Advanced Materials* 2002, *14* (9), 662–665. https://doi.org/10.1002/1521-4095(20020503)14:9<662::AID-ADMA662>3.0.CO;2-N.

(81) Pasha, A.; Khasim, S.; Al-Hartomy, O. A.; Lakshmi, M.; Manjunatha, K. G. Highly Sensitive Ethylene Glycol-Doped PEDOT–PSS Organic Thin Films for LPG Sensing. *RSC Advances* 2018, *8* (32), 18074–18083. https://doi.org/10.1039/C8RA01061G.

(82) Thomas, J. P.; Zhao, L.; McGillivray, D.; Leung, K. T. High-Efficiency Hybrid Solar Cells by Nanostructural Modification in PEDOT:PSS with Co-Solvent Addition. *Journal of Materials Chemistry A* 2014, *2* (7), 2383–2389. https://doi.org/10.1039/c3ta14590e.

(83) Ouyang, J.; Xu, Q.; Chu, C.-W.; Yang, Y.; Li, G.; Shinar, J. On the Mechanism of Conductivity Enhancement in Poly(3,4-Ethylenedioxythiophene):Poly(Styrene Sulfonate)

Film through Solvent Treatment. *Polymer (Guildf)* 2004, *45* (25), 8443–8450. https://doi.org/10.1016/j.polymer.2004.10.001.

(84) Poverenov, E.; Li, M.; Bitler, A.; Bendikov, M. Major Effect of Electropolymerization Solvent on Morphology and Electrochromic Properties of PEDOT Films. *Chemistry of Materials* 2010, *22* (13), 4019–4025. https://doi.org/10.1021/cm100561d.

(85) (nee Włodarczyk), K. C.; Karczewski, J.; Jasiński, P. Influence of Electropolymerization Conditions on the Morphological and Electrical Properties of PEDOT Film. *Electrochimica Acta* 2015, *176*, 156–161. https://doi.org/10.1016/j.electacta.2015.07.006.

(86) Brug, G. J.; van den Eeden, A. L. G.; Sluyters-Rehbach, M.; Sluyters, J. H. The Analysis of Electrode Impedances Complicated by the Presence of a Constant Phase Element. *Journal of Electroanalytical Chemistry and Interfacial Electrochemistry* 1984, *176* (1–2), 275–295. https://doi.org/10.1016/S0022-0728(84)80324-1.

(87) Kurganov, B. I.; Lobanov, A. V.; Borisov, I. A.; Reshetilov, A. N. Criterion for Hill Equation Validity for Description of Biosensor Calibration Curves. *Analytica Chimica Acta* 2001, *427* (1), 11–19. https://doi.org/10.1016/S0003-2670(00)01167-3.

(88) Islam, F.; Haque, M. H.; Yadav, S.; Islam, M. N.; Gopalan, V.; Nguyen, N.-T.; Lam, A. K.; Shiddiky, M. J. A. An Electrochemical Method for Sensitive and Rapid Detection of FAM134B Protein in Colon Cancer Samples. *Scientific Reports* 2017, *7* (1), 133. https://doi.org/10.1038/s41598-017-00206-8.

(89) Frey, B. L.; Jordan, C. E.; Kornguth, Steven.; Corn, R. M. Control of the Specific Adsorption of Proteins onto Gold Surfaces with Poly(L-Lysine) Monolayers. *Analytical Chemistry* 1995, *67* (24), 4452–4457. https://doi.org/10.1021/ac00120a003.

(90) Pasinszki, T.; Krebsz, M.; Tung, T. T.; Losic, D. Carbon Nanomaterial Based Biosensors for Non-Invasive Detection of Cancer and Disease Biomarkers for Clinical Diagnosis. *Sensors* 2017, *17* (8), 1919. https://doi.org/10.3390/s17081919.

(91) Ortiz-Aguayo, D.; del Valle, M. Label-Free Aptasensor for Lysozyme Detection Using Electrochemical Impedance Spectroscopy. *Sensors* 2018, *18* (2), 354. https://doi.org/10.3390/s18020354.

(92) Roda, A.; Michelini, E.; Zangheri, M.; Di Fusco, M.; Calabria, D.; Simoni, P. Smartphone-Based Biosensors: A Critical Review and Perspectives. *TrAC Trends in Analytical Chemistry* 2016, *79*, 317–325. https://doi.org/10.1016/j.trac.2015.10.019.

(93) Brás, E. J. S.; Fortes, A. M.; Chu, V.; Fernandes, P.; Conde, J. P. Microfluidic Device for the Point of Need Detection of a Pathogen Infection Biomarker in Grapes. *Analyst* 2019, *144* (16), 4871–4879. https://doi.org/10.1039/C9AN01002E.

(94) Kaisti, M. Detection Principles of Biological and Chemical FET Sensors. *Biosensors and Bioelectronics* 2017, *98*, 437–448. https://doi.org/10.1016/j.bios.2017.07.010.

(95) Karr, L. J.; Shafer, S. G.; Harris, J. M.; Van Alstine, J. M.; Snyder, R. S. Immuno-Affinity Partition of Cells in Aqueous Polymer Two-Phase Systems. *Journal of Chromatography A* 1986, *354* (C), 269–282. https://doi.org/10.1016/S0021-9673(01)87028-X.

(96) Field, C. R.; Yeom, J.; Salehi-Khojin, A.; Masel, R. I. Robust Fabrication of Selective and Reversible Polymer Coated Carbon Nanotube-Based Gas Sensors. *Sensors and Actuators B: Chemical* 2010, *148* (1), 315–322. https://doi.org/10.1016/j.snb.2010.05.026.

(97) Alizadeh, T.; Rezaloo, F. A New Chemiresistor Sensor Based on a Blend of Carbon Nanotube, Nano-Sized Molecularly Imprinted Polymer and Poly Methyl Methacrylate for the Selective and Sensitive Determination of Ethanol Vapor. *Sensors and Actuators B: Chemical* 2013, *176*, 28–37. https://doi.org/10.1016/j.snb.2012.08.049.

(98) Llobet, E. Gas Sensors Using Carbon Nanomaterials: A Review. *Sensors and Actuators B: Chemical* 2013, *179*, 32–45. https://doi.org/10.1016/j.snb.2012.11.014.

(99) Hangarter, C. M.; Chartuprayoon, N.; Hernández, S. C.; Choa, Y.; Myung, N. V. Hybridized Conducting Polymer Chemiresistive Nano-Sensors. *Nano Today* 2013, *8* (1), 39–55. https://doi.org/10.1016/j.nantod.2012.12.005.

(100) Doleman, B. J.; Sanner, R. D.; Severin, E. J.; Grubbs, R. H.; Lewis, N. S. Use of Compatible Polymer Blends To Fabricate Arrays of Carbon Black−Polymer Composite Vapor Detectors. *Analytical Chemistry* 1998, *70* (13), 2560–2564. https://doi.org/10.1021/ac971238h.

(101) Lux, F. Models Proposed to Explain the Electrical Conductivity of Mixtures Made of Conductive and Insulating Materials. *Journal of Materials Science*. 1993. https://doi.org/10.1007/BF00357799.

(102) McLachlan, D. S.; Blaszkiewicz, M.; Newnham, R. E. Electrical Resistivity of Composites. *Journal of the American Ceramic Society* 1990. https://doi.org/10.1111/j.1151-2916.1990.tb07576.x.

(103) Sauerbrey, G. Use of Crystal Oscillators for Weighing Thin Films and for Microweighing. *Zeitschrift fuer Physik* 1959.

(104) Kondo, A.; Murakami, F.; Higashitani, K. Circular Dichroism Studies on Conformational Changes in Protein Molecules upon Adsorption on Ultrafine Polystyrene Particles. *Biotechnology and Bioengineering* 1992, *40* (8), 889–894. https://doi.org/10.1002/bit.260400804.

(105) Rodahl, M.; Höök, F.; Fredriksson, C.; Keller, C. A.; Krozer, A.; Brzezinski, P.; Voinova, M.; Kasemo, B. Simultaneous Frequency and Dissipation Factor QCM Measurements of Biomolecular Adsorption and Cell Adhesion. *Faraday Discussions* 1997. https://doi.org/10.1039/a703137h.

(106) Honbou, K.; Suzuki, N. N.; Horiuchi, M.; Niki, T.; Taira, T.; Ariga, H.; Inagaki, F. The Crystal Structure of DJ-1, a Protein Related to Male Fertility and Parkinson's Disease. *Journal of Biological Chemistry* 2003, *278* (33), 31380–31384. https://doi.org/10.1074/jbc.M305878200.

(107) Allen J. Bard, L. R. F. *Electrochemical Methods: Fundamentals and Applications, 2nd Edition*; 2001.

(108) Walters, R. R.; Graham, J. F.; Moore, R. M.; Anderson, D. J. Protein Diffusion Coefficient Measurements by Laminar Flow Analysis: Method and Applications. *Analytical Biochemistry* 1984. https://doi.org/10.1016/0003-2697(84)90152-0.

(109) Cheng, C.-M.; Kuan, C.-M.; Chen, C.-F. *In-Vitro Diagnostic Devices*; Springer International Publishing: Cham, 2016. https://doi.org/10.1007/978-3-319-19737-1.

(110) McDonnell, B.; Hearty, S.; Leonard, P.; O'Kennedy, R. Cardiac Biomarkers and the Case for Point-of-Care Testing. *Clinical Biochemistry* 2009, *42* (7–8), 549–561. https://doi.org/10.1016/j.clinbiochem.2009.01.019.

(111) Gubala, V.; Harris, L. F.; Ricco, A. J.; Tan, M. X.; Williams, D. E. Point of Care Diagnostics: Status and Future. *Analytical Chemistry* 2012, *84* (2), 487–515. https://doi.org/10.1021/ac2030199.

(112) Fan, J.; Rezaie, S. S.; Facchini-Rakovich, M.; Gudi, D.; Montemagno, C.; Gupta, M. Tuning PEDOT:PSS Conductivity to Obtain Complementary Organic Electrochemical Transistor. *Organic Electronics* 2019, *66*, 148–155. https://doi.org/10.1016/j.orgel.2018.12.013.

(113) Drillet, J.-F.; Dittmeyer, R.; Jüttner, K. Activity and Long-Term Stability of PEDOT as Pt Catalyst Support for the DMFC Anode. *Journal of Applied Electrochemistry* 2007, *37* (11), 1219–1226. https://doi.org/10.1007/s10800-007-9393-2.

(114) Özcan, A.; İlkbaş, S. Preparation of Poly(3,4-Ethylenedioxythiophene) Nanofibers Modified Pencil Graphite Electrode and Investigation of over-Oxidation Conditions for the Selective and Sensitive Determination of Uric Acid in Body Fluids. *Analytica Chimica Acta* 2015, *891*, 312–320. https://doi.org/10.1016/j.aca.2015.08.015.

(115) Gorduk, O. Differential Pulse Voltammetric Determination of Serotonin Using an Acid-Activated Multiwalled Carbon Nanotube – Over-Oxidized Poly(3,4-Ethylenedioxythiophene) Modified Pencil Graphite Electrode. *Analytical Letters* 2020, *53* (7), 1034–1052. https://doi.org/10.1080/00032719.2019.1693583.

(116) Tehrani, P.; Kanciurzewska, A.; Crispin, X.; Robinson, N.; Fahlman, M.; Berggren, M. The Effect of PH on the Electrochemical Over-Oxidation in PEDOT:PSS Films. *Solid State Ionics* 2007, *177* (39–40), 3521–3527. https://doi.org/10.1016/j.ssi.2006.10.008.

(117) Donavan, K. C.; Arter, J. A.; Pilolli, R.; Cioffi, N.; Weiss, G. A.; Penner, R. M. Virus−Poly(3,4-Ethylenedioxythiophene) Composite Films for Impedance-Based Biosensing. *Analytical Chemistry* 2011, *83* (7), 2420–2424. https://doi.org/10.1021/ac2000835.

(118) Donavan, K. C.; Arter, J. A.; Weiss, G. A.; Penner, R. M. Virus-Poly(3,4-Ethylenedioxythiophene) Biocomposite Films. *Langmuir* 2012, *28* (34), 12581–12587. https://doi.org/10.1021/la302473j.

(119) Field, C. R.; Yeom, J.; Salehi-Khojin, A.; Masel, R. I. Robust Fabrication of Selective and Reversible Polymer Coated Carbon Nanotube-Based Gas Sensors. *Sensors and Actuators B: Chemical* 2010, *148* (1), 315–322. https://doi.org/10.1016/j.snb.2010.05.026.

(120) Alizadeh, T.; Rezaloo, F. A New Chemiresistor Sensor Based on a Blend of Carbon Nanotube, Nano-Sized Molecularly Imprinted Polymer and Poly Methyl Methacrylate for the Selective and Sensitive Determination of Ethanol Vapor. *Sensors and Actuators B: Chemical* 2013, *176*, 28–37. https://doi.org/10.1016/j.snb.2012.08.049.

(121) Llobet, E. Gas Sensors Using Carbon Nanomaterials: A Review. *Sensors and Actuators B: Chemical* 2013, *179*, 32–45. https://doi.org/10.1016/j.snb.2012.11.014.

(122) Hangarter, C. M.; Chartuprayoon, N.; Hernández, S. C.; Choa, Y.; Myung, N. V. Hybridized Conducting Polymer Chemiresistive Nano-Sensors. *Nano Today* 2013, *8* (1), 39–55. https://doi.org/10.1016/j.nantod.2012.12.005.

(123) Doleman, B. J.; Sanner, R. D.; Severin, E. J.; Grubbs, R. H.; Lewis, N. S. Use of Compatible Polymer Blends To Fabricate Arrays of Carbon Black−Polymer Composite Vapor Detectors. *Analytical Chemistry* 1998, *70* (13), 2560–2564. https://doi.org/10.1021/ac971238h.

(124) Karr, L. J.; Shafer, S. G.; Harris, J. M.; Van Alstine, J. M.; Snyder, R. S. Immuno-Affinity Partition of Cells in Aqueous Polymer Two-Phase Systems. *Journal of Chromatography A* 1986, *354* (C), 269–282. https://doi.org/10.1016/S0021-9673(01)87028-X.

(125) Kawahara, J.; Ersman, P. A.; Engquist, I.; Berggren, M. Improving the Color Switch Contrast in PEDOT:PSS-Based Electrochromic Displays. *Organic Electronics* 2012, *13* (3), 469–474. https://doi.org/10.1016/j.orgel.2011.12.007.

(126) Andreev, A.; Matt, G.; Brabec, C. J.; Sitter, H.; Badt, D.; Seyringer, H.; Dean DeLongchamp, B.; Hammond, P. T.; Hammond, P. T.; DeLongchamp, D.; authors thank D Tovar, T. J.; Timothy Swager, P. *Layer-by-Layer Assembly of PEDOT/Polyaniline Electrochromic Devices***; 1996; Vol. 34.

(127) Zozoulenko, I.; Singh, A.; Singh, S. K.; Gueskine, V.; Crispin, X.; Berggren, M. Polarons, Bipolarons, And Absorption Spectroscopy of PEDOT. *ACS Applied Polymer Materials* 2019, *1* (1). https://doi.org/10.1021/acsapm.8b00061.

(128) Tehrani, P.; Kanciurzewska, A.; Crispin, X.; Robinson, N. D.; Fahlman, M.; Berggren, M. The Effect of PH on the Electrochemical Over-Oxidation in PEDOT:PSS Films. *Solid State Ionics* 2007, *177* (39–40), 3521–3527. https://doi.org/10.1016/j.ssi.2006.10.008.

(129) Fan, J.; Rezaie, S. S.; Facchini-Rakovich, M.; Gudi, D.; Montemagno, C.; Gupta, M. Tuning PEDOT:PSS Conductivity to Obtain Complementary Organic Electrochemical Transistor. *Organic Electronics* 2019, *66*, 148–155. https://doi.org/10.1016/j.orgel.2018.12.013.

(130) Zhou, C.; Liu, Z.; Du, X.; Ringer, S. P. Electrodeposited PEDOT Films on ITO with a Flower-like Hierarchical Structure. *Synthetic Metals* 2010, *160* (15–16), 1636–1641. https://doi.org/10.1016/j.synthmet.2010.05.033.

(131) Kurganov, B. I.; Lobanov, A. V.; Borisov, I. A.; Reshetilov, A. N. Criterion for Hill Equation Validity for Description of Biosensor Calibration Curves. *Analytica Chimica Acta* 2001, *427* (1), 11–19. https://doi.org/10.1016/S0003-2670(00)01167-3.

(132) Cremer, M. Origin of Electromotor Properties of Tissues, and Instructional Contribution for Polyphasic Electrolyte Chains. *Z Biol* 1906, *47*, 562–608.

(133) Hirakawa, S.; Yoshimura, H. Measurements of the Intracellular PH in a Single Cell of Nitella Flexilis By Means of Micro-Glass PH Electrodes. 1964, *14*, 45–55.

(134) Aref, M.; Ranjbari, E.; García-Guzmán, J. J.; Hu, K.; Lork, A.; Crespo, G. A.; Ewing, A. G.; Cuartero, M. Potentiometric PH Nanosensor for Intracellular Measurements: Real-Time and Continuous Assessment of Local Gradients. *Analytical Chemistry* 2021, *93* (47), 15744–15751. https://doi.org/10.1021/acs.analchem.1c03874.

(135) Cui, Y.; Wei, Q.; Park, H.; Lieber, C. M. Nanowire Nanosensors for Highly Sensitive and Selective Detection of Biological and Chemical Species. *Science (1979)* 2001, *293* (5533), 1289–1292. https://doi.org/10.1126/science.1062711.

(136) Fujisaku, T.; Tanabe, R.; Onoda, S.; Kubota, R.; Segawa, T. F.; So, F. T. K.; Ohshima, T.; Hamachi, I.; Shirakawa, M.; Igarashi, R. PH Nanosensor Using Electronic Spins in Diamond. *ACS Nano* 2019, *13* (10), 11726–11732. https://doi.org/10.1021/acsnano.9b05342.

(137) Shen, J.; Xiao, Q.; Sun, P.; Feng, J.; Xin, X.; Yu, Y.; Qi, W. Self-Assembled Chiral Phosphorescent Microflowers from Au Nanoclusters with Dual-Mode PH Sensing and Information Encryption. *ACS Nano* 2021, *15* (3), 4947–4955. https://doi.org/10.1021/acsnano.0c09766.

(138) He, J.; Forzani, E. S.; Nagahara, L. A.; Tao, N.; Lindsay, S. Charge Transport in Mesoscopic Conducting Polymer Wires. *Journal of Physics Condensed Matter* 2008, *20* (37). https://doi.org/10.1088/0953-8984/20/37/374120.

(139) Aguilar, A. D.; Forzani, E. S.; Tao, N. J.; Nagahara, L. A.; Amlani, I.; Tsui, R. A Breath Ammonia Sensor Based on Conducting Polymer Nanojunctions. *IEEE Sensors Journal*. 2008, pp 269–273. https://doi.org/10.1109/JSEN.2007.913137.

(140) Forzani, E. S.; Li, X.; Tao, N. Hybrid Amperometric and Conductometric Chemical Sensor Based on Conducting Polymer Nanojunctions. *Analytical Chemistry* 2007, *79* (14), 5217–5224. https://doi.org/10.1021/ac0703202.

(141) Díaz Aguilar, A.; Forzani, E. S.; Leright, M.; Tsow, F.; Cagan, A.; Iglesias, R. A.; Nagahara, L. A.; Amlani, I.; Tsui, R.; Tao, N. J.; Aguilar, A. D.; Forzani, E. S.; Leright, M.; Tsow, F.; Cagan, A.; Iglesias, R. A.; Nagahara, L. A.; Amlani, I.; Tsui, R.; Tao, N. J.; Díaz Aguilar, A.; Forzani, E. S.; Leright, M.; Tsow, F.; Cagan, A.; Iglesias, R. A.; Nagahara, L. A.; Amlani, I.; Tsui, R.; Tao, N. J. A Hybrid Nanosensor for TNT Vapor Detection. *Nano Letters* 2010, *10* (2), 380–384. https://doi.org/10.1021/nl902382s.

(142) Forzani, E. S.; Zhang, H.; Nagahara, L. A.; Amlani, I.; Tsui, R.; Tao, N. A Conducting Polymer Nanojunction Sensor for Glucose Detection. *Nano Letters* 2004, *4* (9), 1785–1788. https://doi.org/10.1021/nl049080l.

(143) MacDiarmid, A. G.; Manohar, S. K.; Masters, J. G.; Sun, Y.; Weiss, H.; Epstein, A. J. Polyaniline: Synthesis and Properties of Pernigraniline Base. *Synthetic Metals* 1991, *41* (1–2), 621–626. https://doi.org/10.1016/0379-6779(91)91145-Z.

(144) Dan, L. I.; Huang, J.; Kaner, R. B. Polyaniline Nanofibers: A Unique Polymer Nanostructure for Versatile Applications. *Accounts of Chemical Research* 2009, *42* (1), 135–145. https://doi.org/10.1021/ar800080n.

(145) Huang, J.; Virji, S.; Weiller, B. H.; Kaner, R. B. Polyaniline Nanofibers: Facile Synthesis and Chemical Sensors. *J Am Chem Soc* 2003, *125* (2), 314–315. https://doi.org/10.1021/ja028371y.

(146) Song, E.; Choi, J. W. Self-Calibration of a Polyaniline Nanowire-Based Chemiresistive PH Sensor. *Microelectronic Engineering* 2014, *116*, 26–32. https://doi.org/10.1016/j.mee.2013.10.014.

(147) Bangar, M. A.; Shirale, D. J.; Chen, W.; Myung, N. V.; Mulchandani, A. Single Conducting Polymer Nanowire Chemiresistive Label-Free Immunosensor for Cancer Biomarker. *Analytical Chemistry* 2009, *81* (6), 2168–2175. https://doi.org/10.1021/ac802319f.

(148) Hangarter, C. M.; Hernandez, S. C.; He, X.; Chartuprayoon, N.; Choa, Y. H.; Myung, N. V. Tuning the Gas Sensing Performance of Single PEDOT Nanowire Devices. *Analyst* 2011, *136* (11), 2350–2358. https://doi.org/10.1039/c0an01000f.

(149) Liu, H.; Kameoka, J.; Czaplewski, D. A.; Craighead, H. G. Polymeric Nanowire Chemical Sensor. *Nano Letters* 2004, *4* (4), 671–675. https://doi.org/10.1021/nl049826f.

(150) Lee, S. Y.; Lim, H.; Choi, G. R.; Kim, J. Di; Suh, E. K.; Lee, S. K. Metal-to-Insulating Transition of Single Polyaniline (PANI) Nanowire: A Dedoping Effect. *Journal of Physical Chemistry C* 2010, *114* (27), 11936–11939. https://doi.org/10.1021/jp101424b.

(151) Xiang, C.; Kung, S. C.; Taggart, D. K.; Yang, F.; Thompson, M. A.; Güell, A. G.; Yang, Y.; Penner, R. M. Lithographically Patterned Nanowire Electrodeposition: A Method for Patterning Electrically Continuous Metal Nanowires on Dielectrics. *ACS Nano* 2008, *2* (9), 1939–1949. https://doi.org/10.1021/nn800394k.

(152) Xiang, C.; Kim, J. Y.; Penner, R. M. Reconnectable Sub-5 Nm Nanogaps in Ultralong Gold Nanowires. *Nano Letters* 2009, *9* (5), 2133–2138. https://doi.org/10.1021/nl900698s.

(153) Zhang, H.; Wang, J.; Wang, Z.; Zhang, F.; Wang, S. Electrodeposition of Polyaniline Nanostructures: A Lamellar Structure. *Synthetic Metals* 2009, *159* (3–4), 277–281. https://doi.org/10.1016/j.synthmet.2008.09.015.

(154) Menke, E. J.; Thompson, M. A.; Xiang, C.; Yang, L. C.; Penner, R. M. Lithographically Patterned Nanowire Electrodeposition. *Nature Materials* 2006, *5* (11), 914–919. https://doi.org/10.1038/nmat1759.

(155) Xing, W.; Hu, J.; Kung, S. C.; Donavan, K. C.; Yan, W.; Wu, R.; Penner, R. M. A Chemically-Responsive Nanojunction within a Silver Nanowire. *Nano Letters* 2012, *12* (3), 1729–1735. https://doi.org/10.1021/nl300427w.

(156) Durkan, C.; Welland, M. E. Analysis of Failure Mechanisms in Electrically Stressed Gold Nanowires. *Ultramicroscopy* 2000, *82* (1–4), 125–133. https://doi.org/10.1016/S0304-3991(99)00133-3.

(157) Hadeed, F. O.; Durkan, C. Controlled Fabrication of 1-2 Nm Nanogaps by Electromigration in Gold and Gold-Palladium Nanowires. *Applied Physics Letters* 2007, *91* (12), 2005–2008. https://doi.org/10.1063/1.2785982.

(158) Trouwborst, M. L.; Van Der Molen, S. J.; Van Wees, B. J. The Role of Joule Heating in the Formation of Nanogaps by Electromigration. *Journal of Applied Physics* 2006, *99* (11). https://doi.org/10.1063/1.2203410.

(159) Strachan, D. R.; Smith, D. E.; Johnston, D. E.; Park, T. H.; Therien, M. J.; Bonnell, D. A.; Johnson, A. T. Controlled Fabrication of Nanogaps in Ambient Environment for Molecular Electronics 043109. *Applied Physics Letters* 2005, *86* (4), 87–90. https://doi.org/10.1063/1.1857095.

(160) Johnston, D. E.; Strachan, D. R.; Johnson, A. T. C. Parallel Fabrication of Nanogap Electrodes. *Nano Letters* 2007, *7* (9), 2774–2777. https://doi.org/10.1021/nl0713169.

(161) Esen, G.; Fuhrer, M. S. Temperature Control of Electromigration to Form Gold Nanogap Junctions. *Applied Physics Letters* 2005, *87* (26), 1–3. https://doi.org/10.1063/1.2149174.

(162) Alexander, C. L.; Tribollet, B.; Orazem, M. E. Contribution of Surface Distributions to Constant-Phase-Element (CPE) Behavior: 2. Capacitance. *Electrochimica Acta* 2016, *188*, 566–573. https://doi.org/10.1016/j.electacta.2015.11.135.

(163) Islam, M. A. Einstein–Smoluchowski Diffusion Equation: A Discussion. *Physica Scripta* 2004, *70* (2–3), 120–125. https://doi.org/10.1088/0031-8949/70/2-3/008.

(164) Kanamura, K.; Kawai, Y.; Yonezawa, S.; Takehara, Z. Diffusion Behavior of Anions in Polyaniline during Electrochemical Undoping.2.Effect of the Preparation Conditions of Polyaniline on the Diffusion Coefficient of BF4-. *The Journal of Physical Chemistry* 1994, *98* (8), 2174–2179. https://doi.org/10.1021/j100059a034.

(165) Lim, J. H.; Phiboolsirichit, N.; Mubeen, S.; Deshusses, M. A.; Mulchandani, A.; Myung, N. V. Electrical and Gas Sensing Properties of Polyaniline Functionalized Single-Walled Carbon Nanotubes. *Nanotechnology* 2010, *21* (7), 075502. https://doi.org/10.1088/0957-4484/21/7/075502.

(166) Srinives, S.; Sarkar, T.; Hernandez, R.; Mulchandani, A. Potassium Iodide-Functionalized Polyaniline Nanothin Film Chemiresistor for Ultrasensitive Ozone Gas Sensing. *Polymers (Basel)* 2017, *9* (12), 80. https://doi.org/10.3390/polym9030080.

(167) Shirsat, M. D.; Bangar, M. A.; Deshusses, M. A.; Myung, N. V.; Mulchandani, A. Polyaniline Nanowires-Gold Nanoparticles Hybrid Network Based Chemiresistive Hydrogen Sulfide Sensor. *Applied Physics Letters* 2009, *94* (8). https://doi.org/10.1063/1.3070237.

(168) Lim, J. H.; Phiboolsirichit, N.; Mubeen, S.; Deshusses, M. A.; Mulchandani, A.; Myung, N. V. Electrical and Gas Sensing Properties of Polyaniline Functionalized Single-Walled Carbon Nanotubes. *Nanotechnology* 2010, *21* (7), 075502. https://doi.org/10.1088/0957-4484/21/7/075502.

(169) Chartier, P.; Mattes, B.; Reiss, H. Donnan Phenomena in the Proton Doping of Emeraldine. *Journal of Physical Chemistry* 1992, *96* (8), 3556–3560. https://doi.org/10.1021/j100187a068.

(170) Bates, R. G. *Determination of PH, Theory and Practice*, 2nd ed.; Wiley, 1973.

(171) Bhasin, A.; Drago, N. P.; Majumdar, S.; Sanders, E. C.; Weiss, G. A.; Penner, R. M. Viruses Masquerading as Antibodies in Biosensors: The Development of the Virus BioResistor. *Accounts of Chemical Research* 2020, *53* (10), 2384–2394. https://doi.org/10.1021/acs.accounts.0c00474.

(172) Kindra, L. R.; Eggers, C. J.; Liu, A. T.; Mendoza, K.; Mendoza, J.; Klein Myers, A. R.; Penner, R. M. Lithographically Patterned PEDOT Nanowires for the Detection of Iron(III) with Nanomolar Sensitivity. *Analytical Chemistry* 2015, *87* (22), 11492–11500. https://doi.org/10.1021/acs.analchem.5b03255.

(173) Wustoni, S.; Combe, C.; Ohayon, D.; Akhtar, M. H.; McCulloch, I.; Inal, S. Membrane-Free Detection of Metal Cations with an Organic Electrochemical Transistor. *Advanced Functional Materials* 2019, *29* (44). https://doi.org/10.1002/adfm.201904403.

(174) Bedioui, F.; Devynck, J.; Claude, B. C. Immobilization of Metalloporphyrins in Electropolymerized Films: Design and Applications. *Accounts of Chemical Research* 1995, *28* (1), 30–36. https://doi.org/10.1021/ar00049a005.

(175) Park, J.; Sempionatto, J. R.; Kim, J.; Jeong, Y.; Gu, J.; Wang, J.; Park, I. Microscale Biosensor Array Based on Flexible Polymeric Platform toward Lab-on-a-Needle: Real-Time Multiparameter Biomedical Assays on Curved Needle Surfaces. *ACS Sensors* 2020, *5* (5), 1363–1373. https://doi.org/10.1021/acssensors.0c00078.

(176) Horng, Y. Y.; Hsu, Y. K.; Ganguly, A.; Chen, C. C.; Chen, L. C.; Chen, K. H. Direct-Growth of Polyaniline Nanowires for Enzyme-Immobilization and Glucose Detection. *Electrochemistry Communications* 2009, *11* (4), 850–853. https://doi.org/10.1016/j.elecom.2009.02.010.

(177) Garreau, S.; Louarn, G.; Buisson, J. P.; Froyer, G.; Lefrant, S. In Situ Spectroelectrochemical Raman Studies of Poly(3,4-Ethylenedioxythiophene) (PEDT). *Macromolecules* 1999, *32* (20), 6807–6812. https://doi.org/10.1021/ma9905674.

(178) Stavytska-Barba, M.; Kelley, A. M. Surface-Enhanced Raman Study of the Interaction of PEDOT: PSS with Plasmonically Active Nanoparticles. *Journal of Physical Chemistry C* 2010, *114* (14), 6822–6830. https://doi.org/10.1021/jp100135x.

(179) Chiu, W. W.; Travaš-Sejdić, J.; Cooney, R. P.; Bowmaker, G. A. Studies of Dopant Effects in Poly(3,4-Ethylenedioxythiophene) Using Raman Spectroscopy. *Journal of Raman Spectroscopy* 2006, *37* (12), 1354–1361. https://doi.org/10.1002/jrs.1545.

(180) Özcan, A.; İlkbaş, S. Preparation of Poly(3,4-Ethylenedioxythiophene) Nanofibers Modified Pencil Graphite Electrode and Investigation of over-Oxidation Conditions for the Selective and Sensitive Determination of Uric Acid in Body Fluids. *Analytica Chimica Acta* 2015, *891*, 312–320. https://doi.org/10.1016/j.aca.2015.08.015.

(181) Łapkowski, M.; Proń, A. Electrochemical Oxidation of Poly(3,4-Ethylenedioxythiophene) - `in Situ' Conductivity and Spectroscopic Investigations. *Synthetic Metals* 2000, *110* (1), 79–83. https://doi.org/10.1016/S0379-6779(99)00271-4.

(182) De Kok, M. M.; Buechel, M.; Vulto, S. I. E.; Van De Weyer, P.; Meulenkamp, E. A.; De Winter, S. H. P. M.; Mank, A. J. G.; Vorstenbosch, H. J. M.; Weijtens, C. H. L.; Van Elsbergen, V. Modification of PEDOT:PSS as Hole Injection Layer in Polymer LEDs. *Physica Status Solidi (A) Applied Research* 2004, *201* (6), 1342–1359. https://doi.org/10.1002/pssa.200404338.

(183) Garreau, S.; Louarn, G.; Buisson, J. P.; Froyer, G.; Lefrant, S. In Situ Spectroelectrochemical Raman Studies of Poly(3,4-Ethylenedioxythiophene) (PEDT). *Macromolecules* 1999, *32* (20), 6807–6812. https://doi.org/10.1021/ma9905674.

(184) Stavytska-Barba, M.; Kelley, A. M. Surface-Enhanced Raman Study of the Interaction of PEDOT: PSS with Plasmonically Active Nanoparticles. *Journal of Physical Chemistry C* 2010, *114* (14), 6822–6830. https://doi.org/10.1021/jp100135x.

(185) Chiu, W. W.; Travaš-Sejdić, J.; Cooney, R. P.; Bowmaker, G. A. Studies of Dopant Effects in Poly(3,4-Ethylenedioxythiophene) Using Raman Spectroscopy. *Journal of Raman Spectroscopy* 2006, *37* (12), 1354–1361. https://doi.org/10.1002/jrs.1545.

(186) Kamensky, M. A.; Eliseeva, S. N.; Láng, G.; Ujvári, M.; Kondratiev, V. V. Electrochemical Properties of Overoxidized Poly-3,4-Ethylenedioxythiophene. *Russian Journal of Electrochemistry* 2018, *54* (11), 893–901. https://doi.org/10.1134/S1023193518130219.

(187) Greczynski, G.; Kugler, T.; Salaneck, W. R. Characterization of the PEDOT-PSS System by Means of X-Ray and Ultraviolet Photoelectron Spectroscopy. *Thin Solid Films* 1999, *354* (1), 129–135. https://doi.org/10.1016/S0040-6090(99)00422-8.

(188) Xing, K. Z.; Fahlman, M.; Chen, X. W.; Inganäs, O.; Salaneck, W. R. The Electronic Structure of Poly(3,4-Ethylene-Dioxythiophene): Studied by XPS and UPS. *Synthetic Metals* 1997, *89* (3), 161–165. https://doi.org/10.1016/s0379-6779(97)81212-x.

(189) Szot-Karpińska, K.; Leśniewski, A.; Jönsson-Niedziółka, M.; Marken, F.; Niedziółka-Jönsson, J. Electrodes Modified with Bacteriophages and Carbon Nanofibres for Cysteine Detection. *Sensors and Actuators, B: Chemical* 2019, *287* (January), 78–85. https://doi.org/10.1016/j.snb.2019.01.148.

(190) Shen, J.; Xiao, Q.; Sun, P.; Feng, J.; Xin, X.; Yu, Y.; Qi, W. Self-Assembled Chiral Phosphorescent Microflowers from Au Nanoclusters with Dual-Mode PH Sensing and Information Encryption. *ACS Nano* 2021, *15* (3), 4947–4955. https://doi.org/10.1021/acsnano.0c09766.

(191) Fujisaku, T.; Tanabe, R.; Onoda, S.; Kubota, R.; Segawa, T. F.; So, F. T. K.; Ohshima, T.; Hamachi, I.; Shirakawa, M.; Igarashi, R. PH Nanosensor Using Electronic Spins in Diamond. *ACS Nano* 2019, *13* (10), 11726–11732. https://doi.org/10.1021/acsnano.9b05342.

(192) Laysandra, L.; Kurniawan, D.; Wang, C.-L.; Chiang, W.-H.; Chiu, Y.-C. Synergistic Effect in a Graphene Quantum Dot-Enabled Luminescent Skinlike Copolymer for Long-Term PH

Detection. *ACS Applied Materials & Interfaces* 2021. https://doi.org/10.1021/acsami.1c18077.

(193) Huang, W.; Chen, R.; Peng, Y.; Duan, F.; Huang, Y.; Guo, W.; Chen, X.; Nie, L. In Vivo Quantitative Photoacoustic Diagnosis of Gastric and Intestinal Dysfunctions with a Broad PH-Responsive Sensor. *ACS Nano* 2019, *13* (8), 9551–9570. https://doi.org/10.1021/acsnano.9b04541.

(194) Huynh, G. T.; Henderson, E. C.; Frith, J. E.; Meagher, L.; Corrie, S. R. Stability and Performance Study of Fluorescent Organosilica PH Nanosensors. *Langmuir* 2021, *37* (21), 6578–6587. https://doi.org/10.1021/acs.langmuir.1c00936.

(195) Huo, Z.; Chen, G.; Geng, Y.; Cong, L.; Pan, L.; Xu, W.; Xu, S. A Two-Photon Fluorescence, Carbonized Polymer Dot (CPD)-Based, Wide Range PH Nanosensor: A View from the Surface State. *Nanoscale* 2020, *12* (16), 9094–9103. https://doi.org/10.1039/d0nr01543a.

(196) Zhang, Q.; Inose, T.; Ricci, M.; Li, J.; Tian, Y.; Wen, H.; Toyouchi, S.; Fron, E.; Ngoc Dao, A. T.; Kasai, H.; Rocha, S.; Hirai, K.; Fortuni, B.; Uji-i, H. Gold-Photodeposited Silver Nanowire Endoscopy for Cytosolic and Nuclear PH Sensing. *ACS Applied Nano Materials* 2021, *4* (9), 9886–9894. https://doi.org/10.1021/acsanm.1c02363.

(197) Paek, K.; Yang, H.; Lee, J.; Park, J.; Kim, B. J. Efficient Colorimetric PH Sensor Based on Responsive Polymer-Quantum Dot Integrated Graphene Oxide. *ACS Nano* 2014, *8* (3), 2848–2856. https://doi.org/10.1021/nn406657b.

(198) Capocefalo, A.; Mammucari, D.; Brasili, F.; Fasolato, C.; Bordi, F.; Postorino, P.; Domenici, F. Exploring the Potentiality of a SERS-Active PH Nano-Biosensor. *Frontiers in Chemistry* 2019, *7* (June), 1–11. https://doi.org/10.3389/fchem.2019.00413.

(199) Zhang, W.; Abou El-Reash, Y. G.; Ding, L.; Lin, Z.; Lian, Y.; Song, B.; Yuan, J.; Wang, X. dong. A Lysosome-Targeting Nanosensor for Simultaneous Fluorometric Imaging of Intracellular PH Values and Temperature. *Microchimica Acta* 2018, *185* (12). https://doi.org/10.1007/s00604-018-3040-y.

(200) Theerasilp, M.; Crespy, D. Halochromic Polymer Nanosensors for Simple Visual Detection of Local PH in Coatings. *Nano Letters* 2021, *21* (8), 3604–3610. https://doi.org/10.1021/acs.nanolett.1c00620.

(201) Michalak, M.; Kurel, M.; Jedraszko, J.; Toczydlowska, D.; Wittstock, G.; Opallo, M.; Nogala, W. Voltammetric PH Nanosensor. *Analytical Chemistry* 2015, *87* (23), 11641–11645. https://doi.org/10.1021/acs.analchem.5b03482.

(202) Go, J.; Nair, P. R.; Reddy, B.; Dorvel, B.; Bashir, R.; Alam, M. A. Coupled Heterogeneous Nanowire-Nanoplate Planar Transistor Sensors for Giant (>10 V/PH) Nernst Response. *ACS Nano* 2012, *6*, 5972–5979.

(203) Zafar, S.; D'Emic, C.; Jagtiani, A.; Kratschmer, E.; Miao, X.; Zhu, Y.; Mo, R.; Sosa, N.; Hamann, H.; Shahidi, G.; Riel, H. Silicon Nanowire Field Effect Transistor Sensors with Minimal Sensor-to-Sensor Variations and Enhanced Sensing Characteristics. *ACS Nano* 2018, *12* (7), 6577–6587. https://doi.org/10.1021/acsnano.8b01339.

(204) Nakata, S.; Shiomi, M.; Fujita, Y.; Arie, T.; Akita, S.; Takei, K. A Wearable PH Sensor with High Sensitivity Based on a Flexible Charge-Coupled Device. *Nature Electronics* 2018, *1* (11), 596–603. https://doi.org/10.1038/s41928-018-0162-5.

(205) Park, H. J.; Yoon, J. H.; Lee, K. G.; Choi, B. G. Potentiometric Performance of Flexible PH Sensor Based on Polyaniline Nanofiber Arrays. *Nano Convergence* 2019, *6* (1). https://doi.org/10.1186/s40580-019-0179-0.

(206) Li, H.; Liu, S.; Li, X.; Hao, R.; Wang, X.; Zhang, W.; Zheng, Z.; Feng, Q. All-Solid, Ultra-Micro, and Ultrasensitive PH Sensor by Monolayer MoS2-Based Array Field-Effect Transistors. *ACS Applied Nano Materials* 2021, *4* (9), 8950–8957. https://doi.org/10.1021/acsanm.1c01568.

(207) Khademi, M.; Barz, D. P. J. Structure of the Electrical Double Layer Revisited: Electrode Capacitance in Aqueous Solutions. *Langmuir* 2020, *36* (16), 4250–4260. https://doi.org/10.1021/acs.langmuir.0c00024.

Appendix A: Supplementary Information for Chapter 2

A.1. Materials and Fabrication of VBR

Additional details relating to this process outlined in the Experimental Section are the following: Gold-film electrodes were cleaned by O_2 plasma for 10 min immediately before use. Scotch tape was placed on the ends of the electrodes to protect the contacts. To obtain low DC resistance PEDOT-PSS films, 3% (v/v) ethylene glycol was mixed with PEDOT-PSS at 550 rpm for 30 min. To obtain high DC resistance PEDOT-PSS films, 1.5% (v/v) ethylene glycol was mixed with PEDOT-PSS at 550 rpm for 30 minutes. The mixture was spin-coated on the gold electrodes at 2500 rpm, 80 s and baked for 1 h at 90 °C. Electrodes were then allowed to equilibrate at room temperature and the cell was then mounted on the gold-film electrodes followed by the incubation of the electrodes in PBS for 30 min. Next, virus-PEDOT films were electropolymerized onto the PEDOT-PSS/gold-film electrodes using a platinum foil counter and a mercurous sulfate electrode (MSE). Virus-PEDOT films were prepared by cycling between 0.2 V and 0.8 V at a scan rate of 20 mV/s in plating solution using a PARSTAT 2263 controlled by Electrochemistry PowerSuit 2.6 software. Plating solutions contained 8 nM M13 bacteriophage, 12.5 mM $LiClO_4$, 2.5 mM EDOT, and were electropolymerized for 2 cycles.

A.2. Process Windows Compliance Assessment of VBRs

VBRs were evaluated at every step of the fabrication process to ensure the reproducibility of signal at each DJ-1 concentration. Starting with the fabrication by photolithography of gold electrodes, the VBR is prepared in five steps (Figure A.1). The parameters measured at each of these steps is indicated in the diagram for Fig. 5.1. In this diagram, the following definitions apply: R_{au} is the dc resistance of the gold electrons prepared in

step 1, measured along their longest dimension, $R_{PEDOT-PSS}$ is the dc resistance of the PEDOT-PSS film produced in step 2, Z_{im} and Z_{re} are the baseline impedances measured for the PEDOT-PSS film after incubation in PBS for 30 min in step 3; i_p is the peak current for the electropolymerization, by cyclic voltammetry, of the virus-PEDOT composite in step 4. The VBR device yield using the process windows described below was ≈60%.

Step 1: The DC resistance between two end-points on the individual gold pad should be 3.9 to 5 Ω. This resistance adds to the resistance of spin-coated PEDOT-PSS resistance to yield the final DC resistance across PEDOT-PSS coated electrodes.

Step 2: Chips with DC resistance across the baked PEDOT-PSS films of 240 to 380 Ω are then used for further fabrication.

Step 3: To eliminate the baseline drift, the PEDOT-PSS films from the previous step are immersed in PBS for 30 minutes. This step results in increased resistance of the swollen PEDOT-PSS film, tracked by the Nyquist Zre = 300 – 500 Ω and Zim = 80 – 150 Ω values.

Step 4: The cyclic voltammogram is indicative of EDOT polymerization quality and phage entrapment. The shape of the voltammogram along with the anodic peak current (i_p) values are important screening parameters. The i_p separation between two subsequent scans is approximately 1×10^{-4} A.

Step 5: Visual inspection of the newly formed biorecognition layer for any abrasions, prevents unusual Nyquist drift and non-specific signals.

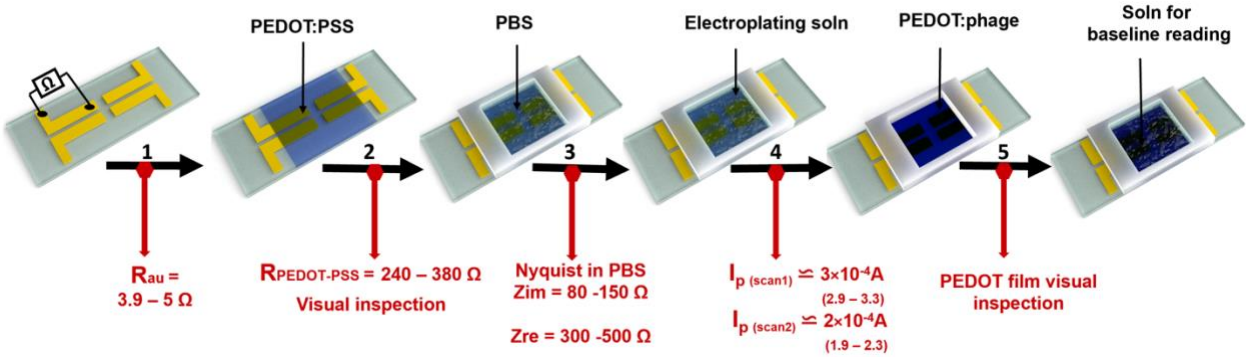

Figure A.1 - Process flow for the VBR fabrication process, including the process window parameters that were enforced for this process, indicated in red.

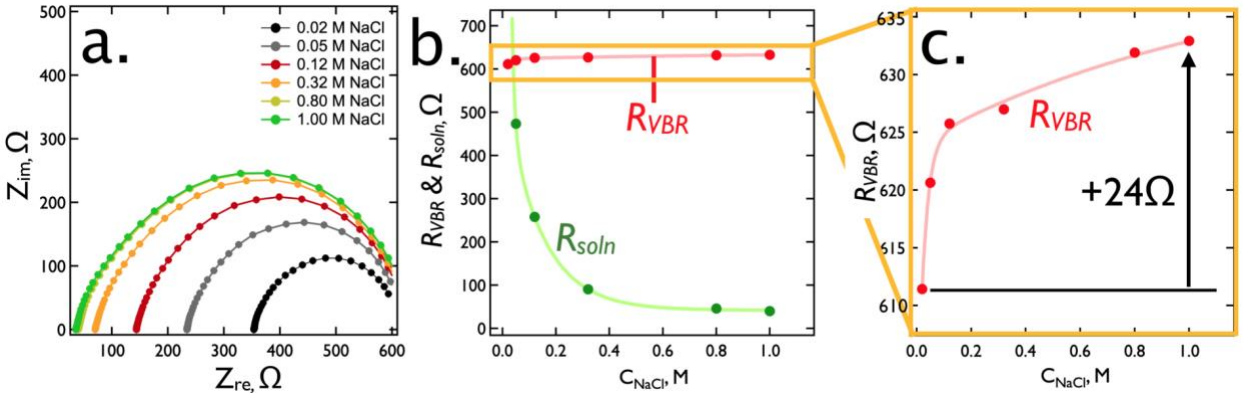

Figure A.2 - Influence of C_{NaCl} on VBR response in the absence of protein. a). Nyquist plots for a single VBR in six aqueous NaCl solutions ranging in concentration from 0.02 M to 1.0 M, as indicated. b). Plot of R_{VBR} and R_{soln} as a function of C_{NaCl}. R_{soln} (green trace) decreases in proportion to $1/C_{NaCl}$ qualitatively as expected, but R_{VBR} is weakly affected, increasing by just 24 Ω against a background of ≈ 600 Ω (b,c).

Table A.1 - VBR circuit elemental values corresponding to the Nyquist plots of Figure 2.8a-c.

Fig 2.8a	Synthetic Urine			10 pM DJ-1	
	value	st dev		value	st dev
R_{sol} (Ω)	338.5	0.2		333.6	0.7
R1 (Ω)	1097	4		1136	8
C_{VBR} (F)	1.040×10^{-5}	4×10^{-8}		1.010×10^{-5}	5×10^{-8}
R_{VBR} (Ω)	1617	2		1674	2
CPE, Q (F)	2.570×10^{-5}	5×10^{-8}		2.54×10^{-5}	2×10^{-7}
CPE, n	0.85	0.00		0.85	0.00
Fig 2.8b	Synthetic Urine			1 nM DJ-1	
	value	st dev		value	st dev
R_{sol} (Ω)	331.7	0.4		333.6	0.1
R1 (Ω)	1490	2		1823	6
C_{VBR} (F)	8.70×10^{-6}	2×10^{-8}		8.610×10^{-6}	8×10^{-9}
R_{VBR} (Ω)	1663.3	0.4		2010	10
CPE, Q (F)	2.380×10^{-5}	9×10^{-8}		2.53×10^{-5}	3×10^{-7}
CPE, n	0.86	0.00		0.86	0.00
Fig 2.8c	Synthetic Urine			300 nM DJ-1	

	value	st dev		value	st dev
R_{sol} (Ω)	304.5	0.1		275	1
R1 (Ω)	2550	20		4110	50
C_{VBR} (F)	8.49×10^{-6}	5×10^{-8}		6.99×10^{-6}	9×10^{-8}
R_{VBR} (Ω)	1983	5		2634	3
CPE, Q (F)	2.66×10^{-5}	1×10^{-7}		2.78×10^{-5}	2×10^{-7}
CPE, n	0.86	0.00		0.86	0.00

Appendix B: Supplementary Information for Chapter 3

B.1. Two Virus Receptors Used in this Study.

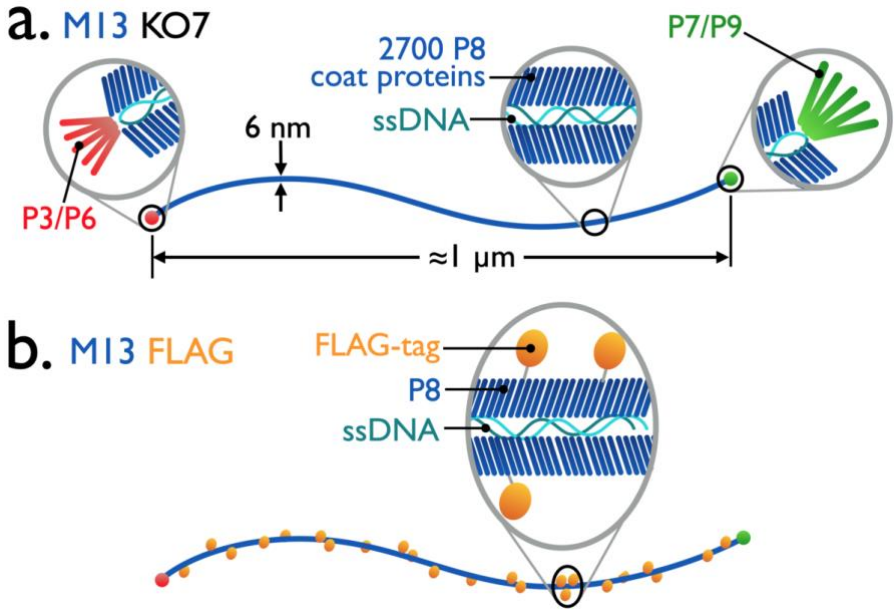

Figure B.1 - Schematic diagrams of the two M13 virus receptors, used for the detection of the two antibodies investigated here. a). M13 KO7 is an M13 variant with no appended peptide epitopes. The anti-M13 Ab recognizes 2700 P8 coat proteins, b). M13 FLAG is an M13 variant that has FLAG-tag (with sequence DYKDDDDK, where D = aspartic acid, Y = tyrosine, K = lysine) appended as C-terminal fusions to a subset of the P8 coat proteins.

B.2. Demonstration of VBR Insensitivity to Two Antibodies.

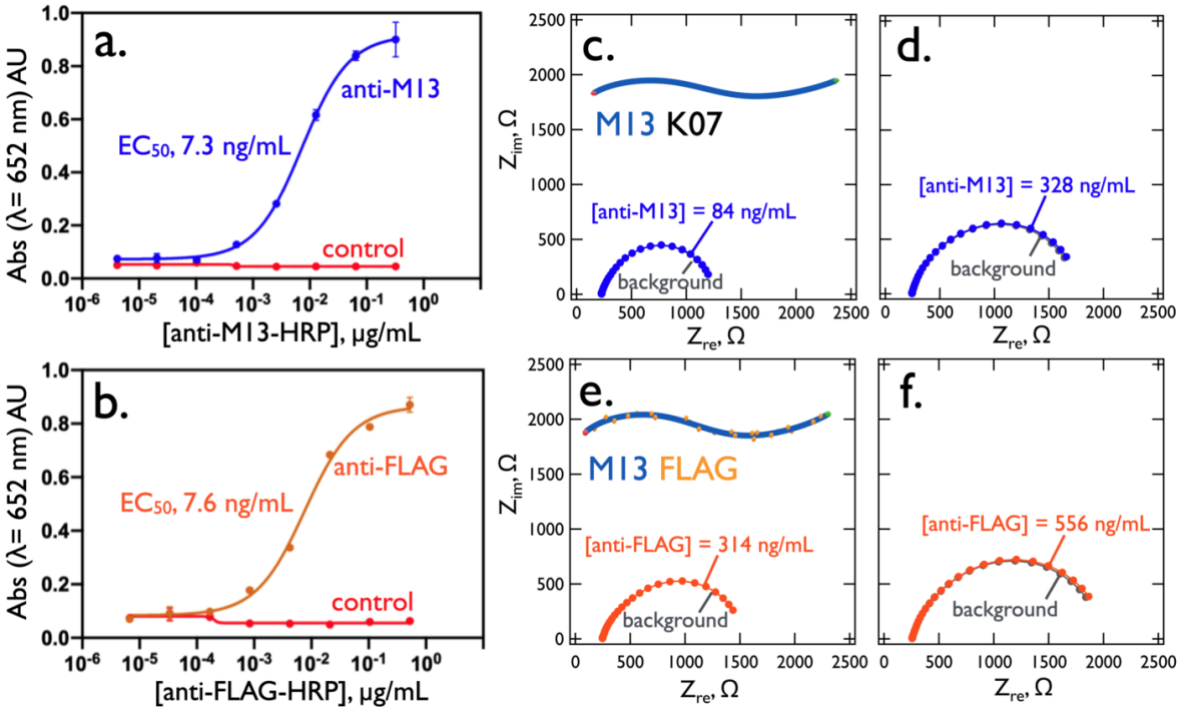

Figure B.2 - Demonstration of VBR insensitivity to two antibodies. a,b). Enzyme-linked immunosorbent assay (ELISA) data for the binding of (a) anti-M13-HRP (horse radish peroxidase) to M13 KO7 showing strong binding with a EC_{50} = 7.3 ng/mL, and the same experiment for anti-FLAG-HRP detection of M13 FLAG showing an EC_{50} = 7.6 ng/mL. The anti-M13 control tracks the response of VBRs containing no phage; the anti-FLAG control shows the response of VBRs containing Stop-4 phage. d). Nyquist plots for two VBRs showing data for a PBS buffer (c) and anti-M13 (d) in PBS at two concentrations. Nyquist traces for buffer and anti-M13 overlap indicating no measurable signal is present. e,f). Same experiment for two VBRs attempting the detection of anti-FLAG at two concentrations, as indicated. Again, buffer and anti-FLAG Nyquist plots overlap, indicating no measurable signal is present.

B.3. Additional Experimental Details.

B.3.1. Fabrication of an O^2VBR.

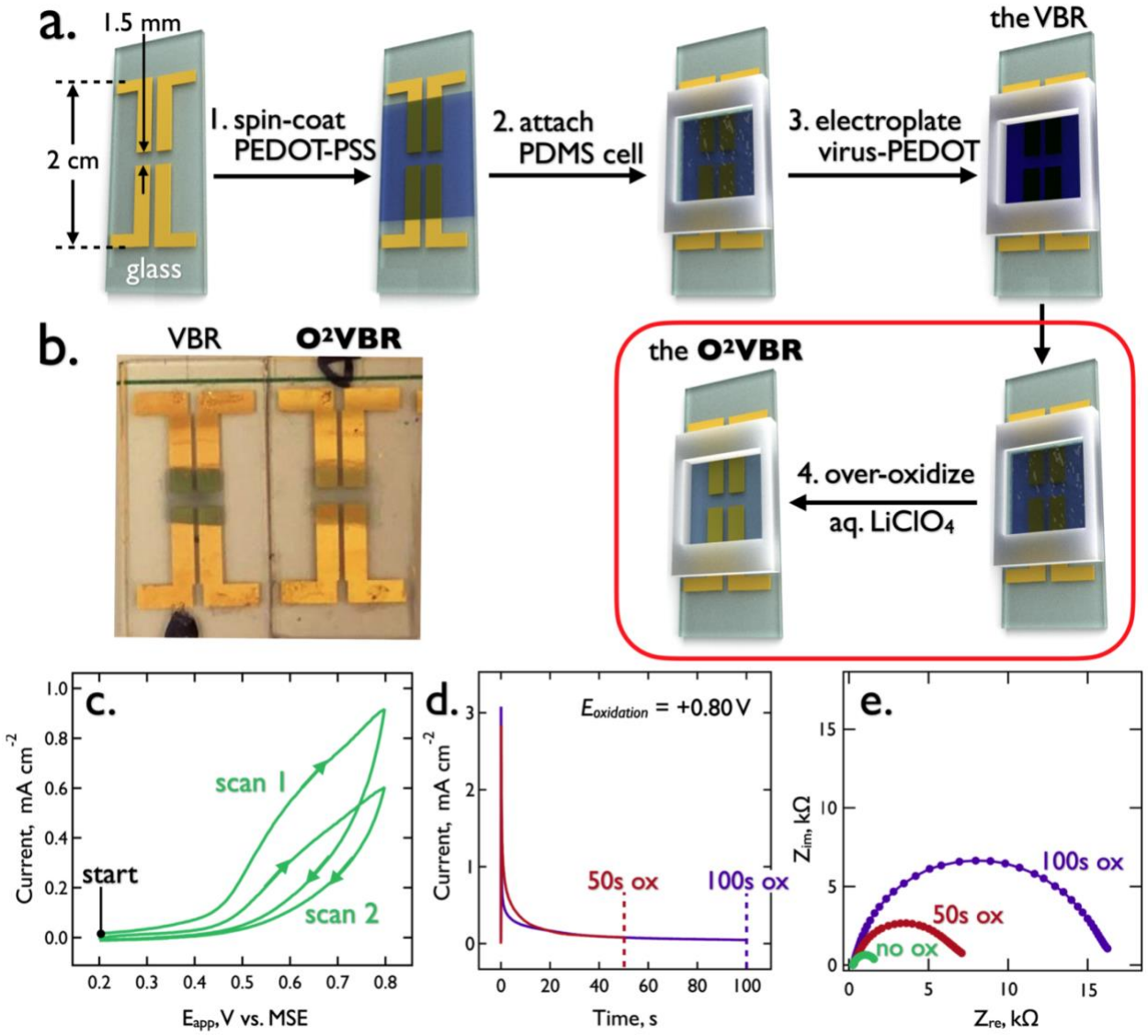

Figure B.3 - Fabrication of an O^2VBR. a). Process flow for the five-step fabrication process, b). Optical photographs of a VBR (left) and an O^2VBR (right). The bleaching of the bioaffinity layer relative to the VBR is characteristic of the over-oxidation process, c). Electrodeposition of the virus-PEDOT layer at 20 mV/s in a solution containing 2.5 mM EDOT, 12.5 mM $LiClO_4$, and 8 nM phage. d). Current versus time for the potentiostatic oxidation of the VBR channel at +0.80 V vs. MSE for 50 s and 100 s, as shown. e). Nyquist plots for the impedance analysis of a VBR (no oxidation, green), an O^2VBR with 50 s of oxidation (red) and an O^2VBR with 100 s of oxidation, (purple).

B.3.2. FLAG-displaying C2 phage propagation and purification

The phagemid DNA was transformed into SS320 competent E. coli, and transformants were plated on a carbenicillin-supplemented (50 µg/mL) agar plate before incubation at 37 °C overnight. A single colony was selected to inoculate 25 mL of 2YT

supplemented with carbenecillin (50 µg/mL) and tetracycline (2.5 µg/mL). The culture was shaken at 37 °C until OD600 reached 0.5; then, 30 µM IPTG and sufficient M13KO7 to achieve a multiplicity of infection of 4.6 was added. After an additional 45 min incubation, 8 mL of the culture was used to inoculate a 150 mL of 2YT supplemented with carbenecillin (50 µg/mL), kanamycin (20 µg/mL), and IPTG (30 µM). This culture was incubated at 30 °C with shaking at 225 rpm for 18 h. The cultures were centrifuged at 10 krpm (15300 x g) for 10 min.

The supernatant was decanted into a centrifuge tube containing 1/5 the volume of PEG-8000 (20%, w/v) and NaCl (2.5 M). The tube was inverted 5 times and stored on ice for 30 min followed by an additional centrifugation at 10 krpm (15300 x g) for 15 min. The supernatant was decanted, and tubes were centrifuged for an additional 4 min at 4 krpm (2429 x g). The pellets were resuspended in PBS and the precipitation steps were repeated. Phage concentrations were quantified by measuring absorbance at 268 nm. Finally, the phage were diluted to 60 nM, flash frozen with Glycerol (10%, v/v), and stored at -80 °C. To prepare for devices or ELISAs, the phage solution was thawed on ice, precipitated a second time, and diluted to 40 nM in either $LiClO_4$ (12.5 mM) or PBS, respectively.

B.3.3. M13K07 phage Propagation and Purification

XL-1 Blue competent cells were streaked on a tetracycline-supplemented (1.5 µg/mL) agar plate before incubation at 37 °C overnight. 10 colonies were selected to inoculate 5 mL of 2YT supplemented with tetracycline (2.5 µg/mL). The culture was shaken at 37 °C until OD600 reached 0.5-0.6. This OD600 of was aliquoted to 200 uL in seven different microcentrifuge tubes. Ten serial dilutions of M13 KO7 helper phage were created by first combining 1.5 µg of phage stock solution with 13.5 µL of PBS to create the first solution. 1.5 µL of the first dilution was added to 13.5 µL of PBS and repeated until ten serial dilutions were prepared. 10 µL of the fourth through tenth M13 KO7 phage dilutions are added separately to the above 200 uL culture aliquots. Each phage-culture aliquot was then separately combined with 4 mL of top agar, inverted 5 times, then poured onto tetracycline-supplemented (1.5 µg/mL) agar plates to uniformly cover the surface.

The plates were incubated at 37 °C overnight. A plate was chosen where individual phage plaques were visible. Using a flame-sterilized Pasteur pipette, a single plaque was removed from the plate and added to 5 mL of 2YT supplemented with tetracycline (2.5 μg/mL) and shaken at 37 °C overnight. This culture was added to 150 mL of 2YT supplemented with kanamycin (20 μg/mL) and shaken at 37 °C for 18 h. The supernatant was decanted into a centrifuge tube containing 1/5 the volume of PEG-8000 (20%, w/v) and NaCl (2.5 M). The tube was inverted 5 times and stored on ice for 30 min followed by an additional centrifugation at 10 krpm (15300 x g) for 15 min. The supernatant was decanted, and tubes were centrifuged for an additional 4 min at 4 krpm (2429 x g). The pellets were resuspended in PBS and the precipitation steps were repeated. Phage concentrations were quantified by measuring absorbance at 268 nm. Finally, the phage were diluted to 8 nM, flash frozen with Glycerol (10%, v/v), and stored at -80 °C. To prepare for devices or ELISAs, the phage solution was thawed on ice, precipitated a third time, and diluted to 40 nM in either $LiClO_4$(12.5 mM) or PBS, respectively.

B.3.4. Impedance Spectroscopy

All IS measurements were performed on a Princeton Applied Research PARSTAT Model 2263 potentiostat via Electrochemistry PowerSuite 2.6 software or a PalmSense 3 potentiostat via PSTrace 5.6 software. EIS Analyzer software (ABC Chemistry) was used to fit the data to the circuit as described previously. [44] 300 iterations of the Powell algorithm was used to extract values for each element in the same equivalent circuit as previously reported.[2] The difference in the R_{VBR} value acquired before and after exposure to antibodies is used to determine the signal of the device. If a tail not conforming to a semicircle appeared at the low frequency end of the impedance Nyquist plot, the lowest frequencies from 1 Hz to ~5 Hz were omitted from the equivalent circuit fitting process.

B.3.5. Control Experiments

Three control experiments were performed for O^2VBRs. For example, for O^2VBRs loaded with KO7 phage that targets anti-M13, one control was a device fabricated without phage; exposure of this device to the anti-M13 antibody assesses non-specific binding of the antibody to PEDOT. A second control was a O^2VBR with KO7 “helper” phage, which lack a displayed receptor, exposed to anti-FLAG, an IgG antibody; this control can detect any non-specific signal from similar antibodies to the KO7 phage. A third control involved

the exposure of O^2VBRs loaded with KO7 phage to anti-GFP (green fluorescent protein), another IgG antibody, to further confirm the specificity of these biosensors for their intended target, the anti-M13 antibody.

For FLAG-displaying phage, the first control was a device without phage exposed to anti-FLAG to examine non-specific binding of the antibody to PEDOT. Second, O^2VBRs loaded with STOP-4, a phage that does not display peptide receptor moieties, were exposed to anti-FLAG to determine the level of non-specificity between phage and the antibody. The last two controls were O^2VBRs loaded with FLAG-displaying phage exposed to anti-DL1 (IgG antibody) and anti-GFP, both to investigate non-specificity between similar antibodies and the device.

B.3.6. Raman Spectroscopy

Samples for Raman spectroscopy experiments were prepared in a similar fashion to the samples for XPS. Raman spectra were collected using a customized Renishaw InVia Raman microscope with a 785 nm excitation laser and a 2 μm spot size. Peak positions were taken from the apparent peak maximum; no peak fitting was used to deconvolute the spectra. Figure B.1 shows Raman spectra from a normal VBR and an O2VBR, both sampled from the center of the film. Bands in the Raman spectra correspond well with literature Raman spectra of PEDOT films.[177–180] A 3 cm^{-1} shift in the band corresponding to symmetric Cα=Cβ stretching from 1425 cm^{-1} in the normal VBR to 1428 cm^{-1} for the O^2VBR is consist with literature on oxidized PEDOT films.[180–185]

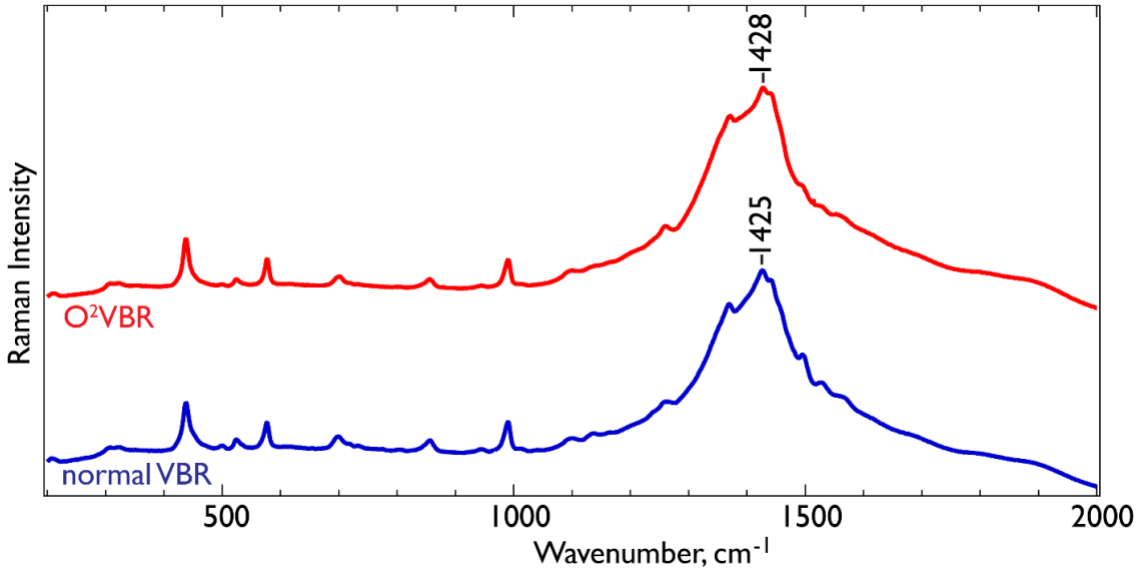

Figure B.4 - Raman spectra of normal and O²VBR films. Indexed band corresponds to symmetric Cα=Cβ stretching.

B.3.7. X-Ray Photoelectron Spectroscopy

Samples were fabricated for X-ray photoelectron spectroscopy (XPS) experiments as described in the main text. After the final fabrication step, sensors were then rinsed thrice with Milli-Q water (resistivity of 18.2 MΩ*cm, Millipore Milli-Q Gradient) before being dried overnight in a vacuum desiccator. XPS data was acquired using the AXIS Supra by Kratos Analytical Inc equipped with monochromatic Al/Ag X-ray source. The adventitious C 1s peak corresponding to the C-C bond was referenced to 284.8 eV. Any depth-profiling was performed at the center of the sample using 10 kV of 1000+ Ar clusters for 6 cycles of 5 seconds each.

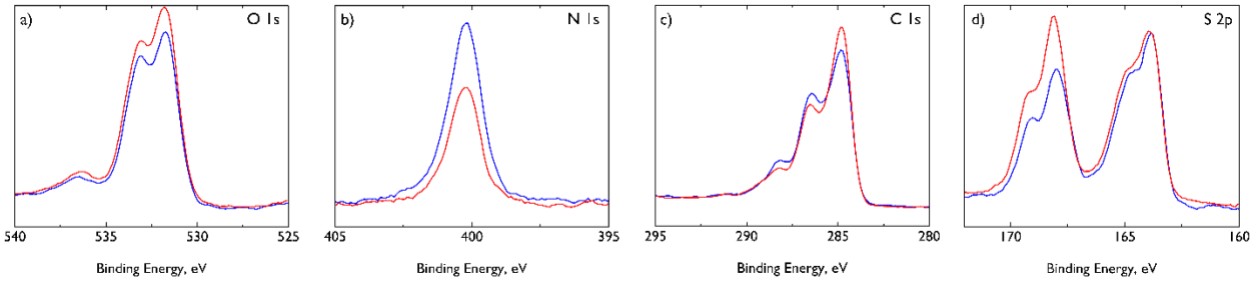

Figure B.5 - XPS spectra of a) O 1s, b) N 1s, c) C 1s, and d) S 2p. Blue traces represent the normal VBR, red traces represent the O²VBR. No significant shifts in binding energies were observed between the normal VBR and O²VBR. Deconvoluted peaks (not shown here) appear at similar binding energies to those observed in previous literature.[186–189]

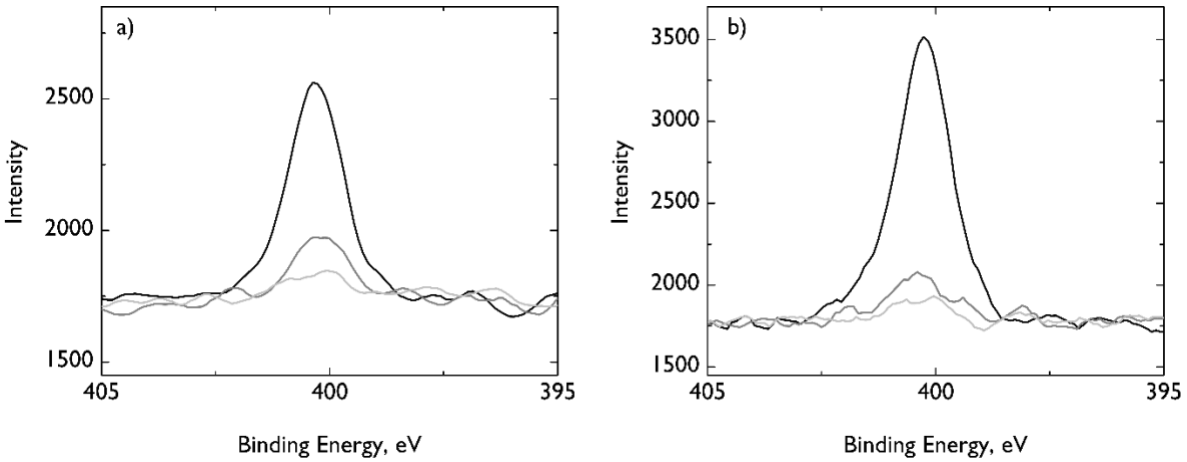

Figure B.6 - N 1s XPS depth profiling of a) normal VBR and b) O^2VBR. Significant nitrogen signal was observed at the surface of both the normal VBR and O^2VBR, attributed to the nitrogen atoms on the P8 coat protein of bacteriophage. As the surface of the sensor was etched, the nitrogen signal was reduced significantly in both the normal and O^2VBR. Black trace represents 0 seconds of etching, grey trace represents 5 seconds of etching, and light grey represents 10 seconds of etching.

Appendix C: Supplementary Information for Chapter 4

C.1. Table of Nanoscopic pH Sensors

Table C.1 - Recent examples of nanoscale pH sensors in the literature.

Type of Sensor	Size[i]	Transduction Method	pH Range	Response Time	Repeatability[i]	Ref
Self-Assembled Au Nanoclusters into microflowers	AuNC 2 nm Diameter Microflowers = 10 – 30 µm diameter	Phosphorescence	6.5 – 10.5	5 s	5 cycles	190
Chemically Modified Fluorescent Nanodiamonds	50-100 nm diameter	Fluorescence	3.0 – 11.0	<1 s	5 cycles	191
Nitrogen doped Graphene Quantum Dot Copolymer film	QDs: 3 nm diameter film: 100 µm thick	Fluorescence	2.0 – 13.0		35 cycles over 30 days	192
PANI@Au nanoparticles	100 nm diameter	Photoacoustic imaging	1.0 – 8.0			193
Organosilica nanoparticles	100 – 500 nm Diameter	Fluorescence	4.5 - 8			194
Carbonized polymer dots	3 nm Diameter	Photoluminescence	3.0 – 8.0		5 cycles	195
Gold-Photodeposited Silver Nanowire	<300 nm diameter	SERS	4.4 – 9.3			196
Quantum Dot Integrated Graphene Oxide	30 – 85 nm Diameter	Photoluminescence	1.0 – 7.0	5 min	3 cycles	197
AuNPs with 4MBA SAM	60 nm Diameter	SERS	2.0 – 10.0			198
Silica nanoparticle functionalized with dyes	95 nm Diameter	Fluorescence	3.0 – 9.0			199
Dual-Luminescent polymer nanoparticles	40-48 nm Diameter	Fluorescence	4.5 – 8.0			200

Syringaldazine modified pyrolyzed carbon nanopipette	50 nm Diameter	Voltametric	2.0 – 12.0	1 s		[201]
Carbon nanopipette electrode	800 nm Diameter	Potentiometric	6.0 – 8.5	<5 s	3 cycles	[134]
Si nanoplate – nanowire transistor	100 nm nanowire Diameter	Double-gated FET	4.6 – 10.7	5 min		[202]
Si Nanowire Array	30 nm - Diameter	FET	4.0 – 8.0			[203]
PANI electrodeposited thin film		Potentiometric	3.0 – 8.0		6 cycles	[204]
PANI nanofiber array		Potentiometric	3.9 – 10.1	15 s	2 cycles, 97.9% retention	[205]
MoS_2 monolayer	100 - 3000 μm^2	Field-Effect Transistor	2.0 – 12.0		100 cycles	[206]
PANI nanowire array	500 x 500 µm	Voltametric	1 – 6		5 cycles	[146]
Single PANI-filled nanogap	<100 nm Length, Height, and Width	Impedimetric	2.0 – 9.0	30 s	17 cycles between pH 1.0 and 2.0 – 9.0	This work

i. Size describes the largest dimension of the active material performing pH sensing.
ii. Repeatability represents the number of measurement cycles demonstrated for solutions of two or more pH values.

C.2. Concept and Fabrication of PANI Nanojunction pH Sensors

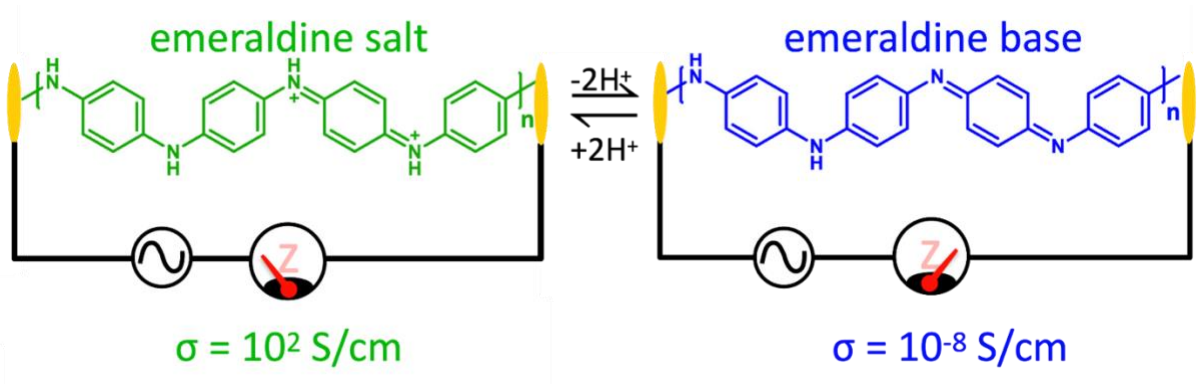

Scheme C.1 – Schematic representation depicting the structure of poly(aniline) (PANI) and its

conductivity in the protonated (emeraldine salt) and deprotonated (emeraldine base) state.

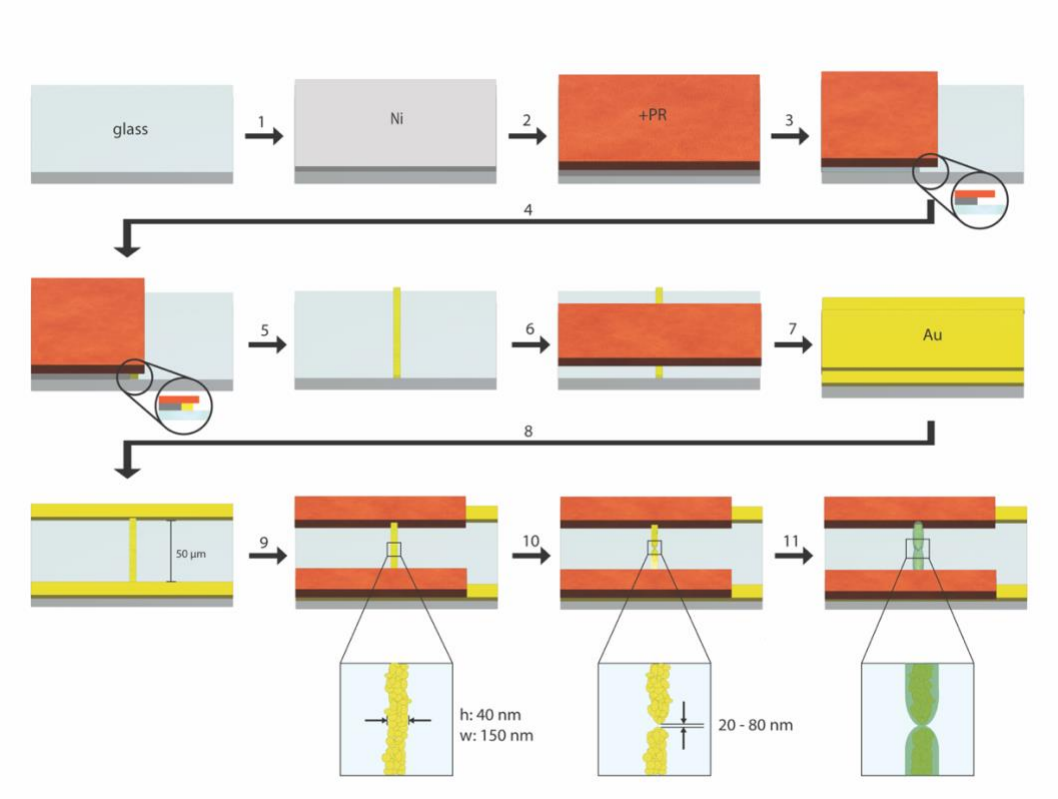

Figure C.1 - Fabrication process for single poly(aniline) (PANI) nanojunction sensors. (1). Ni Physical Vapor Deposition (PVD), 40 nm. (2). Spin-coating positive photoresist (+PR). (3). UV exposure, developing and etching of half of the Ni slide, leaving overhanging +PR. (4). electrodeposition of Au NW on Ni edge. (5). Removal of +PR and etching of remaining Ni. (6). Spin-coating +PR, UV exposure of a negative of the contact pattern, and developing. (7). PVD of 4 nm Cr, 60 nm Au. (8). Sonication in acetone. (9). Spin-coating, UV exposure, and developing of a ~45 µm gap within the contacts to insulate contacts from solution. (10). Electromigration to form nanogap. (11). Electropolymerization of PANI.

C.2.1. Single Au Nanowire Fabrication

The electrodeposition of single gold nanowires was accomplished using the lithographically patterned nanowire electrodeposition process or LPNE, as previously described and shown in Figure C.1 steps 1 - 5.[151] Step 1 was the physical vapor deposition (PVD) of Ni (40 nm) onto a glass slide. Step 2 shows the spin-coating and soft baking of positive photoresist onto the Ni thin film. Next, Step 3 shows the UV exposure (λ_{UV} = 365 nm), developing, and etching of Ni from half of the slide. A trench was etched into the Ni, so the photoresist creates an overhang to limit the height of the nanowire during the electrodeposition. Step 4 shows electrodeposition of a single Au nanowire on a Ni edge

with overhanging photoresist (-0.9 V vs. Saturated Calomel Electrode for 900 s). Once the single Au NW was prepared by LPNE a glass slide, a lift-off process was performed to deposit Au contacts 50 µm apart, providing robust contacts to the Au nanowire. This process was the following: First positive photoresist (Microposit S1808) was spin-coated on the bare gold wire and glass surface in step 6, and a negative of the contact pattern was used as a mask during exposure to UV light. The exposed photoresist was the developed, and in step 7, 4 nm of Cr followed by 60 nm of Au were deposited on the glass slide by physical vapor deposition. Lift-off was accomplished in step 8 by sonicating the slide in acetone for 1 minute, resulting in the removal of the remaining photoresist and the Au deposited on top of it. This left two Au contact pads, separated by 50 µm of a single Au nanowire. These contacts were covered with an insulating photoresist layer in step 9 to prevent their exposure to test solutions.

C.2.2. Electromigration

The automated, feedback-controlled electromigration process used to prepare nanogaps in single gold nanowires has been described elsewhere and is shown step 10 (Figure C.1).[152] Briefly, a feedback-controlled voltage ramping program was applied across the Au nanowire. The initial nanowire resistance, R_{ref}, was measured and recorded. From an initial applied voltage, E_{app} = 10 mV, E_{app} was increased at 5 mV per second. When the resistance of the wire changed by 0.015R_{ref}, E_{app} was reduced by 50 mV, a new R_{ref} was recorded, and the process was repeated until a large increase in resistance to >1 MΩ signaled the formation of a single nanogap (Figure 4.2a). Breaks seen in the measurements of E_{app} and resistance (Figure 4.2a) mark time points at which a 50 mV reduction in E_{app} occurred. This algorithm reproducibly generated nanogaps with dimensions 50 ± 30 nm range, as required for the fabrication of the nanometer-scale pH sensors described here.

C.3. Control Experiments

C.3.1. Single Au Nanowire pH Controls

In order to confirm that all pH generated signal is coming only from the PANI rather than the gold, a single Au nanowire was exposed to solutions with pH = 1.0 – 9.0. The Nyquist plots for these data can be seen in C2a. .Extracting the Z_{im} at low frequency (Figure C.2b) demonstrates that there is large change or clear trend with pH.

Furthermore, fitting these data to the equivalent circuit in figure C.2a-b, shows that neither resistor changes significantly with pH.

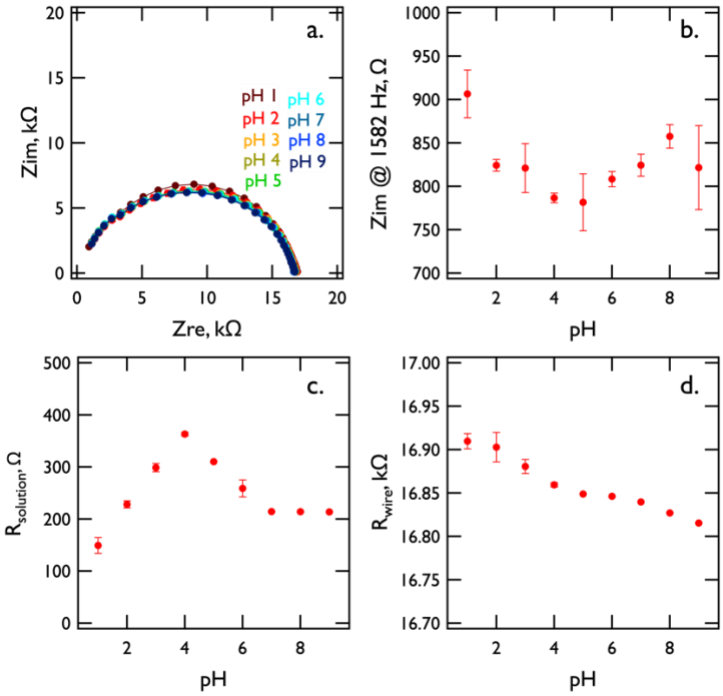

Figure C.2 - pH control experiments for a continuous Au nanowire. a). Nyquist plots in different PBS solutions of pH 1.0 – 9.0. b). The Z_{im} impedance at the lowest frequency recorded. c). The R_{soln} values and (d) R_{wire} extracted from fitting the impedance data to the (R_{soln} + Q_{EDL}) / R_{wire} equivalent circuit. Error bars represent one standard deviation of triplicate measurements.

C.3.2. Empty Nanogap pH Controls

Again, to rule out pH related signal coming from the Au nanogap, solutions of various pH values were exposed to an empty Au nanogap. The Nyquist and Z_{im} bode plot for these data are shown in figures C.5a and C.5d. Extracting the low frequency Z_{im} again shows no clear trend, as can be seen in figure C.5e. Fitting these data to the high salt nanogap equivalent circuit again demonstrates no clear trend in figure C.5b-c.

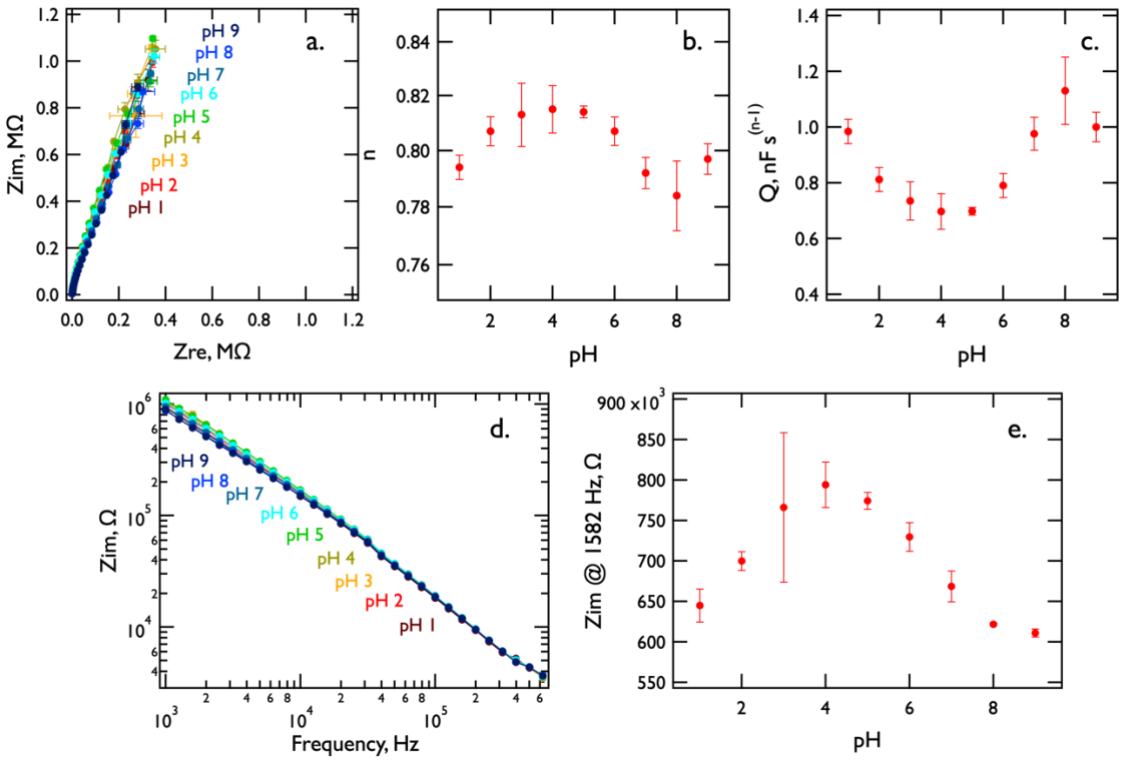

Figure C.3 - pH controls for empty nano-gap within a single Au nanowire. a). Nyquist plots in different PBS solutions of pH = 1.0 – 9.0. b-c). Best fit values from the equivalent circuit for the constant phase element, n (b) and Q (c). d). Bode impedance plot of Zim vs. Frequency for the same sensor. e). Plot of low frequency Z_{im} vs. pH.

C.4. Validation of Nanowire, Empty Nanogap, and PANI Filled Nanogap Equivalent Circuits

C.4.1. Single Au Nanowire Equivalent Circuit

The equivalent circuit for the single Au is presented in the main text figure 4.3d. This circuit contains the through wire resistor in parallel with the solution resistor and double layer capacitor series. To confirm that this circuit is valid for the sensor, solutions of $LiClO_4$ of different concentrations were added to the sensor to evaluate the solution impedance spectra, which is seen as Nyquist plots in C.4a. Figure C.4c shows that R_{soln} changed in accordance with the $LiClO_4$ concentration and thus the ionic strength. As evidence by figure C.4b, R_{wire} is not affected by the change in the ionic strength of the solution and instead continuously matches with what is measured using a multimeter's DC resistance feature.

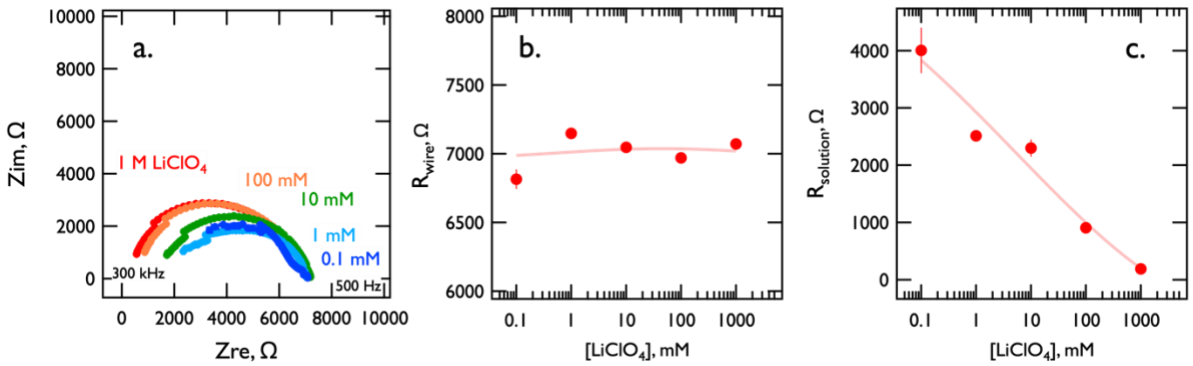

Figure C.4 - Experimental data and best fit models for the Au nanowire while varying the concentration of $LiClO_4$ exposed to the device. a). Nyquist plots for the single Au NW exposed to different $LiClO_4$ concentrations. The Nyquist plots are taken from 300 kHz – 500 Hz. b-c). The best fit values of the (b) R_{wire} component and (c) R_{soln} of the equivalent circuit as a function of $LiClO_4$ concentration. Error bars are calculated using the standard deviation of the best fit values from three Nyquist plots of each $LiClO_4$ concentration.

C.4.2. Empty Nanogap Inside Single Au Nanowire Equivalent Circuit

To evaluate the proposed equivalent circuit for the empty nano-gap seen in Figure 4.3e, a solutions resistor in series with a double layer capacitor, solutions of $LiClO_4$ of different concentrations were exposed to the empty nano-gap. The Nyquist plots in Figure C.4a show a high frequency semicircle forming when the salt concentration is low, suggesting a parallel R and C, but no high frequency semicircle when the salt concentration is high. Thus, two different equivalent circuits must be used depending on the salt concentration. Figure C.5b shows the low salt concentration circuit as a solution resistor in series with a parallel R_{ionic} and C_{bulk}, representing the impeded ionic charge transport at low ionic strength solutions, in series with a double layer constant phase element.[207] The high salt concentration circuit includes just the R_{soln} and the $Q_{dl\text{-}wire}$ in series. The R_{soln} values track well with the salt concentration, as does the R_{ionic} with only the low salt concentrations. Other noteworthy trends are that the imaginary impedance at low frequency decreases with increased salt concentration, signifying an increase in capacitance.

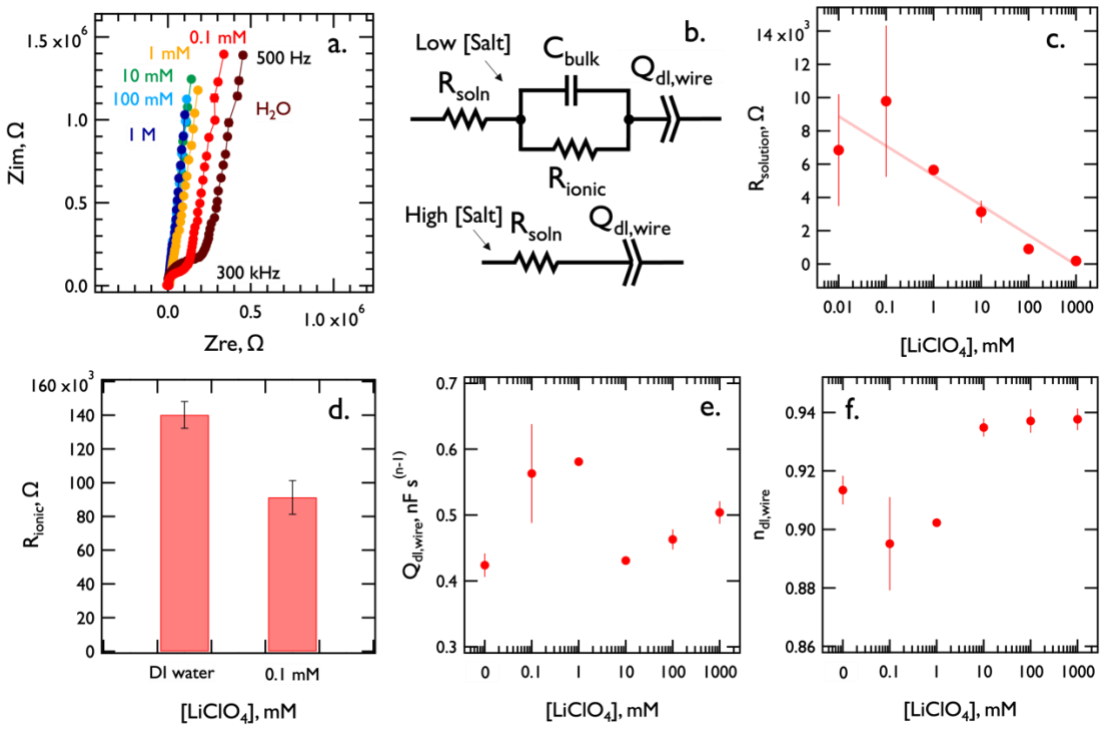

Figure C.5 - Experimental data and best fit models for the Au nanogap while varying the concentration of $LiClO_4$ exposed to the device. a). Nyquist plot of the Au nanogap device exposed to different concentrations of $LiClO_4$. c). Best fit values of the R_{soln} of the equivalent circuit as a function of $LiClO_4$. d). Best fit values of the R_{ionic} component of the equivalent circuit for the solutions with a low $LiClO_4$ concentration. e-f). Best fit values of (e) Q and (f) n.

C.4.3. PANI Nanojunction Equivalent Circuit

The equivalent circuit proposed for the filled nanogap is the same is the continuous Au nanowire, seen in Figure 3f. Again, this circuit has a PANI resistor in parallel with a solution resistor and double layer capacitor in series. Figures S6 a-f show the Nyquist plots in increasing pH solutions overlayed with the best fit circuit. The high frequency impedance data shows a small non-ideal deviation, which is minimized by using a CPE instead of a capacitor. Past pH 4, the Nyquist plot does not show semicircular behavior anymore, and to extract best fit values, the PANI resistor must be set to a large value. All the best fit values can be seen in Table C.2.

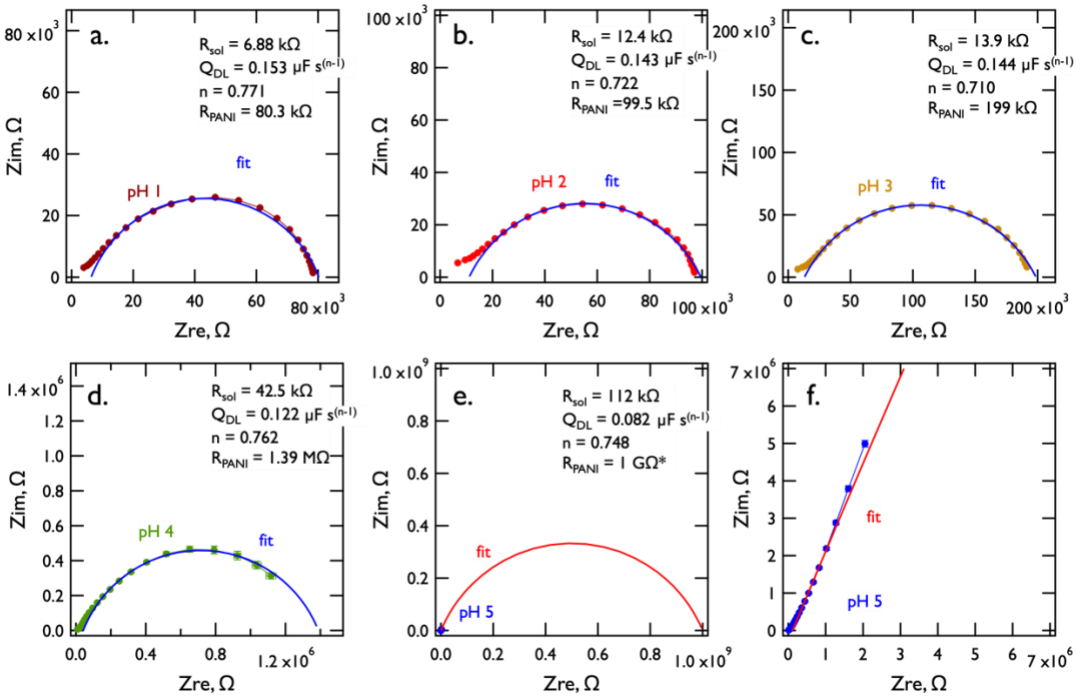

Figure C.6 - Averaged impedance data of the PANI NJ sensor exposed to various solutions of different pH values overlayed with the best fit overlayed. pH = 1.0 – 5.0 are shown in (a-e), respectively, and (f) shows the pH 5.0 data enlarged to what was seen in the experiment. The R_{PANI} component of the best fit model in (e-f) was constrained to 1 GΩ due to the lack of low frequency impedance data that could capture this high impedance behavior.

Table C.2 - Best fit values from the randomized pH exposures in figure S6. The Levenberg-marquardt algorithm was used with 500 iterations to fit the averaged data to the equivalent circuit: $(R_{soln} + Q_{EDL})/R_{PANI}$.

pH	R_{soln}, kΩ	Q_{DL}, μF s^{n-1}	n_{DL}	R_{PANI}, kΩ
1	6.88	0.153	0.771	80.3
2	12.4	0.142	0.722	99.5
3	13.9	0.144	0.710	199
4	42.5	0.112	0.762	1,390
5	112	0.082	0.748	10^{6*}
6	230	0.061	0.691	10^{6*}
7	210	0.046	0.704	10^{6*}
8	470	0.04	0.787	10^{6*}
9	485	0.039	0.788	10^{6*}

* value constrained due to lack of low frequency impedance data

C.5. Interfering Ions Study

C.5.1. Influence of Ionic Strength on *NJ-pH* Accuracy

Figure C.7 shows the flow chart for the correction of the pH for different salt concentrations. The first step was to measure the salt concentration in the solution using 300 kHz Z_{tot}. This information is used to decide which Z_{im} at 0.8 Hz vs pH calibration curve to use, providing a more accurate measurement of the pH.

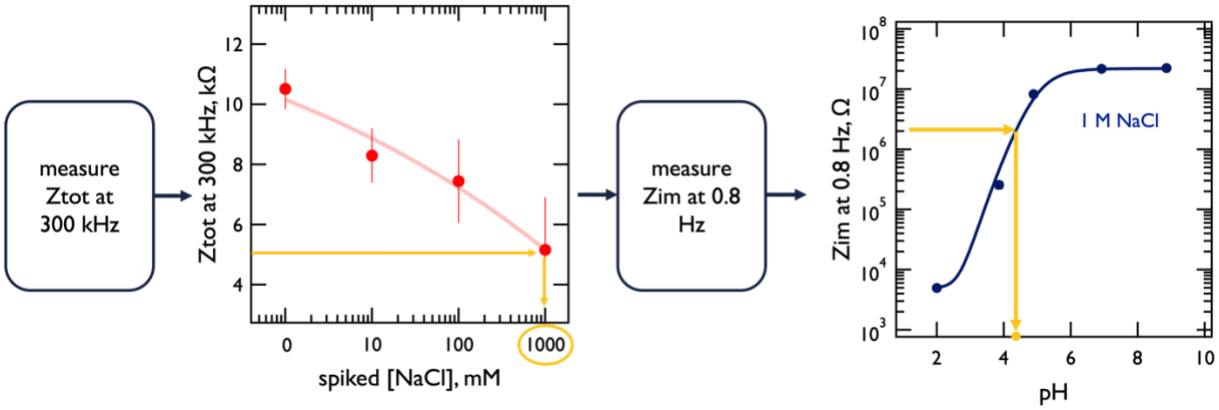

Figure C.7 - A diagram of how one would use the high frequency impedance to correct for the salt effect. First, measuring Z_{tot} at 300 kHz will allow the sensor to predict the salt concentration. Seen in this diagram is a theoretical measurement of Z_{tot} = 5 kΩ, which translates to the 1 M NaCl calibration curve. Next, Z_{im} at 0.8 Hz is measured, and plotted on the calibration curve of Z_{im} vs pH. In this diagram a theoretical measurement of Z_{im} = 2 MΩ is made, leading to a measured pH of 4.2.

C.5.2. Accuracy of *NJ-pH* in Synthetic Urine

Figure C.8 shows the results from two *NJ-pH* sensors in which 100 mM NaCl phosphate buffers were used to create calibration curves. A solution of synthetic urine was used to test the accuracy of the sensor to more complex media. The synthetic urine contains Urea, $MgSO_4$, $CaCl_2$ and NaCl in DI water. The measured pH from the *NJ-pH* sensors was 6.72 ± 0.04 compared to the measured pH from a glass pH-electrode which was 6.62.

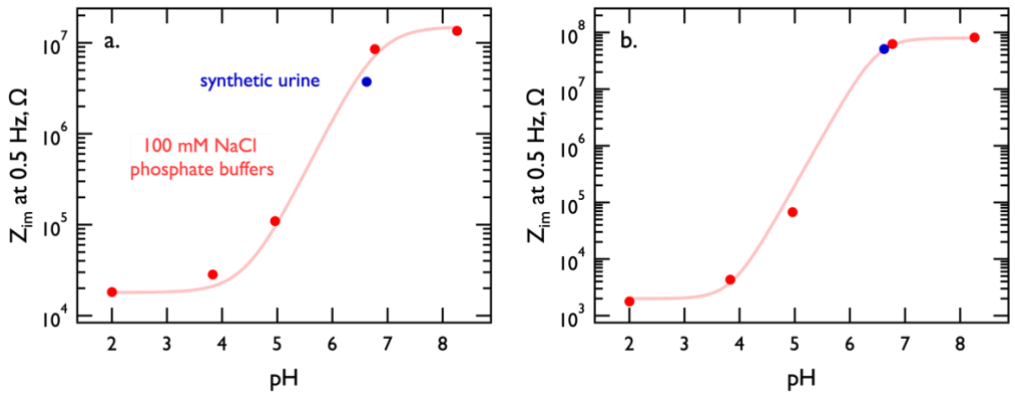

Figure C.8 - Calibration curves for two separate NJ-pH sensors. a-b). Low frequency Z_{im} vs pH plots. The data in red was collected using 50 mM phosphate buffers with 100 mM NaCl. The blue data points on each plot are measurements taken of synthetic urine, which was found to have pH = 6.62 according to a glass pH-electrode. The calculated pH for the synthetic urine samples was 6.69 and 6.76 for (a) and (b), respectively.